

## Photocopy and Use Authorization

In presenting this thesis in partial fulfillment of the requirements for an advanced degree at Idaho State University, I agree that the Library shall make it freely available for inspection. I further state that permission for extensive copying of my thesis for scholarly purposes may be granted by the Dean of the Graduate School, Dean of my academic division, or by the University Librarian. It is understood that any copying or publication of this thesis for financial gain shall not be allowed without my written permission.

Signature\_\_\_\_\_

Date\_\_\_\_\_

Radiation-Induced Optical Absorption In High Purity Synthetic Fused  
Silica

by

Justin Gahley

A thesis

submitted in partial fulfillment

of the requirements for the degree of

Master of Science in the Department of Physics

Idaho State University

Summer 2022

# Committee Approval

To the Graduate Faculty:

The members of the committee appointed to examine the thesis of Justin Gahley find it satisfactory and recommend that it be accepted.

---

Dr. Dustin McNulty

Major Advisor

---

Dr. Dan Dale

Committee Member

---

Dr. David Delehanty

Graduate Faculty Representative

*Dedicated to my children Vanessa, Jaden, Braxton, and Eli. You can do anything you  
decide you can.*

# Acknowledgments

This thesis is the result of over a year and a half of effort and dedication on the part of many individuals. During this experiment and as an undergraduate and graduate student, I have received advice, support, guidance, and mentorship, above and beyond the call of a graduate advisor from Dustin McNulty. Your help and encouragement have been invaluable in the implementation and completion of this experiment, this thesis, my work as a graduate student, and in life. Thank you for everything.

In addition, much of this work was done with the tremendous support of the employees at the Idaho accelerator center Chad O'Neil, Kevin Folkman, and Jon Stoner. Your knowledge, patience, and willingness to help were critical to our success; thank you. I want to thank Mason Jausii, the ISU radiation safety officer, for all of your time, advice, and suggested reading. They were great help with our dosimetry and the cesium calibrations. And a special thanks to Brian Berls for the countless hours spent going over dosimetry, working on equipment, help with our cesium calibrations, and probably several other things I am forgetting because you did so much over the last year and a half I can't thank you enough.

When we ran the experiments at the IAC, two undergraduates filled out our beamday team. Colton Fischer and Kouassi Freddy Kouakou, thank you for all your help with the data collection, dosimetry, and coding. You guys made the experiment possible. Without you, we could not have done it. Thanks to Mitchell Frasure, who came in towards the end and helped with the 3D printing. And thanks to Connor Harper, whose footsteps we followed in the dosimetry; thank you for answering questions, giving us your simulation, and always

being there to help.

Finally, I would like to thank Linards Skuja, your guidance with the NBOHC defect and other suggestions that made us pause and do more research before completing this thesis.

Thank you for taking the time to answer a student's emails.

# TABLE OF CONTENTS

List of Figures	xii
List of Tables	xiii
Abstract	xiii
<b>1 Introduction</b>	<b>1</b>
<b>2 Background and Theory</b>	<b>3</b>
2.1 MOLLER . . . . .	3
2.1.1 MOLLER Background . . . . .	5
2.1.2 Cherenkov Radiation . . . . .	6
2.1.3 Cherenkov Detectors and TIR . . . . .	8
2.2 High Purity Synthetic Fused Silica . . . . .	10
2.2.1 From Silicone Dioxide to HPFS . . . . .	10
2.3 Absorption Centers . . . . .	13
2.3.1 Theory . . . . .	13
2.3.2 Chemical Structure . . . . .	17
2.3.3 E'-center . . . . .	19
2.3.4 Non-bridging Oxygen Hole Center . . . . .	20
2.3.5 Peroxy Radical Center . . . . .	20
2.3.6 Other Centers . . . . .	21
2.4 Dose . . . . .	22

2.4.1	Dose Background . . . . .	22
2.4.2	Geant 4 Simulation . . . . .	24
2.4.3	Optically Stimulated Luminescence (OSL) . . . . .	25
2.5	Light Transmission . . . . .	25
<b>3</b>	<b>Experimental Setup</b>	<b>28</b>
3.1	Equipment and Materials . . . . .	29
3.1.1	Light Transmission Apparatus . . . . .	30
3.1.2	Accelerator . . . . .	38
3.1.3	Dosimetry Materials . . . . .	40
3.2	Methods . . . . .	42
3.2.1	Beamline Setup . . . . .	43
3.2.2	Light Transmission Loss Procedure . . . . .	45
3.2.3	Dose Calculation . . . . .	46
3.2.4	G4 Simulation . . . . .	47
<b>4</b>	<b>Results and Discussion</b>	<b>50</b>
4.1	Light Transmission . . . . .	50
4.1.1	Sources of Error . . . . .	50
4.1.2	Results . . . . .	51
4.2	Dose . . . . .	59
4.2.1	G4 Simulation Results . . . . .	60
4.2.2	Charge . . . . .	62
4.2.3	nanoDot OSLD Results . . . . .	62
4.2.4	Dose Results . . . . .	63
4.3	Intensity Loss by Dose . . . . .	64
4.4	Absorption Centers . . . . .	67
4.5	General Discussion . . . . .	71

<b>5 Conclusion</b>	<b>74</b>
<b>A Error Propagation</b>	<b>80</b>
<b>B Cesium-137 Measurements</b>	<b>84</b>
B.0.1 Equipment used . . . . .	85
B.0.2 Methods . . . . .	85
B.0.3 Results and Conclusions . . . . .	86
B.1 OSL Calibration measurements . . . . .	89
<b>C Beam Characterization</b>	<b>91</b>

# LIST OF FIGURES

Figure 2.1	MOLLER Detector System . . . . .	4
Figure 2.2	Cherenkov Radiation . . . . .	7
Figure 2.3	TIR . . . . .	9
Figure 2.4	DIRC . . . . .	9
Figure 2.5	Phase Diagram of Quartz . . . . .	11
Figure 2.6	Phases of SiO <sub>2</sub> . . . . .	12
Figure 2.7	HPFS . . . . .	12
Figure 2.8	Irradiated Glass . . . . .	13
Figure 2.9	Franck-Condon Diagram . . . . .	14
Figure 2.10	Structure of Quartz . . . . .	18
Figure 2.11	HPFS Rings . . . . .	18
Figure 2.12	POR . . . . .	21
Figure 2.13	Dose Depth Profile . . . . .	23
Figure 3.1	Light Transmission App. Diagram . . . . .	29
Figure 3.2	Light Transmission App. . . . .	30
Figure 3.3	Deuterium Lamp . . . . .	32
Figure 3.4	Spectrometer . . . . .	33
Figure 3.5	Spectrometer . . . . .	34
Figure 3.6	Spectrometer Eff. . . . .	34
Figure 3.7	Fiber optics . . . . .	35

Figure 3.8	Lens . . . . .	36
Figure 3.9	HPFS Holders . . . . .	37
Figure 3.10	Beamline HPFS Stand . . . . .	38
Figure 3.11	Linear Accelerator . . . . .	38
Figure 3.12	Linear Accelerator Specifications . . . . .	39
Figure 3.13	Accelerator Equipment . . . . .	39
Figure 3.14	Pearson Coil & Oscill... . . . .	40
Figure 3.15	nanoDot Picture . . . . .	41
Figure 3.16	nanoDot Diagram . . . . .	41
Figure 3.17	nanoDot equipment . . . . .	42
Figure 3.18	45°Port . . . . .	44
Figure 3.19	Beam Alignment . . . . .	44
Figure 3.20	Geant 4 Sim... . . . .	49
Figure 4.1	Light Source Fluctuation . . . . .	51
Figure 4.2	RMS in Background Intensity . . . . .	52
Figure 4.3	Light Loss by Energy Sept. . . . .	53
Figure 4.4	Absorption Coeff. Sept. . . . .	54
Figure 4.5	Light Loss by Wavelength Sept. . . . .	55
Figure 4.6	Light Loss by Energy March . . . . .	56
Figure 4.7	Absorption Coeff. March . . . . .	57
Figure 4.8	Light Loss by Wavelength March . . . . .	58
Figure 4.9	OSLD/HPFS Cartoon . . . . .	59
Figure 4.10	Simulated dose conversion . . . . .	61
Figure 4.11	Varied beam parameters . . . . .	61
Figure 4.12	Charge Distribution . . . . .	62
Figure 4.13	nanoDot Calibration Fit . . . . .	63

Figure 4.14 Intensity Loss by Dose . . . . .	65
Figure 4.15 Intensity Losses for All samples . . . . .	67
Figure 4.16 Absorption Bands . . . . .	70
Figure 4.17 POR Peak . . . . .	71
Figure A.1 RMS in Background Intensity . . . . .	81
Figure A.2 Light Source Fluctuation . . . . .	82
Figure A.3 Uncertainty in % loss . . . . .	83
Figure B.1 Exposure Measurements . . . . .	85
Figure B.2 Cesium Source . . . . .	86
Figure B.3 Ion-Chamber . . . . .	86
Figure B.4 Oct. Exposure Measurements 1 . . . . .	87
Figure B.5 Oct. Exposure Measurements 2 . . . . .	87
Figure B.6 Activities . . . . .	88
Figure B.7 OSLs Array Cs-137 . . . . .	89
Figure C.1 Irradiated Glass . . . . .	92
Figure C.2 Glass Slide Distributions . . . . .	93
Figure C.3 Sim. & Real optimization 1 . . . . .	93
Figure C.4 Sim. & Real optimization 2 . . . . .	94
Figure C.5 Sim. & Real Comparison . . . . .	94
Figure C.6 Dose Depth and HPFS . . . . .	95

# LIST OF TABLES

Table 2.1	Common point defects in HPFS . . . . .	22
Table 4.1	Dose by Run . . . . .	64
Table 4.2	Dose by Run . . . . .	64
Table 4.3	Intensity Loss March . . . . .	66
Table 4.4	Intensity Loss Sep. . . . .	66
Table B.1	OSL Calibration Times . . . . .	90

# Radiation-Induced Optical Absorption In High Purity Synthetic Fused Silica

Thesis Abstract–Idaho State University (2022)

A Cherenkov detector made with high purity synthetic fused silica (HPFS) will experience light signal losses if exposed to ionizing radiation. This experiment quantifies these losses with a precision  $\lesssim 0.5\%$  in five HPFS samples. The doses range from  $\sim 5$  to  $\sim 177$  Mrad  $\pm 8\%$  in a  $5 \times 5 \times 10$  mm<sup>3</sup> section of the samples. Our results show quantifiable differences in losses between the samples as a function of dose. The Heraeus Spectrosil 2000 H<sub>2</sub> doped brand showed the least loss, while the Heraeus Spectrosil 2000-standard is the worst, showing the most damage.

These light losses are due to the generation of absorption centers. Although hundreds of studies have characterized many centers, there is still uncertainty about the location of some, such as the peroxy radical center (POR). This study also argues for a possible bulk absorption peak of the peroxy radical absorption center at  $\sim 5.3$  eV.

Key Words: high purity synthetic fused silica; radiation; optical absorption; peroxy radical center; Cherenkov detector; nanoDot OSLD.

# Chapter 1

## Introduction

An upcoming experiment called MOLLER (Measurement of a Lepton-Lepton Electroweak Reaction), aims to make the most precise measurement of a parity-violating asymmetry ( $A_{PV}$ ) in electron-electron scattering to date. This measurement will probe the accuracy of the Standard Model of Physics through indirect access to potential new physics at the MeV to multi-TeV scale<sup>[1]</sup>. But this achievement, at least partly, relies on the choice of the detector system. The primary detectors in MOLLER will be directly integrating Cherenkov detectors (DIRCs), made with high purity synthetic fused silica (HPFS) radiators. HPFS material was chosen in part because of its “radiation hardness”. Resistance to radiation damage is essential for MOLLER due to the anticipated high levels of ionizing radiation exposure to the detector radiators over the experiment’s lifetime. However, despite the HPFS’s enhanced resistance to radiation damage, large amounts of deposited energy density (dose or absorbed dose) cause the creation of optical absorption bands, which absorb light in the ultraviolet regions of the Cherenkov spectrum. Therefore, to understand the effects of dose on the performance of the MOLLER detector systems, quantifying light losses from these absorption bands is of significant interest.

Although many of these absorption bands have been studied in detail, the prevailing literature primarily focuses on characterizing the bands and associated “defect-centers”.

The connection from the literature to a relative signal loss that a Cherenkov detector might experience is less clear. In addition, studies that have attempted to make this connection have shown mixed results<sup>[2,3]</sup>, with unclear dose calculations and no relation to absorption centers. So the primary question is posed, how much light transmission loss can one expect as a function of dose in our HPFS radiator tiles?

Also, do transmission losses vary across different brands of HPFS? Many companies produce comparable HPFS tiles, but no information can predict which brand or type is the most radiation hard. In addition, the Heraeus company has a product that introduces high levels of molecular hydrogen ( $H_2$ ), which may increase its radiation hardness. So, which brands are better, and does the  $H_2$  doped Heraeus product have an improved radiation hardness?

Any differences in light transmission found between the HPFS brands directly result from the absorption centers generated. Despite a large number of studies, there is still some uncertainty about what centers may be present<sup>[4,5]</sup>. In particular, the absorption center from the “peroxy radical” (POR) defect is not well described. So, what absorption centers can be found in these modern HPFS brands, what role do they play in the overall light transmission loss, and can anything new be found about the POR?

This thesis examines the optical transmission losses due to ionizing radiation in five types of HPFS samples using a custom-made apparatus. It also investigates the absorption bands present in the samples, and determines whether or not the  $H_2$  doped Heraeus product has an enhanced radiation hardness. In addition to the optical measurements, we determine the dose on our samples at the 8 % level using measurements from optically stimulated luminescent dosimeters (OSLDs) combined with Geant4 (G4) simulations.

We present background information and theoretical models in Chapter 2. We describe our equipment and procedures in Chapter 3. Chapter 4 presents our results and a discussion of our findings. And finally Chapter 5 has our conclusions.

# Chapter 2

## Background and Theory

This Chapter covers the background information on the physics involved. Section 2.1 details the MOLLER experiment with descriptions of Cherenkov radiation and the Cherenkov detectors used. Section 2.2 explains what HPFS is, how it is made, and its physical characteristics. Section 2.3 gives a first principles derivation on the theory of absorption in defect centers, their creation, and chemical structures. Section 2.4 covers dose, how it works, how we use simulation, and details of optically stimulated luminescence. Finally, Section 2.5 defines light transmission loss and how we use it in this experiment.

### 2.1 MOLLER

The primary purpose of this experiment is to quantify the transmission loss of optical photons in irradiated HPFS tiles for use in the MOLLER experiment. These tiles will be used as Cherenkov radiators in multiple rings that comprise the entire detector system. Figure 2.1 displays a visualization of these rings of detectors. This Section briefly describes the detectors, the MOLLER experiment, and Cherenkov radiation.

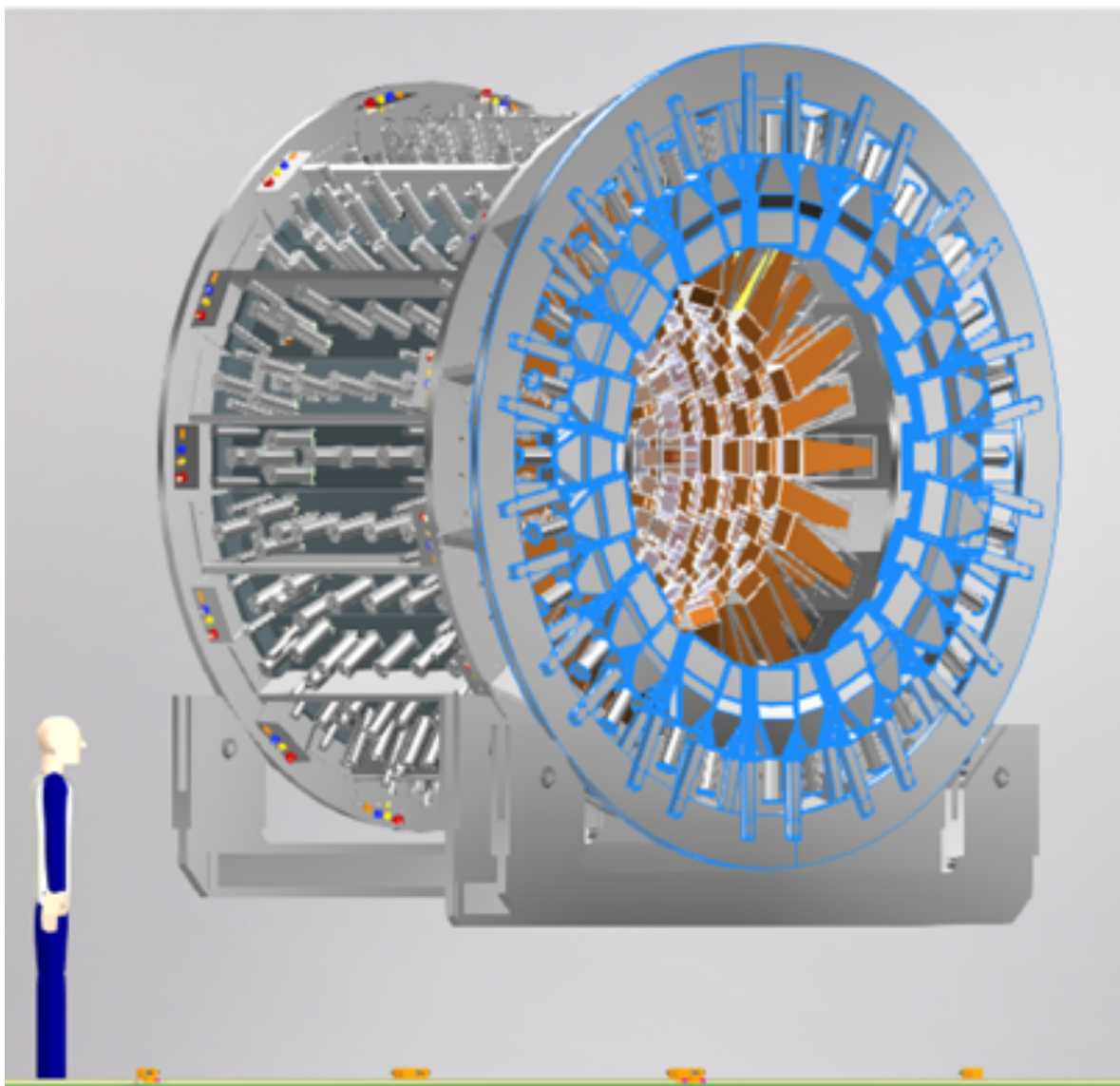


Figure 2.1: The MOLLER detector system. The main detector consists of 224 HPFS tiles over 6 concentric rings. Downstream of these rings is a ring of 28 Shower-max detectors (highlighted), each with 4 HPFS tiles.

### 2.1.1 MOLLER Background

The weak mixing angle ( $\theta_W$ ), also known as the “Weinberg angle”, is a free parameter of electroweak theory with extremely low theoretical uncertainty. Our precise understanding of the value of this parameter makes it a desirable candidate for probing the completeness of the Standard Model (SM) of particle physics and has been the subject of measurement in several past experiments, such as SLAC E158<sup>[6]</sup>. Backed by the group experience of four generations of parity-violating experiments, the MOLLER collaboration proposes to improve upon the E158 measurement by a factor of five. To achieve this level of precision, the experiment will implement a sophisticated system of nearly 300 individual integrating detectors of different types, as shown in Figure 2.1.

The MOLLER experiment proposes to measure a rate asymmetry from the scattering of longitudinally spin-polarized beam electrons with unpolarized target electrons (Møller scattering). The longitudinal beam polarization is flipped between right and left-handed helicity states at 960 Hz throughout the experiment. The scattered flux through the detector radiators creates the Cherenkov signal, which is integrated over a given beam polarization (or helicity) state.

The measured asymmetry ( $A_{meas}$ ) results from parity symmetry violation in the weak interaction and is expressed as

$$A_{meas} \equiv \frac{\sigma_R - \sigma_L}{\sigma_R + \sigma_L}, \quad (2.1)$$

where  $\sigma_R$  and  $\sigma_L$  are the cross-sections for right and left-handed polarized incident electrons. Essentially, the asymmetry is a measure of how many more (or less) interactions happen for right versus left polarized electrons<sup>[1]</sup>. After corrections are applied to the measured asymmetry, it is used to determine the parity violating physics asymmetry ( $A_{PV}$ ). From this one can determine the weak charge of the electron,  $Q_W^e$ , or weak mixing angle ( $\theta_W$ ) using the expression

$$A_{PV} = m_e E \frac{G_f}{\sqrt{2}\pi\alpha} \frac{4\sin^2(\theta_W)}{3 + \cos(\theta_W)} Q_W^e, \quad (2.2)$$

where  $m_e$  is the mass of an electron,  $E$  is the beam energy,  $G_f$  is the Fermi coupling constant for the weak interaction, and  $\alpha$  is the fine structure constant. The extracted weak mixing angle can then be compared to the Standard Model prediction at the kinematics of MOLLER.

The MOLLER experiment will run at Thomas Jefferson National Accelerator Facility (JLab) using an 11 GeV longitudinally polarized electron beam with several “main” detector rings at different radii. These detectors are then used to make the actual  $A_{PV}$  measurement. There are six rings of these main integrating detectors plus an additional ring with a detector called Shower-Max, which is of novel design<sup>1</sup>. All of these are called detectors of internally reflected Cherenkov (DIRC). Due to concerns such as cost, complexity, and radiation hardness<sup>2</sup>, and internal reflection HPFS was chosen as the Cherenkov radiators. Cherenkov radiation and its detection is briefly explained in the next Section.

### 2.1.2 Cherenkov Radiation

DIRCs work by measuring internally reflected Cherenkov radiation coming from a radiator. But what is Cherenkov radiation (or light), and how is it detected?

Cherenkov light is electromagnetic radiation emitted from a charged particle traveling faster than the phase velocity of light in a dielectric medium. It is analogous to the sonic boom effect in air when objects travel faster than the speed of sound. As a photon enters a medium that has electric and magnetic polarizability, the velocity of the light changes, this new velocity is called its phase velocity ( $v_p$ ) in that medium. The ratio of its  $v_p$  and the propagation velocity in vacuum is called the index of refraction ( $n$ ) and is typically greater than one. In most materials,  $n$  is wavelength dependent (or equivalently frequency

---

<sup>1</sup>Created by our group here at ISU

<sup>2</sup>This term means it is resistant to ionizing radiation. In this case it means the material’s transparency is resistant to degradation.

dependent). For photons, the propagation velocity in vacuum is the speed of light  $c$ ,  $n$  is then given by

$$\frac{c}{v_p} = n. \quad (2.3)$$

As a charged particle travels through a medium, the particles and molecules in that medium polarize around it and become excited. When they relax back to the ground state, they emit some of the energy they received from the traveling charged particle in the form of spherical electromagnetic wavefronts, as in the Huygens' principle. When the charged particle travels at velocities less than  $v_p$  the emitted waveforms do not interfere or overlap. However, if the charged particles have a velocity greater than  $v_p$  they overlap and constructively interfere, which causes the cone-like electromagnetic propagation at the characteristic angle  $\theta_{ch}$  called the Cherenkov angle. Figure 2.2 depicts an example of Cherenkov radiation.

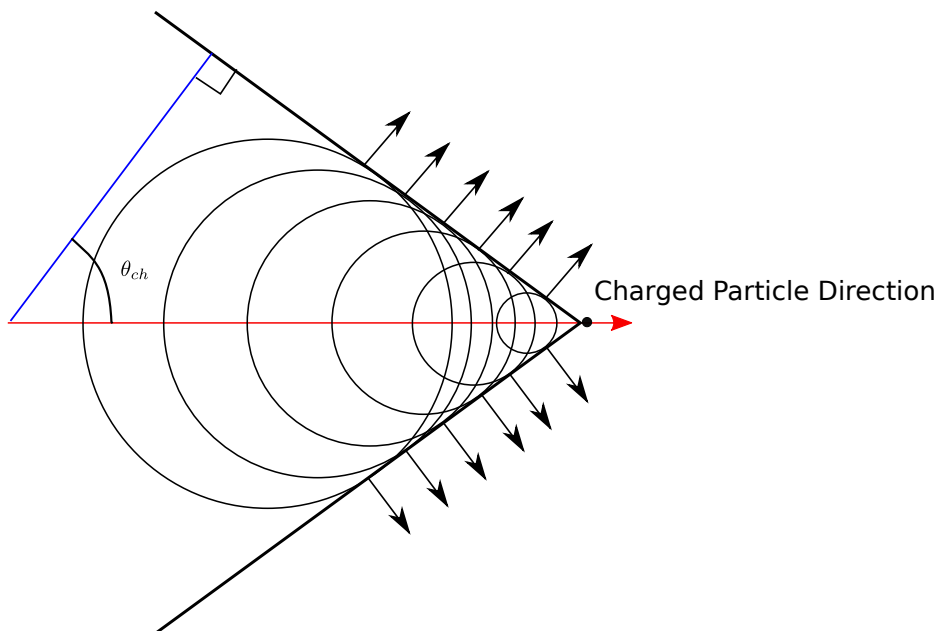


Figure 2.2: Diagram of Cherenkov radiation. The Cherenkov wavefront propagates in the direction of the black arrows, at  $\theta_{ch}$  relative to the charged particle trajectory.

Pavel Cherenkov first discovered this type of radiation and won a Nobel prize with Igor

Tamm and Ilya Frank, who developed its theory. The Frank-Tamm formula, which characterizes the Cherenkov radiation spectrum, is

$$\frac{\partial^2 E}{\partial x \partial \omega} = \frac{q^2}{4\pi} \mu(\omega) \omega \left(1 - \frac{c^2}{v^2 n^2(\omega)}\right), \quad (2.4)$$

where  $E$  is the energy of the charged particle,  $q$  is its electric charge,  $\omega$  is the frequency of light,  $\mu(\omega)$  and  $n(\omega)$  are the frequency dependent permeability and index of refraction (respectively),  $x$  is the distance in the material,  $v$  is the velocity of the charged particle, and  $c$  the speed of light in vacuum. This yields a continuous spectrum with peak intensities in the ultraviolet (UV) region<sup>3</sup>.

### 2.1.3 Cherenkov Detectors and TIR

Directly integrating Cherenkov detectors (DIRCs) for MOLLER take advantage of HPFS's nearly total internal reflection (TIR) properties. TIR is an optical phenomenon in which light waves arriving at a boundary between two media do not transmit, but reflect into the first medium. TIR is often explained using light rays instead of waves; as the incident angle of the light ray approaches the critical angle ( $\theta_{cr}$ ), the refracted beam approaches 90 degrees; once the incident beam passes the  $\theta_{cr}$  the ray is totally internally reflected (see Figure 2.3). Note that even at angles below  $\theta_{cr}$  there is a small amount of reflection.

In a DIRC, the reflected Cherenkov light eventually exits at a beveled end, where the angle of incidence is less than  $\theta_{cr}$ . The light is then directed to a photomultiplier tube (PMT); in the case of MOLLER, the light is funneled by an air-core light guide to a PMT. Figure 2.4 illustrates this process. TIR is one property of HPFS that makes it a desirable candidate for the MOLLER experiment.

---

<sup>3</sup>This is the same region that peak damage in HPFS receive from ionizing radiation, hence the need to understand and characterize these losses in this experiment.

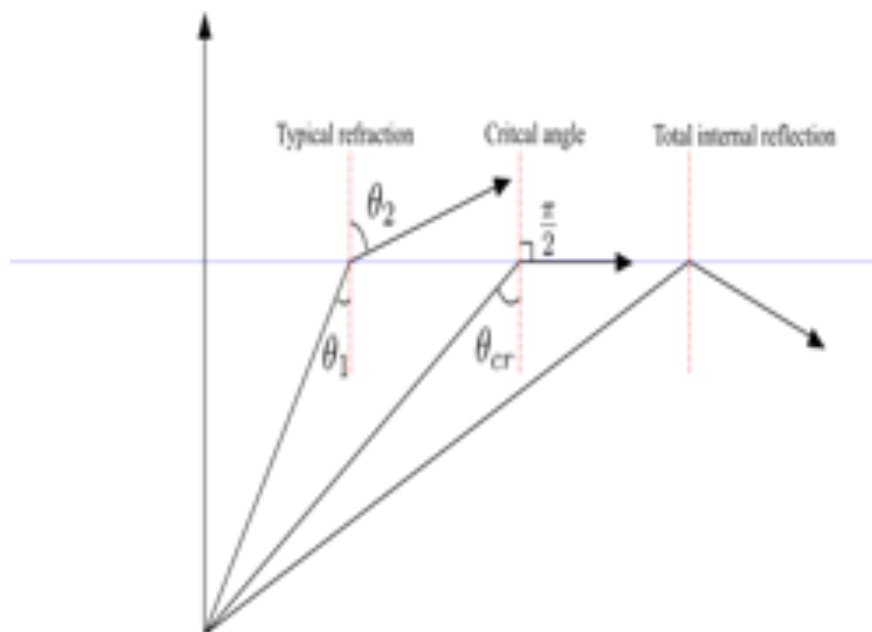


Figure 2.3: Total internal reflection diagram assuming index of refraction above blue line is less than the one below. For angles less than  $\theta_{cr}$ , the light exits the HPFS.

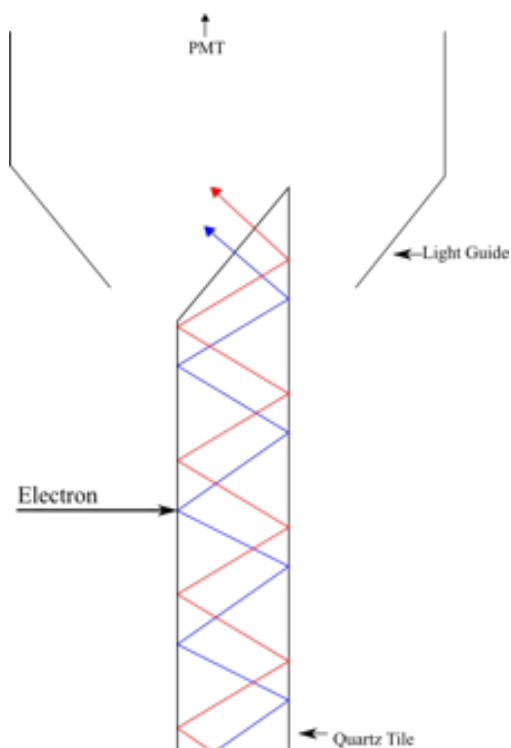


Figure 2.4: Detector of internally reflected Cherenkov radiation (DIRC). This shows an HPFS tile or bar with bevel at one end. The blue and red rays depict a 2D slice of the Cherenkov cone photon paths. TIR enables  $\sim$  all the Cherenkov light, theoretically, to be captured.

## 2.2 High Purity Synthetic Fused Silica

### 2.2.1 From Silicone Dioxide to HPFS

Silicon dioxide ( $\text{SiO}_2$ ) is the most abundant chemical compound found in Earth's rocks, and soils<sup>[7]</sup>. It is also the most common ingredient for many glasses. Silica glasses are highly transparent amorphous solids made by heating  $\text{SiO}_2$  then rapidly cooling. The heating and rapid cooling (called vitrification) prevent the material from re-crystallization and leave it in an amorphous “glassy” state. Fused silica is a pure form of glassy silica (without additives found in household glasses).

Fused silica is made by heating quartz in its natural crystalline form,  $\alpha$ -quartz (trigonal crystalline form), which then transitions to polymorphs  $\beta$ -quartz (hexagonal crystalline structure), HP-tridymite (Hexagonal),  $\beta$ -cristobalite (Tetragonal), and after 1713 °C into a liquid with a highly randomized structure. The material is then rapidly cooled, freezing this structure into an amorphous network with no long-range order called fused silica (or a- $\text{SiO}_2$ )<sup>[8]</sup>. Figures 2.5 and 2.6<sup>4</sup> show the phase diagram, molecular structure, and pictures of some phases.

Making fused silica from natural quartz often leads to large amounts of impurities affecting the transparencies and radiation hardness in the UV-Vis ranges. Instead, starting with silicon tetra-chloride yields high purity synthetic fused silica (referred to as HPFS, quartz, fused silica, and or synthetic fused silica interchangeably), characterized by low levels of impurities, radiation hardness, and high transparency in the UV-Vis region.

HPFS is made by burning silicon tetra-chloride, producing silicate nano-particles called “soot”. This soot is then deposited onto a substrate and made into the desired end products using different techniques such as chemical vapor deposition (CVD), plasma outside deposi-

---

4



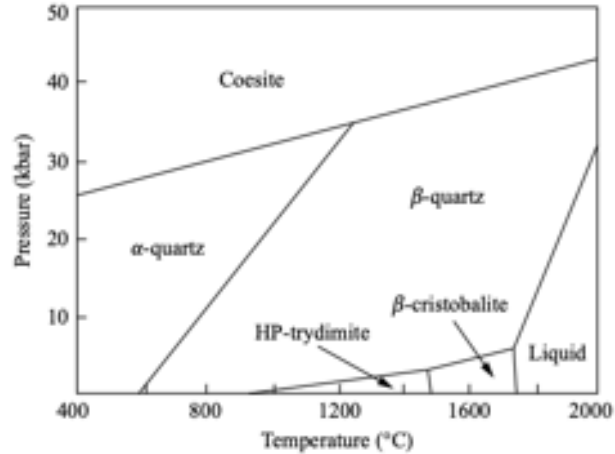


Figure 2.5: Phase diagram of silicon dioxide<sup>[8]</sup>.

tion (POD), outside vapor deposition (OVD), and vapor axial deposition (VAD). VAD is the process typically used to make the HPFS tiles like the ones used in this experiment. VAD involves depositing the soot to the end of a rod while it is pulled upwards; this creates a porous soot body that is then vitrified to produce HPFS<sup>[16]</sup>. After the manufacturing process, the HPFS is optically polished. The end product is highly transparent, thermal shock and scratch resistant, and is radiation hard compared to other forms of quartz. Figure 2.7 has a photograph of a finished sample used in this experiment.

Adding extra hydroxyl groups (OH) during HPFS production can increase its radiation resistance; this creates what is called “wet” synthetic fused silica. Any OH content higher than 200 ppm is considered wet; everything less is called “dry”. Besides OH, molecular hydrogen (H<sub>2</sub>) can also be “doped” into a sample, leaving a high interstitial H<sub>2</sub> content. All of our samples would be considered wet, except for the O’Hara SK-1300. Moreover, one type of the Heraeus Spectrosil-2000 has been doped with H<sub>2</sub>. Section 3.1.1 discusses these and all brands of HPFS used in this experiment.

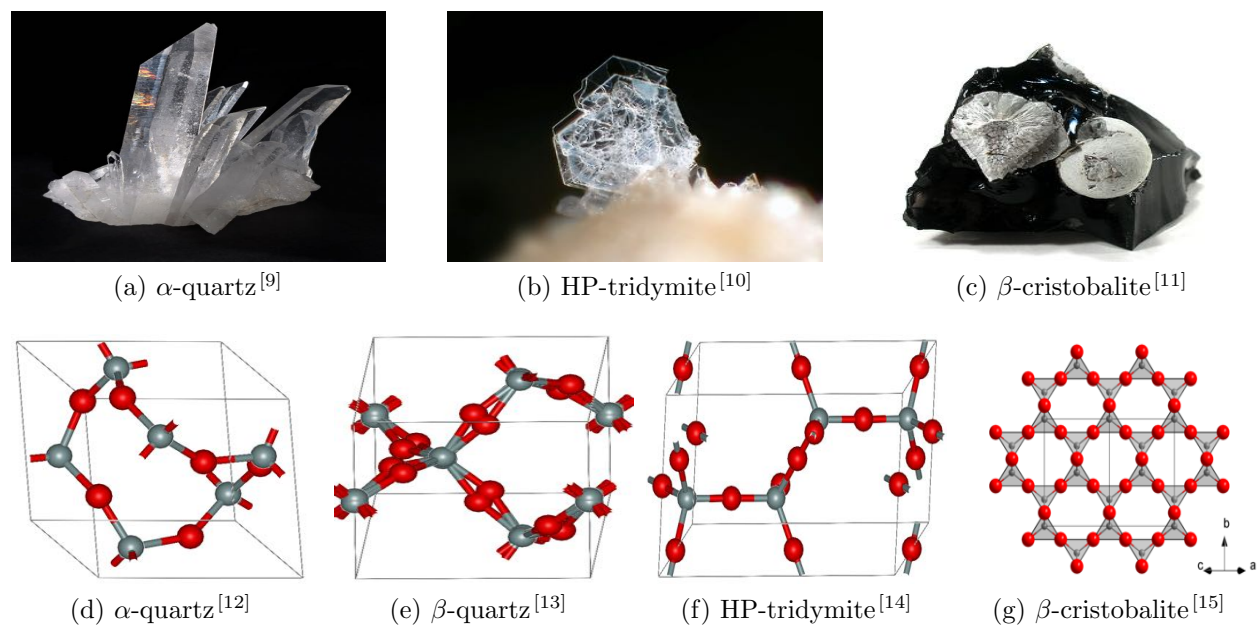
Figure 2.6: Different phases of  $\text{SiO}_2$ 

Figure 2.7: HPFS sample inside a custom holder designed for our radiation hardness tests.

## 2.3 Absorption Centers

Ionizing radiation causes the formation of defects in HPFS. These defects act as absorption centers and result in the light transmission losses found in the experiment. This Section gives background information on the theory of their optical structure and descriptions of their chemical structure.

### 2.3.1 Theory

What is an absorption center? To understand this better, let us look at the glass slide in Figure 2.8. Following its irradiation, light does not pass through the glass as before, and it looks blackish/brown where the beam hits it. What has happened is that the particles passing through the glass damaged some of its chemical bonds. These damaged areas now have a structure that will absorb specific wavelengths of light. Kun Huang and Avril Rhys originally proposed the theory that explains this electromagnetic absorption in these types of damaged centers<sup>[17]</sup>. In this thesis, we make no first principle calculations but provide the following derivation for informational purposes.

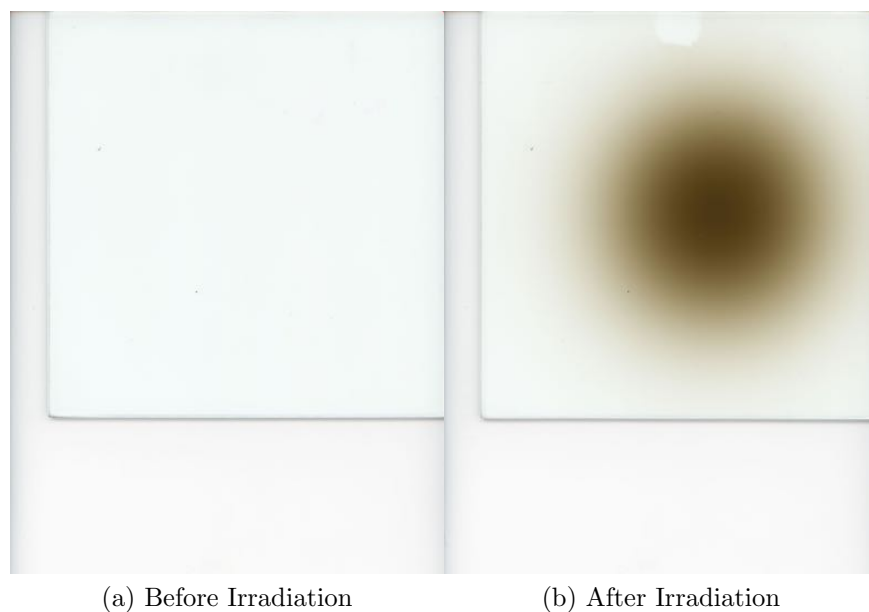


Figure 2.8: Scan of a glass slide before and after irradiation with 8 MeV electron beam.

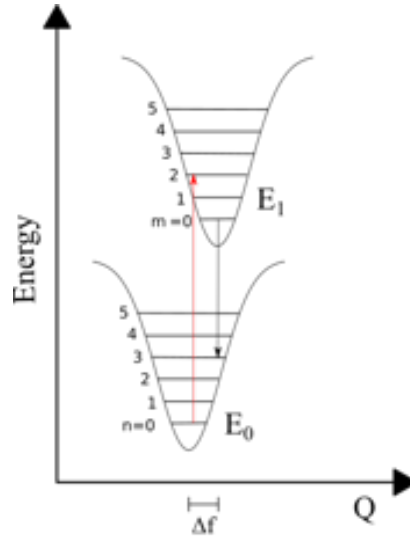


Figure 2.9: Franck-Condon diagram.  $E_0$  is the ground state of the system;  $E_1$  is the excited state.  $\Delta_f$  is the change in the equilibrium position (normal nuclear coordinates) of the atoms in the system.

At the most fundamental level, the photons traveling through these damaged centers are “absorbed” by causing vertical vibronic (simultaneously electronic and vibrational) energy transitions according to the Franck-Condon principle (see Figure 2.9). If the incident photon energy  $E_{1,0}$  matches the quantum transition between the ground and excited state,  $E_{1,0} = E_1 - E_0$ , then the absorption coefficient through a unit path length is given by<sup>[18]</sup>.

$$\alpha(E) = \ln\left(\frac{I_0(E)}{I(E)}\right) = \frac{N_0\pi E}{3\hbar^2 E_0 c} |R_{1,0}|^2 \delta(E - E_{1,0}), \quad (2.5)$$

where  $N_0$  is the number of identical non-interacting absorbers per unit volume in the ground state.  $R_{1,0}$  is the quantum mechanical matrix element of the electric dipole moment,  $M$ , between the total eigenfunctions  $\psi_0$  and  $\psi_1$  of the ground and excited state, respectively (called the transition moment).

$$|R_{1,0}|^2 = |\langle \psi_1 | M | \psi_0 \rangle|^2. \quad (2.6)$$

Using the Born-Oppenheimer approximation we can treat the electronic and vibrational wavefunctions separately as

$$\begin{aligned}\psi_0(r, Q) &= \phi_0(r, Q)\varphi_0(r, Q) \quad \text{and} \\ \psi_1(r, Q') &= \phi_1(r, Q')\varphi_1(r, Q'),\end{aligned}\tag{2.7}$$

where  $\phi$  is the electronic wavefunction, and  $\varphi$  is the vibrational. Note that in the excited state there is an equilibrium shift ( $\Delta_f$ ) hence the change in normal nuclear coordinates from  $Q$  to  $Q'$ <sup>[19]</sup>. The dipole moment can be split into an electronic term  $M_{el}$  and a nuclear term  $M_{nuc}$ . Integrating over the electronic ( $d\tau_e$ ) and vibrational ( $d\tau_\mu$ ) spaces,  $R_{1,0}$  then becomes

$$\begin{aligned}R_{1,0} &= \int \phi_1^*(r, Q')M_{el}(r)\phi_0(r, Q)d\tau_e \times \int \varphi_1^*(r, Q')\varphi_0(r, Q)d\tau_\mu \\ &+ \int \phi_1^*(r, Q')\phi_0(r, Q)d\tau_e \times \int \varphi_1^*(r, Q')M_{nuc}(Q)\varphi_0(r, Q)d\tau_\mu.\end{aligned}\tag{2.8}$$

Because nuclei are almost stationary between the ground and excited states, we can use the Condon approximation that  $\phi$  depends on  $Q = Q_0$ , then by orthogonality the second term vanishes. The integral  $\int \varphi_1^*(r, Q')\varphi_0(r, Q)d\tau_\mu$  is known as the Franck-Condon integral, it measures the overlap of the vibrational eigenfunctions. If there is no coupling<sup>5</sup> between the electronic and vibrational eigenfunctions, then the normal nuclear coordinates coincide, meaning  $Q = Q'$  ( $\Delta_f = 0$ ). And by orthogonality, only terms with the same quantum numbers ( $m_f = n_f$ ) contribute. If there is coupling than all terms contribute.

Due to the finite lifetime  $\tau$  of an excited state, the  $\delta$  function can be replaced with a Lorentzian shape function  $\frac{\Gamma}{(E-E_{1,0})^2+\Gamma^2}$ . And when the temperature  $T = 0$  K, only the  $n_f = 0$  vibrational level of the ground electronic state can be occupied. In this case we can rewrite 2.5 as

---

<sup>5</sup>This means that the systems are bound to each other in such a way that a change in one system creates a change in the other system

$$\alpha(E, T = 0) = M_0 E \sum_{(m_f)} \left[ \left( \prod_{f=1}^{N_f} e^{-S_f} \frac{S_f^{m_f}}{m_f!} \right) \frac{\Gamma}{(E - E_{00} - h \sum_{f=1}^{N_f} m_f \nu_f)^2 + \Gamma^2} \right], \quad (2.9)$$

where  $E_{00}$  represents the energy difference between the  $m_f = 0$  in the excited state and the  $n_f = 0$  in the ground state.  $S_f$  is the Huang-Rhys factor;  $S_f = \frac{h\nu_f}{2} \Delta_f^2$  measures the coupling strength between the electronic transition, from ground to excited state, and the  $f^{th}$  vibrational mode. And  $M_0 = \frac{N_0 \pi}{3\hbar^2 E_0 c} |R_{1,0}|^2$ .

Looking at a temperature range from  $T_{min}$  to  $T_{max}$ , where  $T_{max}$  is an imposed upper limit, it is possible to distinguish between high frequency vibrational modes ( $\nu_h$ ) and low frequency modes ( $\nu_l$ ). Where  $\nu_h$  only have frequencies such that  $h\nu_h \gg k_B T_{max}$  ( $k_B$  is the Boltzmann constant). So that only  $n_h = 0$  is occupied in temperatures up to  $T_{max}$ . This implies that all of the  $N_h$  high frequency modes will only transition from  $n_h = 0$  in the ground electronic state to  $m_h = 0, 1, 2, \dots$  in the excited state. On the other hand the low frequency modes can vary their transitions across changing temperatures. Treating the combination of the  $N_l$  low frequency modes as an Einstein oscillator, that is a single mode with a single average frequency  $\langle \nu_l \rangle$  and an average coupling constant  $S_l$ . We can then convolve equation 2.3.1 with a Gaussian to include temperature dependence,  $\frac{1}{W(T)} e^{-\frac{E^2}{2W^2(T)}}$ , where  $W^2(T) = N_l S_l h^2 \langle \nu_l \rangle^2 \coth \frac{h\langle \nu_l \rangle}{2k_B T}$ .

There are also contributions to absorption that arise from the different local environments of the point defects. This contribution comes from purely electronic transition energies  $E_{00}$ . This distribution is typically given by a Gaussian function  $g(E_{00}) = \frac{1}{(\sqrt{2\pi}\sigma_{inh})} e^{-\frac{(E_{00}-E'_{00})^2}{2\sigma_{inh}^2}}$ . This is also referred to as inhomogeneous broadening.

The energy and temperature dependent absorption coefficient can then generally be given by a Lorentzian function convoluted with the combination of two Gaussian functions. These functions are called ‘‘Voigtians’’ and are written as

$$\alpha(E, T) = L(E) \otimes G(E, T), \quad (2.10)$$

where  $L$  is the Lorentzian component,  $G$  is the combination of the Gaussian's and  $\otimes$  is the convolution operator. The total width of the distribution is then given by

$$W_{tot}^2 = W^2 + \sigma_{inh}^2. \quad (2.11)$$

For more information on this derivation please see<sup>[17,18]</sup>. This all indicates that absorption spectra can be expected to be approximately *Gaussian distributions* in energy. More recently, simulations have been used to make these calculations.

Experts now use *ab-initio* molecular dynamics simulations to make first principle calculations. The simulations can unify and numerically solve Newton's and Schrodinger's equations for many bodies by utilizing a second-generation version of the Car-Parrinello approach to Born-Oppenheimer molecular dynamics<sup>[20]</sup>. For more detail on *ab-initio* calculations and how the simulations work please see<sup>[20]</sup>.

### 2.3.2 Chemical Structure

The chemistry of HPFS consists primarily of  $\equiv \text{Si-O-Si} \equiv$  bonds where  $\equiv \text{Si}$  represents a silicon atom bonded to three oxygen atoms; Figure 2.10 shows a simulated section of HPFS. These bonds tend to form various sizes of "rings" as in Figure 2.11. A ring is the shortest closed path connecting two oxygen atoms bonded to the same silicon atom. For example,  $\alpha$ -quartz is entirely composed of six-part rings. The bond lengths and angles in a six-part ring have the lowest energy state and are therefore the most common found in any quartz<sup>[8]</sup>. However, HPFS because of its amorphous structure, has stable  $n$ -numbered rings ranging from  $n = 3 - 9$ , Si-O bonds.

The smaller the ring size, the more excess energy the bonds have. Under this model,

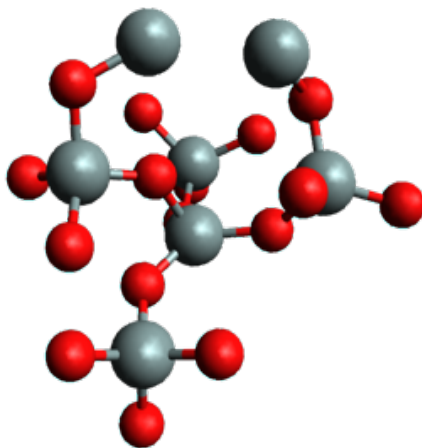


Figure 2.10: Amorphous structure of synthetic fused silica. At the top of the structure you can see two silicons with no oxygen bond bridging in-between them. This is an example of an oxygen deficient center (ODC) ( $\equiv \text{Si}\dots\text{Si} \equiv$ ). This is just one example of how the amorphous structure can lead to abnormal bonds or defect centers.

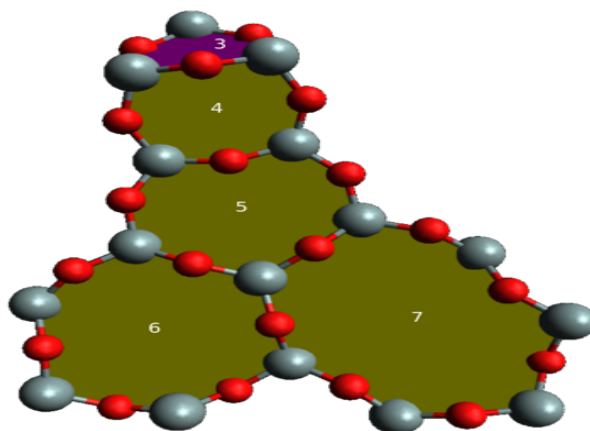
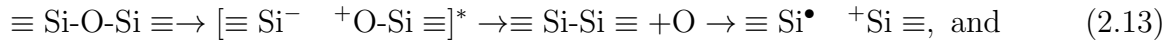
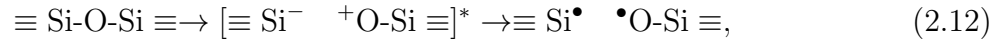


Figure 2.11: An example of different numbered rings that can be found in amorphous silica.

the 3, 4, and 5-part rings are more sensitive to ionizing radiation and tend to break into larger numbered rings. This breaking apart generates meta-stable point defects like the E'-center and the non-bridging oxygen hole center. In addition to the ring breaking mechanism, abnormal bonds (or lack of bond) can cause point defects like the peroxy radical center and the oxygen-deficient center. All of these defects are explained below, starting with the most significant.

### 2.3.3 E'-center

The E' absorption center is the most studied point defect<sup>[4,8,21-23]</sup> and gives the largest amount of absorption in most HPFS types. It has several variants: E'<sub>α</sub>, E'<sub>γ</sub>, and E'<sub>β</sub>. It is often called a dangling silicon bond, meaning that a three-bonded silicon has an unpaired spin. This is represented by ≡ Si•, where ≡ represents three oxygen atom bonds and Si• represents a silicon atom with an unpaired valence electron spin. The mechanisms of generation are thought to be



All E'-centers are thought to have similar electronic structures and therefore the same absorption bands centered around 5.7 – 5.8 eV. This means the absorption bands cannot be used to distinguish between variants, instead their electron paramagnetic resonance (EPR) signals are used.

### 2.3.4 Non-bridging Oxygen Hole Center

The first generation mechanism of the non-bridging oxygen hole center (NBOHC) is thought to be the breaking of a strained silicon oxygen bond exactly as in reaction 2.12. The second is the dehydrogenation of a silanol (Si-O-H) group



Until recently, this point defect was associated with an absorption band centered at 4.8 eV and a much smaller one at 1.9 eV. However, in 2011 Skuja et al.<sup>[5]</sup> was able to show a semi-continuous spectrum from 4 – 7.8 eV in addition to the 1.9 eV band. Somewhat unusually, they were able to study NBOHCs in a sample without the co-presence of E'-centers, which is difficult considering they are co-generated as in reaction equation 2.12. This is the second most prevalent defect center in HPFS.

### 2.3.5 Peroxy Radical Center

The peroxy radical (POR) is thought to be generated by



where  $\equiv \text{Si-O-O-Si} \equiv$  is called peroxy linkage as in Figure 2.12. This defect center's absorption spectra have been difficult to separate from the overlapping bands of the NBOHC and E'. Moreover, its peak location and contribution to the overall absorption is currently undetermined.

The proposed absorption centers are 5.1, 5.4 (on the surface), and 4.8 eV, with no consensus in the literature. Though it is thought this center is more likely to develop in oxygen-rich environments, such as in wet HPFS.

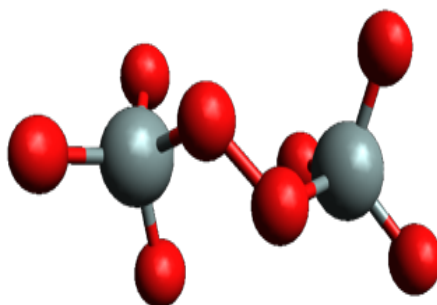


Figure 2.12: Peroxy linkage example. One can see the two oxygen atoms bonded together. This would be more likely found in an oxygen rich environment.

### 2.3.6 Other Centers

Another common point defect is the oxygen-deficient center (ODC) with two flavors: ODC(I) can refer to a  $\equiv \text{Si-Si} \equiv$  bond, or possibly two unbounded silicons  $\equiv \text{Si}\dots\text{Si} \equiv$ ; ODC(II) possibly refers to an oxygen vacancy or oxygen divacancy. These are thought to be more common in dry HPFS. The related absorption centers have peaks  $\sim 5.0, 6.8,$  and  $7.8$  eV.

Many other defect types can occur in HPFS and natural fused quartz, such as hydrogen hole centers  $\equiv \text{Si-H}^\bullet$ , interstitial  $\text{O}_2$  and  $\text{O}_3$ , silanone groups  $= \text{Si} = \text{O}$ , interstitial  $\text{Cl}_2$ , germanium related defects/impurities, and aluminum impurities. Typically absorption in the visible region is caused by impurities like aluminum<sup>6</sup>. However, these sources likely make small contributions to the overall absorption. For more information on any of these defects, a review of the topic can be found here<sup>[22]</sup>.

Table 2.1 summarizes the most prominent absorption centers found in HPFS and their likely structures. Ionizing radiation generates all of these point defects by depositing energy into the HPFS; this is called absorbed dose.

---

<sup>6</sup>besides the small NBOHC peak at 2 eV

Defect Centers			
Defect Designation	Possible structure	Peak optical absorption energy [eV]	Ref.
$E'$ ( <i>various species</i> )	$\equiv \text{Si}^\bullet$	5.7 – 5.85	[4,8,21–23]
NBOHC	$\equiv \text{Si-O}^\bullet$	1.9, 4.8 <sup>7</sup>	[5,8]
POR	$\equiv \text{Si-O-O}^\bullet$	<i>surface</i> = 5.4, 4.8, 5.1	[22,24,25]
ODC(II)/B <sub>2</sub>	$\equiv \text{Si-Si} \equiv$	$\sim 5.0$	[22] [4,22]

Table 2.1: Common point defects in HPFS, their structures, absorption peaks, and literature references.

## 2.4 Dose

### 2.4.1 Dose Background

Absorbed dose is an SI-derived unit defined as the mean energy imparted,  $d\epsilon$ , by ionizing radiation into a mass,  $dm$ , as in equation 2.17. Integrating equation 2.17 over the entire volume gives the total dose. In this experiment, we define absorbed dose (or dose) as the total energy deposited in a volume divided by the mass of that volume.

$$\text{AbsorbedDose} = \frac{d\epsilon}{dm} \quad (2.17)$$

The movement of energetic particles through space is called “radiation”. When a material has been exposed to radiation, we say that it was “irradiated”. When these energetic particles travel through matter, they cause absorbed dose. There are many types of traveling energetic particles, the one of interest for this experiment and MOLLER is the electron, and the matter it travels through is HPFS. Note that there are other forms of radiation (gammas, neutrons, etc.) that traverse HPFS during MOLLER, and the dose from these other forms is tallied into our target dose levels. However, for this experiment, we achieve the desired dose level in our HPFS samples by irradiating mainly with electrons (and some gammas, but no neutrons).

The mechanisms for dose from energetic electrons coming into contact with any atom are elastic scattering (single and repeated elastic scattering called multiple-scattering, i.e.,

MSC), bremsstrahlung<sup>8</sup>, excitation, and ionization. These are the fundamental interactions from which all other effects stem.

The accelerator in this experiment is tuned to produce 8 MeV electrons. This energy is well suited for our purposes as it is below neutron production threshold, and so does not activate our samples, and has an efficient dose depth profile in HPFS. The dose depth profile measures the percentage of the total dose deposited as a function of the longitudinal distance traveled in the material. Figure 2.13 shows the dose depth profile for several particles at various energies in HPFS. Most of the dose of an 8 MeV electron will deposit in the first centimeter of the HPFS. These dose depth profiles and the dose estimate for this experiment are found using simulation.

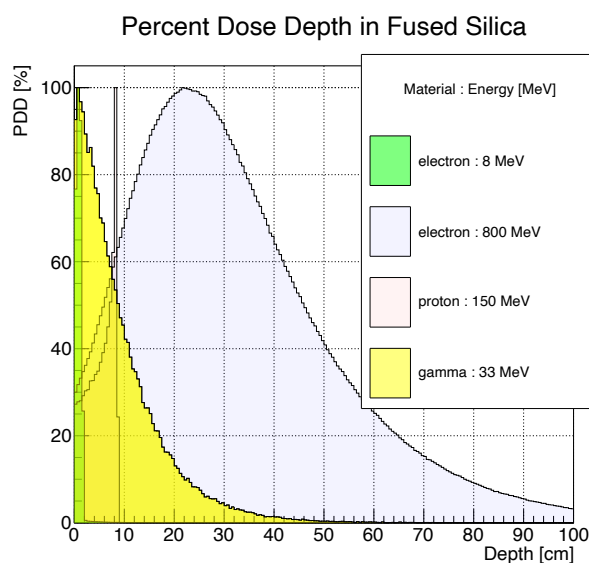


Figure 2.13: This is the dose depth profile in fused silica for various particles and energies. The dose depth curves relate the percentage of total dose deposited as a function of depth along the axis of propagation. You can see an 8 MeV electron (green) will deposit most of its dose in the first centimeter of material, which is the depth of the HPFS samples in this experiment.

---

<sup>8</sup>Bremsstrahlung radiation does not contribute significantly to the dose as it usually exits the material.

## 2.4.2 Geant 4 Simulation

In this experiment, we find the estimated doses in our samples using dosimeters and the simulation software toolkit Geant4 (G4). G4 is a Monte Carlo simulation framework used extensively in nuclear and particle physics. G4 is complete with a vast range of features and functionality, including tracking, geometry, visualization, and physics models<sup>[26]</sup>. Its primary goal is to simulate the passage of particles through matter. Here, we will give a high-level overview of the inner workings of G4 to clarify how our simulation operates.

A run or G4Run is the largest unit of a simulation; every run consists of a sequence of events. A G4Event contains all the information about the primary particle objects and their conversion into G4Track objects. The G4Track objects hold the current information of the particle, such as energy, momentum, and location. This information can be recorded for analysis by assigning a tracking volume.

For example, if 100 electrons are simulated. The simulation generates one electron at a time to send through the simulation environment. Every time an interaction is calculated, a G4Event occurs; if it occurs in the tracking volume, this is called a “hit”. During these hits, particles can do many things, such as create secondary particles and deposit energy. A G4Track object stores all of this information. After the first electron (and any secondaries) has moved through the simulation, the next electron starts. After all 100 electrons and their events have moved through, the G4Run is complete. For more details on G4, how it works, and the physics models used, please see<sup>[26-28]</sup>.

Our G4 simulation “Dose-sim”, is designed primarily to track the amount of energy deposited inside a volume. Dose-sim sets a tracking volume and records every event. The recording happens using two different methods as a sanity check. In one method, a G4Accumulable stores and prints the energy deposited on the screen at the end of the run. The other method records the G4track information in the volume and outputs it to a ROOT file.

It is worth noting that G4 counts energy deposition in two ways, a continuous energy deposition ( $\frac{dE}{dx}$  for the volume) along each step of the simulation and a discrete energy

deposition from specific interactions. Our simulation spreads the energy deposition between pre/post-step points for a more realistic dose profile. This dose spreading prevents the simulation from showing all the continuous energy deposited along a step in one location.

### 2.4.3 Optically Stimulated Luminescence (OSL)

This experiment estimates the dose inside an HPFS sample using a combination of G4 simulation and dosimetric measurements. We use optically stimulated luminescent dosimeters (OSLDs) for the dosimetry. OSLDs have been engineered over the last several decades to have a nearly linear response to ionizing radiation that is easily measured. They are used extensively in medical physics to estimate dose in human tissue. Therefore, we believe OSLDs are ideal for assisting in our dose calculations.

Band theory describes the OSL process in the following way. When ionizing radiation interacts with a crystalline insulator, meta-stable defects are generated, trapping electrons/electron holes ( $e^-/e^{\bullet}$ 's) in-between the conduction and valance bands called a “band-gap”. Optical photons matching the energy of this band-gap can then stimulate the  $e^-/e^{\bullet}$ 's back down to the ground state. This transition causes the emission of characteristic photons, which can then be measured in a photo-multiplier tube.

## 2.5 Light Transmission

In this experiment, the light transmission loss through 1 cm thick samples of irradiated HPFS is measured. However, what does light transmission loss mean? Light transmission is the passage of light particles through matter that are not reflected or absorbed. In this experiment, we measure the intensity of light transmitted through unirradiated (baseline) samples, then we compare this intensity to the light transmitted through the irradiated (dosed) samples. As a function of photon energy, this gives a relative amount of “light lost” ( $T_E$ ) as a percent change. This can be written as

$$T_E = \frac{I_0 - I_d}{I_0 - I_{back}} * 100, \quad (2.18)$$

where  $I_0$  is the baseline sample intensity,  $I_d$  is the dosed sample intensity, and  $I_{back}$  is the background intensity which is treated as a constant (see Section 4.1) and cancels out of the numerator. We also present absorption coefficients ( $\alpha_E$ ) which are found by solving this equation

$$I_d = I_0 * e^{-\alpha_E x}, \quad (2.19)$$

giving

$$\alpha_E = -\ln\left(\frac{I_f}{I_0}\right). \quad (2.20)$$

Where  $I_0$  is the initial intensity incident on the material's surface,  $I_f$  is the light exiting the material, and  $x$  is the distance the light travels through the material. Nevertheless, as in the light transmission loss, we give these as relative measurements compared to baseline, not an absolute absorption; this is an important distinction. So, we are giving a change in absorption coefficients between doses. A derivation is provided to make this clear. Say you have the absolute intensity of light incident on the surface  $I_{abs}$ , compared to the baseline transmitted intensity  $I_0$  this gives  $\alpha_{E,0} = -\ln\left(\frac{I_0}{I_{abs}}\right)$ . Then the next irradiation gives a new intensity  $I_1$  the absolute absorption coefficient would then be  $\alpha_{E,1} = -\ln\left(\frac{I_1}{I_{abs}}\right)$ . Taking the difference between these two gives

$$\begin{aligned}
\alpha_{E,1} - \alpha_{E,0} &= -\ln\left(\frac{I_1}{I_{abs.}}\right) + \ln\left(\frac{I_0}{I_{abs.}}\right) \\
&= \ln\left(\frac{I_{abs.}}{I_1}\right) + \ln\left(\frac{I_0}{I_{abs.}}\right) \\
&= \ln\left(\frac{I_{abs.}}{I_1} \cdot \frac{I_0}{I_{abs.}}\right) \\
&= \ln\left(\frac{I_0}{I_1}\right).
\end{aligned} \tag{2.21}$$

This cuts out a sample's “background” absorption and only looks at the delta of the absorption coefficient from the baseline. This has been featured in peer-reviewed papers; for example, see<sup>[5]</sup>.

The definition of intensity is as follows. Radiant energy ( $Q_e$ ) is the energy of electromagnetic radiation, and radiant flux ( $\Phi_e$ ) is the change in radiant energy with respect to time. Radiance or intensity (I) is the change in radiant flux into a solid angle, which is the term used in this experiment. The ratio of incident to transmitted intensity is called transmittance.

$$\begin{aligned}
\text{Radiant Flux} : \Phi_e &= \frac{\partial Q_e}{\partial t}, \\
\text{Intensity} : I_\Omega &= \frac{\partial^2 \Phi_e}{\partial \Omega \partial A \cos \theta}.
\end{aligned} \tag{2.22}$$

## Chapter 3

# Experimental Setup

The main goal of this experiment is to measure the relative<sup>1</sup> optic transmission loss through five brands of irradiate high purity synthetic fused silica (HPFS). To do this, we irradiated and tested HPFS samples at the Idaho Accelerator Center (IAC) on September 02, 2021, and March 10, 2022. A 25 MeV medical electron linear accelerator (linac) irradiated the samples to the desired dose levels. A light transmission apparatus (LTA) designed and built for this experiment measures the transmission losses. The sample dose is quantified using nanoDot OSLD dosimetry, measurements of the charge per pulse exiting the beampipe window of the linac, and Geant4 simulation.

Before this round of irradiation experiments, previous studies from within the group were used as a starting point. The general principles and some of the LTA equipment (the light source and spectrometer) were kept. However, most of the equipment and procedures used in these irradiations evolved throughout the study. This Chapter will detail the equipment and procedures used, including the Geant4 (G4) simulation.

---

<sup>1</sup>Relative to an unirradiated sample

### 3.1 Equipment and Materials

Most of the equipment involved in the experiment is in the LTA. The LTA consists of a deuterium light source that generates the wavelengths of interest (namely UV and visible), fiber optics, and lenses that focus and transmit the light through the HPFS samples. Moreover, a spectrometer to measure the intensities of light at each wavelength. Figure 3.1 gives a simple schematic of the LTA. By comparing the pre- and post-irradiation spectra, this device measures the relative light transmission loss in the HPFS.

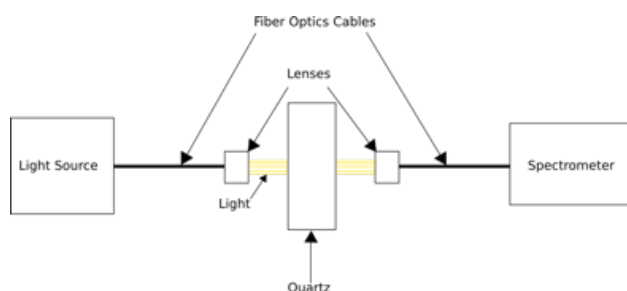


Figure 3.1: A simple schematic (not to scale) of the light transmission apparatus. Light generates in the light source, travels through a fiber optic cable into a collimating lens, then through open-air and through the HPFS sample, through air again and into another collimating lens and fiber optic cable, and finally into the spectrometer where it is measured.

A 25 MeV medical linac irradiates the HPFS samples. At the beampipe exit window of the accelerator, a Pearson<sup>TM</sup> Current Monitor (Pearson coil) measures the current of the electron beam pulses. An oscilloscope reads the current from the Pearson coil. This information is used to calculate the number of electrons that exit the linac during a sample irradiations, which is used in the dose calculations.

NanoDot OSL dosimeters (also called OSLDs) are irradiated in the same position as the HPFS samples. The dose from these, in combination with the charge per pulse data and the G4 simulation, are used to determine the HPFS dose. All of this equipment is described in detail in this Section beginning with the LTA.

### 3.1.1 Light Transmission Apparatus

The LTA consists of a deuterium arc lamp that generates a light beam passed through a fiber optic cable and into a collimating lens. A photograph of the LTA is given in Figure 3.2). The collimated light beam,  $\sim 4.5$  mm in diameter, exits the lens and passes through an HPFS sample (1 cm thick) held in place by a nylon stand and sleeve. The light travels to another collimating lens and fiber optic cable and finally into a spectrometer.

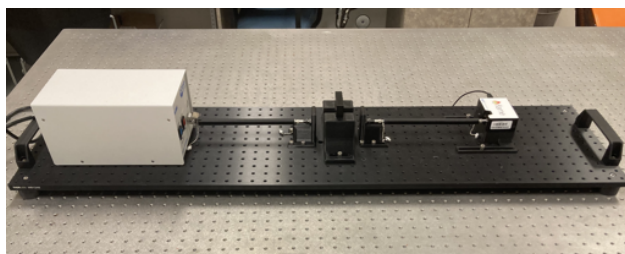


Figure 3.2: The light source is on the left and spectrometer on the right. Samples are located in the center; the entire apparatus is approximately 40 inches long.

### HPFS

Five unique types of HPFS samples made by three different companies are studied in the experiment. The companies and samples are: Corning® HPFS® 7980 homogeneity grade F, Corning® HPFS® 7980 ArF Excimer, O’Hara® SK-1300, Heraeus® Spectrosil-2000® , and Heraeus® Spectrosil-2000® doped with H<sub>2</sub>. All samples are “wet” with an OH content greater than 200 ppm (most 800 – 1000 ppm), except the O’Hara SK-1300, which is “dry” and has an OH content of less than 200 ppm.

Corning makes two samples, HPFS 7980 homogeneity grade 5F and HPFS 7980 ArF Excimer. The 7980 indicates the glass code used by the company to identify different materials they manufacture, and the “homogeneity grade 5F” indicates the piece is certified to have a variation in the index of refraction below  $\pm 5 \times 10^{-6}$ . This grade is equivalent to ISO 10110 part 4 homogeneity class 2 and the SCHOTT homogeneity class H2. The sample has a birefringence rating of  $\leq 5$  nm/cm and a density of 2.20 g/cm<sup>3</sup>. Both Corning samples are

5 cm in diameter, 1 cm thick round cylinders, optically polished on the faces with a rough or unpolished ground surface around the edge.

The Corning HPFS 7980 ArF Excimer is also a 7980 glass type window, but the “ArF Excimer” grade indicates its ability to withstand exposure to an argon fluoride excimer laser ( $\lambda = 193$  nm). This brand aims to have high UV damage resistance. This corning sample has a birefringence rating of  $\leq 1$  nm/cm, and a density of  $2.20$  g/cm<sup>3</sup>.

O’Hara SK-1300 is made by vapor-phase axial deposition (see Section 2.2.1). It has an optical grade quality, grade A, according to MIL-G-174B, which gives a variation of the index of refraction of  $\pm 100 \times 10^{-6}$ , this is the lowest of all the grades tested in this experiment. It has a slightly higher rate of birefringence than the Corning samples at  $\leq 10$  nm/cm and a density of  $2.201$  g/cm<sup>3</sup>. The O’Hara sample is a round cylinder, 5 cm in diameter, optically polished on the faces with a rough surface around the edge.

Heraeus makes two of the samples tested. Heraeus Spectrosil-2000 has a homogeneity grade of 2 according to ISO 10110. Its specification sheet does not give the exact birefringence rating but does indicate that it is very low, especially towards the center of the piece. It has a density of  $2.20$  g/cm<sup>3</sup>. The H<sub>2</sub> doped sample is made from the same material but has a higher concentration of H<sub>2</sub>. Both sample types are 1 cm thick,  $5 \times 5$  cm<sup>2</sup> with optically polished faces and rough surfaces around the edges.

## Light Source

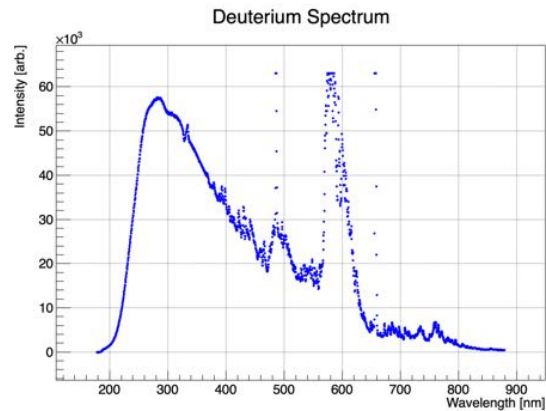
The light source is a 25 Watt DH-2000 Deuterium-Halogen Light Source made by Ocean Optics see Figure 3.3a for a photograph. This type of lamp is known as a deuterium arc lamp. The lamp consists of a cathode and anode in an enclosure filled with molecular deuterium gas (D<sub>2</sub>). An arc is created between the cathode and anode, which excites the gas molecules and produces a continuous spectrum in the UV through visible region (UV-Vis).

This light source is rated to emit wavelengths between  $\sim 190 - 900$  nm. Figure 3.3b shows spectra of our lamp with the characteristic hydrogen Balmer lines, sharp peaks at 486

nm and 656 nm, and Fulcher band emission between 560 to 640 nm. A sharp drop-off in intensity close to 200 nm results from the loss of sensitivity/efficiency of our LTA components to transmit and measure these small wavelengths. In actuality, the spectrum does not drop off until wavelengths close to 160 nm.



(a) Photograph of the Deuterium light source



(b) Deuterium Spectrum

Figure 3.3: The intensity units are arbitrary and only make sense relative to one another. The hydrogen Balmer lines with sharp peaks at 486 nm and 656 nm, and Fulcher band emission between 560 to 640 nm are clearly visible. Note the Balmer lines and tip of the Fulcher band intensities are saturated.

The lamp needs to reach thermal equilibrium for the best intensity stability. It is turned on at least 45 minutes before the first measurements; this is done every time. After the warm-up period, the manufacturer claims it has an intensity stability of 0.01%/hr and a drift value of 0.01%/hr at 254 nm. Our LTA measured a higher rate of intensity fluctuation (although still minimal), at  $\sim 0.1\%$ /hr, likely due to the combined effect of all the LTA's optical components and our measurement technique.

## Spectrometer

The spectrometer in this experiment is the Flame-S-UV-VIS-ES miniature spectrometer made by Ocean Optics (see fig. 3.4). This spectrometer measures wavelengths between 200 – 900 nm, making it well suited to the light source. The -S stands for Sony, the charge-coupled device (CCD) brand, -UV-VIS stands for the ultra-violet and visible wavelength

range it is optimized to detect, and -ES stands for enhanced sensitivity using an additional lens just before the CCD as discussed below.

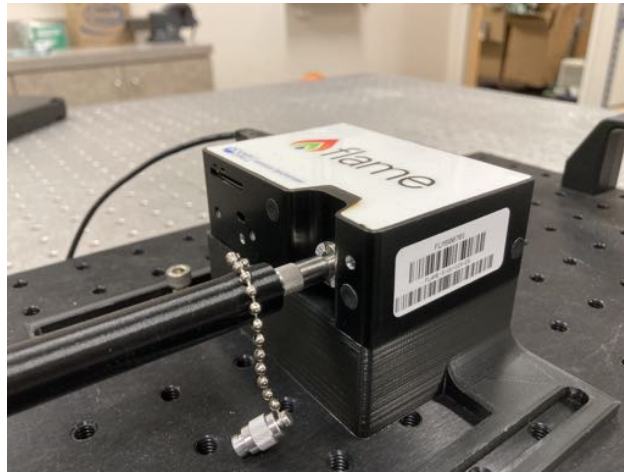
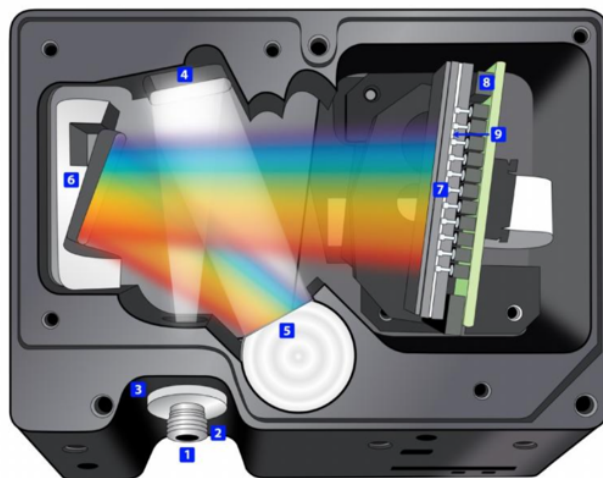


Figure 3.4: The spectrometer connects to a fiber optic cable receiving the transmission signal. It sits in it's own 3D-printed stand that bolts to the optical table.

The spectrometer first receives light through an SMA 905 fiber optic connector with a 25  $\mu\text{m}$  slit that acts as an entrance aperture (1),(2), and (3) in Figure 3.5. The light travels to a collimating mirror (4), reflecting as a collimated beam unto a diffraction grating (5). This grating is tuned at the factory and fixed permanently to avoid any system shifting. The light is then incident on a focusing mirror (6) which focuses diffraction peaks onto the detector collection lens (7). The collection lens focuses light onto the (CCD) detector elements (this is the -ES enhanced sensitivity). Finally, the CCD is a Sony ILX511B with a fixed pixel well depth of  $\approx 62,500$  photons for each photo-detector (or pixel), giving it a signal-to-noise ratio (S:N) of 250:1<sup>[29]</sup>. The Flame spectrometer also comes with factory control and data acquisition PC software which we use.

Our spectrometer's grating type and slit size give it a spectral range of  $\approx 693$  nm starting at 178 nm, with an optical resolution of 1.4 nm. However, the CCD digitizes the signal with an 11-bit ADC, providing a data binning resolution of  $\sim 0.3$  nm. Figure 3.6 shows the relative detection efficiency for each wavelength. Our spectrometer uses grating #1 with peak efficiency at approximately 375 nm and a best use range ( $> 25\%$  efficiency) of



**Flame Open Bench**

Figure 3.5: A diagram of the inner workings of the spectrometer<sup>[29]</sup>. The light travels to a collimating mirror (4), reflecting to a diffraction grating (5), then to a focusing mirror (6) and into a collection lens (7), and finally onto the CCD.

approximately 200 – 775 nm.

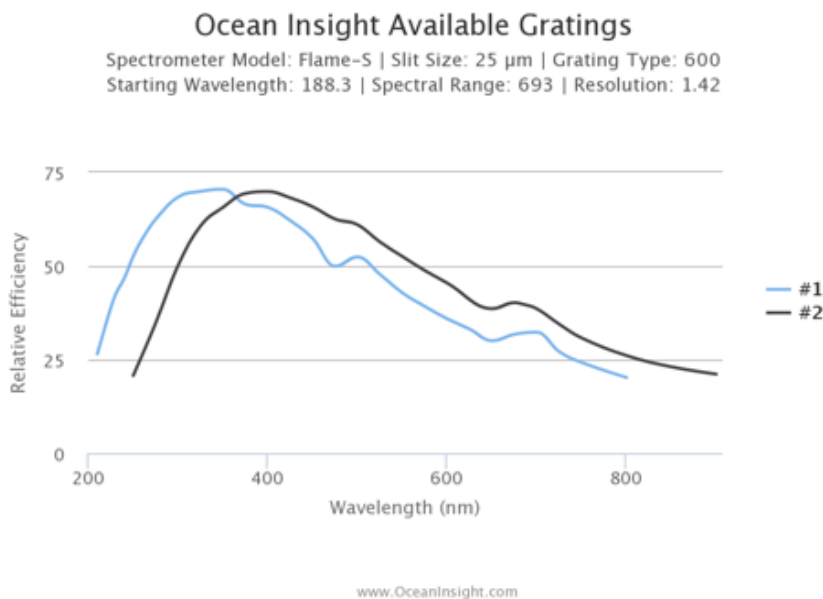


Figure 3.6: Spectrometer Wavelength Efficiency Chart from the factory.

## Fiber Optics and Lenses

The fiber optic cables used in the apparatus are model QP450-0.25-XSR made by Ocean Optics. Figure 3.7 displays a picture of the cables. QP450 indicates the fiber core diameter of  $450\ \mu\text{m}$ , 0.25 is the length of the fiber in meters, and XSR stands for solarization<sup>2</sup> resistant, which means that this fiber is made with aluminum and polyimide buffers to reduce the degradation from UV radiation. The fibers are encased in a stainless steel type BX jacket designed for added resilience and durability.

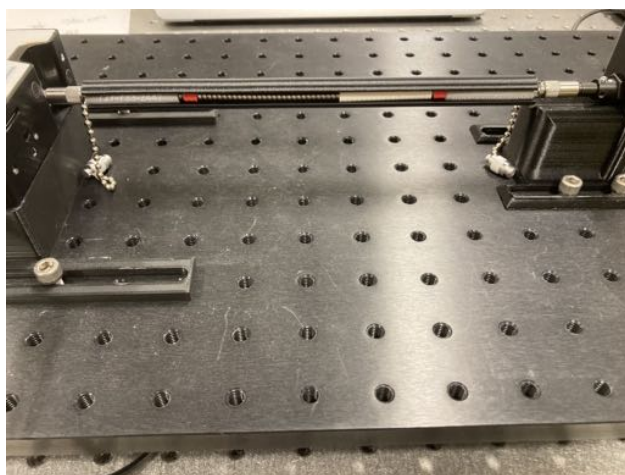


Figure 3.7: The jacketed fiber optic cable inside of its 3D-printed nylon sleeve.

The fibers slide into a long cylindrical sleeve custom-made from 3D-printed nylon. This sleeve protects the fibers from being touched, shifted, or changing position during the running of the experiment.

The lenses collimate the light coming from the first fiber optic cable and again after the light has passed through the HPFS before entering the second fiber optic cable on its way to the spectrometer. They are model 74-UV collimating lenses made by Ocean Optics. Figures 3.8a and 3.8b show their picture. The optical lens is made from type f/2 fused silica Dynasil and is made to pass wavelengths between  $180\text{nm} - 2.5\mu\text{m}$ . The lenses thread onto custom 3D printed nylon mounts to keep them in place during the experiment. The nylon mounts are shown in Figure 3.8c.

---

<sup>2</sup>Solarization means increased absorption in the UV region.

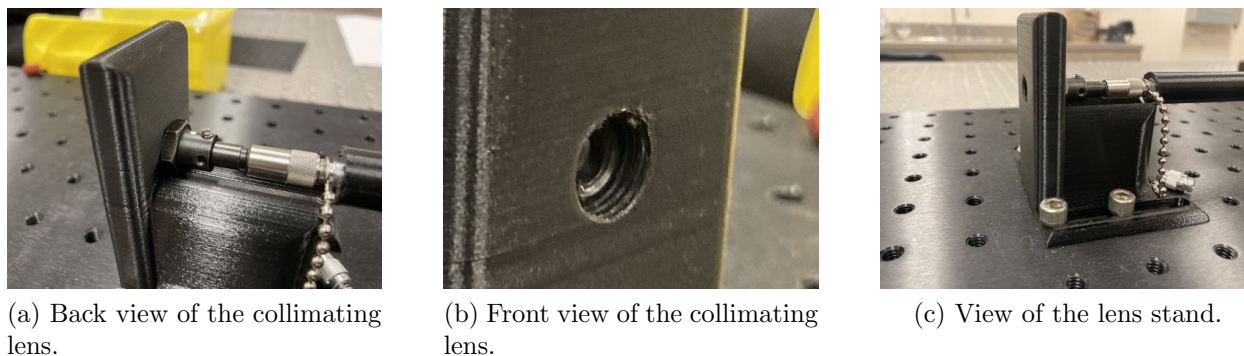


Figure 3.8: Photos of a collimating lens mounted in its stand. The lens threads into the 3D-printed support stand.

### HPFS Sample Stands and Sleeves

In the middle of the apparatus is a 3D-printed nylon HPFS mounting block, as shown in Figure 3.9a. The stand mounts to the optical table, and a nylon HPFS sleeve inserts inside. The sleeve and mount constrain the HPFS sample in all degrees of freedom which allows for repeatable measurements through the same location on each HPFS piece. Figure 3.9b shows a sleeve inserted into the mount.

Figures 3.9c and 3.9d are pictures of the HPFS sleeve which hold the HPFS samples. These sleeves transport easily from the light apparatus to the beamline, where the samples are irradiated inside the beamline HPFS stand. Figure 3.10 displays the beamline HPFS stand, which bolts to an optical table and scissor jack. The beamline stand serves the same purpose as the sample holder, allowing irradiation in the same location on each HPFS piece each time they are dosed.

The 3D-prints are made from black nylon, known to be relatively radiation-hard<sup>[30]</sup>, resistant to UV light, and will not easily scratch polished HPFS. So, the nylon prints can withstand the radiation from the beam and the intense UV light from Cherenkov radiation and will not scratch the polished HPFS.



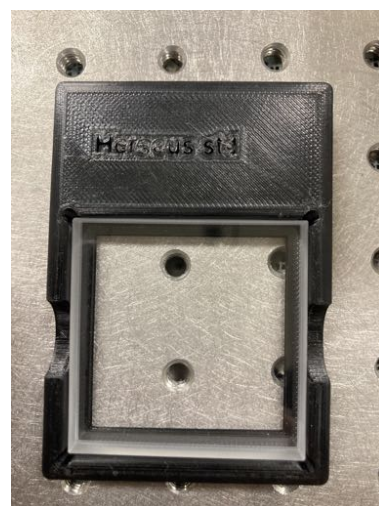
(a) HPFS Stand



(b) Sleeve inserted into the stand



(c) Round sample sleeve



(d) Square sample sleeve

Figure 3.9: We have designed various stands and sleeves throughout this experiment. These are the final designs used in these irradiations.

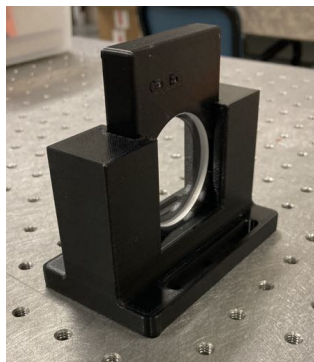


Figure 3.10: The beamline HPFS stand with a round sleeve inserted.

### 3.1.2 Linear Accelerator

#### Accelerator

A 25 MeV, S-band linear electron accelerator at the IAC irradiates the HPFS samples. The linac uses an electron source and radio-frequency acceleration from an applied ac voltage. The electrons accelerate as they cross the gaps between hollow tube electrodes (drift tubes). As the electrons enter the drift tubes, they drift in a field-free region for a time equal to half the period of the ac voltage. The polarity of the voltage is reversed while the particle is in the drift tube; the electrons then accelerate as they cross the next gap<sup>[31]</sup>. Figure 3.11 gives a simple diagram of this process.

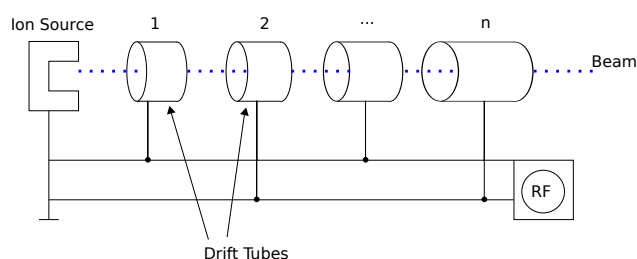


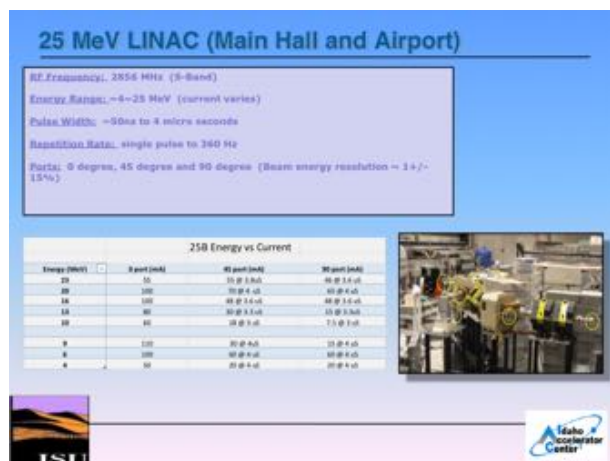
Figure 3.11: This is an example of how a linear accelerator works. These particles accelerate due to an applied ac voltage as they cross the gaps between RF drift tubes. They drift the field-free region of the tubes for a time equal to half the period of the ac voltage.

The accelerator operates at 8 MeV peak energy,  $\sim 40$  mA peak current, and with 1000 ns pulse width at a 200 Hz repetition rate. These settings provide approximately 35 – 40 nanoCoulombs (nC) of beam charge per pulse. Figure 3.12b shows some advertised

specifications for the accelerator. The beam has two exit ports, a  $0^\circ$  port which is used during all irradiation and dosimetry runs, and a  $45^\circ$  port used only for the beam energy scan. Both ports are shown in Figure 3.13.



(a) 25 MeV Linac at the IAC

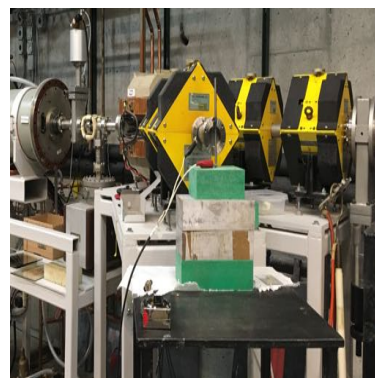


(b) Specifications for the IAC 25 MeV electron Linac

Figure 3.12: The 25 MeV accelerator at the IAC with some advertising specifications.



(a) Pearson coil in front of the  $0^\circ$  beam pipe window



(b)  $45^\circ$  port with the tungsten rod

Figure 3.13: The  $45^\circ$  and  $0^\circ$  ports of the linear accelerator. The  $0^\circ$  port is used for all light transmission measurements. The  $45^\circ$  is used for the energy scans covered in Section 3.2.1.

## Oscilloscope and Pearson Coil

A Tektronix model TDS 3044B four channel color digital phosphor oscilloscope (see Figure 3.14b) reads the information obtained from a Pearson™ wide band current monitor made by Pearson Electronics inc. Figure 3.14 shows photographs of both items. The Pearson coil is set just outside the beam pipe window as in Figure 3.13a.



(a) Pearson coil



(b) Oscilloscope

Figure 3.14: Equipment used to measure the charge of the electron beam exiting the beampipe window.

### 3.1.3 Dosimetry Materials

#### nanoDot™ OSL Dosimeters

Inlight® nanoDot™ OSL dosimeters (referred to as OSLDs) quantify the dose to the HPFS samples. They are designed for single-point radiation assessment applications, such as medical imaging and radiation oncology. We use them in this study to estimate a dose in inorganic fused silica. However, their OSL properties (see Section 2.4.3) make them ideal for our dosimetric application.

The nanoDot OSLDs are made of carbon-doped aluminum oxide encased in a polyester binding material layered between a thin polyester substrate and a polyester film. The active

part of the nanoDots are disc-shaped wafers 0.50 cm in diameter and effectively  $\sim 0.02$  cm thick<sup>[32]</sup>. The disc is enclosed in an ABS plastic light tight shell to shield the OSLD disk from optical light exposure to avoid discharge. Figure 3.16 is an exploded diagram of the nanoDot and Figure 3.15 is an image.

The nanoDots are screened at the manufacturer to have less than 5.5 % variation in dose-response. They are also given a sensitivity correction to adjust the PMT counts measured from the individual OSLDs. This correction is automatically accounted for when measured using their proprietary reader, the microStar<sup>®</sup> as we do in this experiment.



Figure 3.15: Image of a nanoDot used in the dosimetry measurements. Notice the top row alpha numeric sequence; the DN091 stands for a sensitivity correction of 0.91

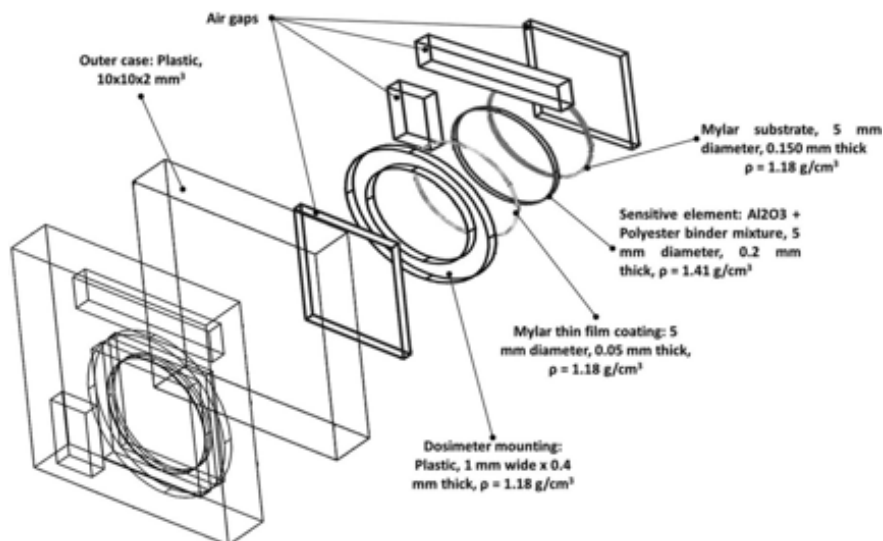
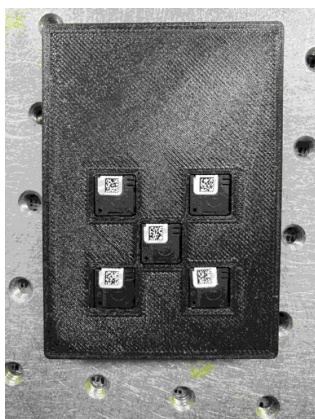


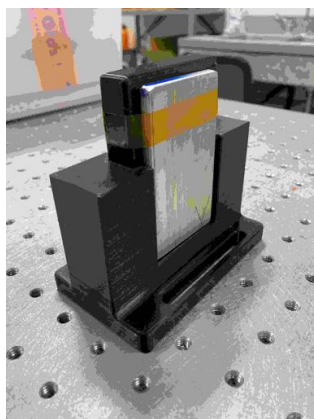
Figure 3.16: Exploded diagram of nanoDot<sup>[32]</sup>. Note in Figure that the density used in their paper was an attempt to account for the polyester binding material. We found that using this low density leads to inaccurate dose estimations. We simply make an active material out of carbon doped aluminum oxide in our G4 simulation.

## Beamline nanoDot equipment

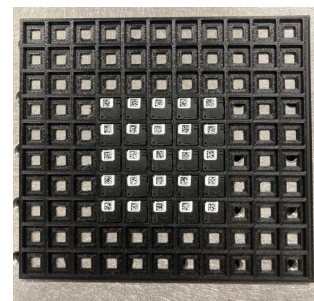
The nanoDots are placed into a 3D printed nylon grid and a five point nylon sleeve (see Figure 3.17). This is for consistent and repeatable OSL placement. We irradiate the arrays with a 3/16 inch thick aluminium plate placed in front.



(a) Five point nanoDot Sleeve.



(b) Sleeve inserted in the beamline stand with aluminium.



(c) OSLDs inserted in the nylon grid.

Figure 3.17: The nanoDot beamline equipment. In (a) the center OSLD is in the exact same location as the  $5 \times 5 \times 10 \text{ mm}^3$  section of HPFS that is measured through in the light transmission measurements.

## 3.2 Methods

This Section contains measurement and calculation procedures for the light transmission loss, dosimetry, sample dose, and beamline setup. The so-called “beamdays” (ten hour periods), in which all reported measurements are taken, took place at the IAC on September 02, 2021, and March 10, 2022. Some procedures detailed here were not yet fully developed by the September beamday. For example, the beamline procedure did not involve the same equipment, and there was no laser alignment. Despite this exception, most measurements were taken in the same ways. And all data analysis is done with the ROOT data analysis framework.

A few measurements were taken using slight variations in the light transmission techniques, different beam settings, or different analysis techniques. They are not detailed here; instead, they are described in Chapter 4 with their accompanying results.

### 3.2.1 Beamline Setup

We implement a standard setup procedure for consistent measurements during every beam-day. This procedure involves these steps: we use consistent beam parameter settings set by the IAC technicians; characterize the beam by quantifying beam properties such as the energy distribution and charge of the pulses; align the HPFS samples to the beam center, and take dosimetric measurements.

#### Beam Parameters

We use the operation parameters of 8 MeV peak energy,  $\sim 40$  mA peak current, and 1000 ns pulse width at a 200 Hz repetition rate for the nominal beam setup. This provides approximately 35 – 40 nC of beam charge per pulse. These settings also keep the dose rate low enough to keep the HPFS sample temperature under  $\sim 40$  °C. Temperatures higher than 100 °C will be shown in Section 4.4 to anneal some defect centers, and thus distort our transmission loss measurements.

#### Beam Characterization

After the nominal beam setup, we measure the beam energy distribution. The technique uses a calibrated dipole magnet and a thin tungsten rod placed at the center of the 45° port beampipe exit window; a photograph of the setup is shown in Figure 3.18. The dipole magnet sweeps through various “set points” which steer known beam energies into the tungsten rod. The beam generates a current on the tungsten rod, which is measured at each dipole set point giving the beam’s energy distribution. Our G4 simulation uses this distribution in the simulated beam. Other beam characterizations are described in appendix C.



Figure 3.18: The 45°Port. A tungsten rod (oriented vertically) located at beamport exit window measures the current for the beam energy scan.

### Beam Alignment

A laser aligning procedure ensures the HPFS sample placement at the beam's center. First, a glass slide is irradiated at the beam pipe window. The center of the beam distribution is marked and checked using a photocopier and ImageJ software. Another glass slide  $\sim 50$  cm downstream of the beampipe window is irradiated, marked, and checked. An alignment laser is then adjusted to pass through the center marks in both glass slides, assuring accurate alignment of the laser to the center of the beam. Figure 3.19 shows an illustration of this alignment.

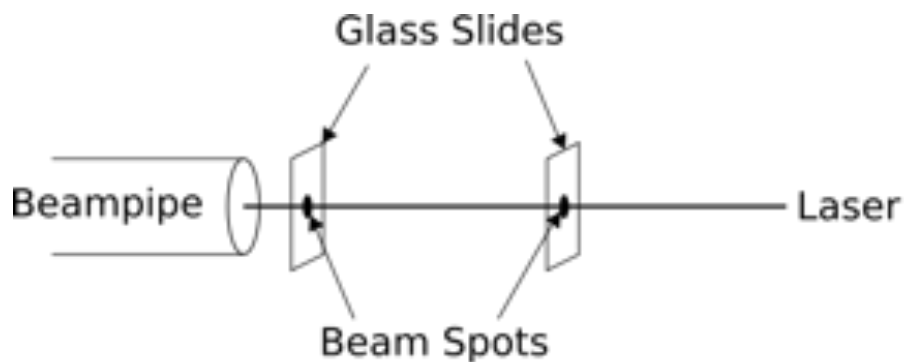


Figure 3.19: A simplified diagram showing how the laser is adjusted until it passes through the center of the beam spots on two glass slides  $\sim 50$  cm apart.

The beamline HPFS stand is bolted to an optical scissor jack, for vertical positioning, and aligned to place the center of HPFS samples directly in the path of the alignment laser

50 cm from the beampipe window. When the HPFS sample is placed in the stand, the laser beam reflects back to the laser source within 2 – 4 cm of the origin<sup>3</sup>. This process aligns the  $5 \times 5 \times 10 \text{ mm}^3$  center section of the HPFS to the center of the beam distribution.

### 3.2.2 Light Transmission Loss Procedure

The LTA measures the relative light transmission loss through the irradiated HPFS samples. This section outlines the procedure for the light transmission measurement.

First, the light source is turned on and allowed to warm up for at least 45 minutes. After the warm-up period, “open air” (no sample) and background (no sample or light) measurements are taken. These measurements are taken throughout the beamday between irradiations; they track systematic changes in the LTA, specifically any change in the lens/fiber optics positions, light source intensity drift, or ambient light fluctuations.

After the first open air and background measurements, we put the HPFS samples into their sleeves (each sample has a custom printed sleeve) and take several pre-irradiation measurements. First, the sleeve is inserted into the stand; a spectrum measurement is saved, then the sleeve is taken out of the stand. The process is typically repeated  $\sim 10$  times for each sample. The spectrometer integrates the signal for 1 ms (called a scan) and averages 1000 of those scans together to make one measurement. These first measurements provide the “baseline” that all proceeding (post-irradiation) measurements are compared to.

Following the baseline measurements, the HPFS sample is put into the beamline stand; where the distance from the beampipe exit window to the upstream face of the HPFS sample is  $\sim 50$  cm. Two vortex-producing, compressed air nozzles blow cold air directly on the samples to keep the HPFS below 40 °C. The samples are then hit with 16k, 32k, 64k, 112k, and 240k beam pulses in five successive exposure runs. In between each run, three light transmission measurements are taken at around 15 seconds per measurement. The time exposed to the deuterium source is kept as short as possible to minimize the amount of

---

<sup>3</sup>At  $\sim 8$  m round trip that puts an approximate angular deflection of  $\lesssim 0.5$  degree

annealing from UV bleaching.

### 3.2.3 Dose Calculation

The G4 simulation allows us to convert a dose from a nanoDot OSLD to the  $5 \times 5 \times 10$  mm<sup>3</sup> center section of an HPFS sample. The various components (procedures, measurements, calculations and simulations) used to determine the sample dose are described in this subsection.

#### Dosimetric Measurements

The five-point OSL array sleeve shown in Figure 3.17a is designed to fit into the beamline stand and has an overall geometry identical to the HPFS sample sleeves. This allows consistent alignment of the center of the OSL array with the center of the beam, and thus the center of the HPFS sample. A 3/16 inch thick aluminum plate is mounted just upstream of the OSL array. Using the aluminum plate reduces fluctuations in the OSLD measurements; this feature is also implemented in the simulation. The OSLD arrays are irradiated for only 3 – 5 pulses to keep doses below 20 Gy. Again, the central OSLD in the array is in the same location as the center  $5 \times 5 \times 10$  mm<sup>3</sup> section of the HPFS samples, which is where we perform the light transmission measurements.

The microStar reader measures the OSLDs after “resting” for 10 minutes post-irradiation. This allows for dose stabilization in the OSLDs. The reader measures PMT counts, which are then fed into a second-order polynomial calibration curve<sup>4</sup>, to obtain a dose. This dose is normalized to the acquired charge in the beam pulses and is used by our G4 simulation to determine the dose in our HPFS samples.

---

<sup>4</sup>This curve is from a cesium-137 calibration which is covered in Appendix B

## Charge Data Collection

We record the charge from each beam pulse of the dosimetry measurements individually. The charge for the HPFS irradiations, which consists of hundreds of thousands of pulses, is sampled every 60 seconds using the software at the IAC designed for these measurements. The software saves all the beam pulse charge measurements to an output file that is used in the analysis.

### 3.2.4 G4 Simulation

The G4 simulation called “Dose-sim” simulates the dose in the  $5 \times 5 \times 10 \text{ mm}^3$  center section of an HPFS sample. The simulation determines a constant ratio, or conversion factor,  $A$ , between the normalized dose on the center OSLD crystal to the normalized dose in the center of the HPFS sample. This can be expressed simply as

$$\frac{Dose_{5x5HPFS}}{\text{nC}} = A * \frac{Dose_{OSL}}{\text{nC}}, \quad (3.1)$$

where the conversion factor  $A$  is a constant determined by varying the simulated beam parameters and studying the simulated dose-response in an OSL crystal and an HPFS sample. Hundreds of individual simulations are combined to determine the dose conversion factor. For more details on previously attempted strategies to calculate dose see appendix C.

### Matching the Environment and Materials

At the top level of the simulation environment is a “world” volume made of vacuum. Inside the world is a volume made of a customized air which contains a titanium volume for the beampipe window and a tracking volume made of either HPFS or an OSLD array.

The custom air is made from the G4 materials database with the pressure set to 0.85 atm and a temperature of 20° C, approximating what the air is like in Pocatello, Idaho<sup>5</sup>.

---

<sup>5</sup>This does not affect the dose-response, but is a carryover from previous dose calculation strategies.

The titanium plate is one mil thick to replicate the beam pipe window that the electrons pass through, exiting the accelerator.

The HPFS material is one part silicon, and two parts oxygen, with a density set to 2.20 g/cm<sup>3</sup><sup>[33,34]</sup>. The OSL material is 99.988 % aluminum oxide and 0.012 % carbon-12 with a density set to 3.9698 g/cm<sup>3</sup><sup>[35]</sup>. Layers of aluminum and ABS plastic are added in front of the OSL array to simulate the aluminum plate and the plastic from the nanoDot case. Figure 3.20 shows a visualization of these volumes and 1000 electron events.

### Simulated Electron Beam

We initially sought to fully characterize the real-world particle beam by matching the energy distribution and beam divergence found in the beam characterization measurements in appendix C. Through the experiment, we found this to be an unnecessary process. The dose-response ratio from OSLD to HPFS is constant no matter the beam parameters used. This is shown in Section 4.2.1. The beam energy distribution is the only measurement still used. The simulation parameters are as follows.

624220 electrons ( $10^{-3}$  nC) at 8 MeV  $\pm$ 0.6 MeV are simulated incident on an OSLD array or HPFS sample. Angular and radial sigmas of the generated beam are simulated over a large phase space of values ranging from 0 degrees to 3 degrees angular sigma and 0 cm to 3 cm radial sigma. The dose-response is then stored and used for analysis; results are shown in Section 4.2.1.

To summarize, the dose in the HPFS is found by irradiating OSLDs in the same spot as the HPFS samples. The OSLDs are measured in the microStar reader, which gives PMT counts that are put into a calibration curve to obtain a dose. This dose is normalized to the charge in the beam pulses, yielding a dose/nC for the OSLDs. The simulated conversion factor converts this to a dose/nC for HPFS, which is scaled by the total charge for each run.

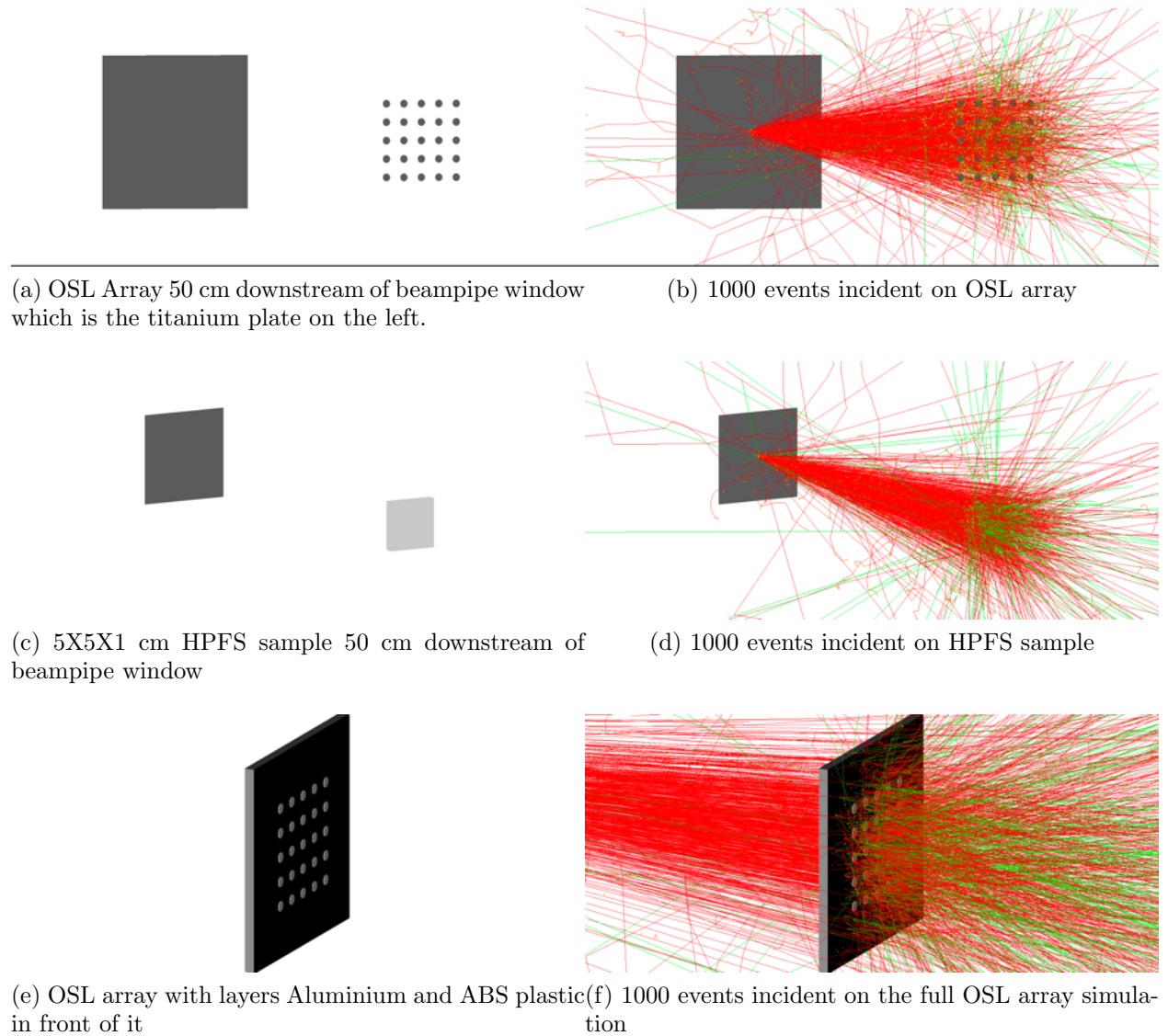


Figure 3.20: Images of the simulated environment of Dose-sim. This exhibits several materials 50 cm down stream from the titanium plate which sits just outside of the air volume inside of the world vacuum. In (f) is an example of what the simulated beam looks like incident on a target.

# Chapter 4

## Results and Discussion

### 4.1 Light Transmission

The light transmission losses for 10 HPFS samples (2 of each type) were taken on two separate beamdays, September 02, 2021, and March 10, 2022. The sources of error for the measurements are discussed in Section 4.1.1, the analysis and results are shown in Section 4.1.2. Error propagation calculations are described and discussed in appendix A.

#### 4.1.1 Sources of Error

There are several sources of systematic error in the transmission measurements. The most significant contributions come from inserting the HPFS piece into the light transmission apparatus (LTA), which can cause rotational or translational changes in the HPFS position. Rotation changes the orientation of the face of the sample causing changes in reflection and refraction. Translation changes the volume that the light passes through; this is important for reasons stated in Section 4.2. Other sources include shifting of the optical components, light source intensity fluctuation, annealing/damaging effects from UV light exposure, and temperature changes.

Most of these sources are accounted for in the repeated measurements or are eliminated

by the LTA design. The only exceptions are the optical component shifting and light source intensity fluctuation. However, those sources are tracked by taking measurements throughout the day with no samples in the LTA (referred to as open-air and background measurements). By comparing these measurements to each other, we can see if any changes have occurred. Figure 4.1 graphs the relative standard deviation of open-air measurement intensities from 200 – 800 nm. This data covers 8 measurements over approximately one hour, the average time to dose one sample completely. These are typical results and show that the LTA intensity measurements vary by less than 0.1% over a one hour period.

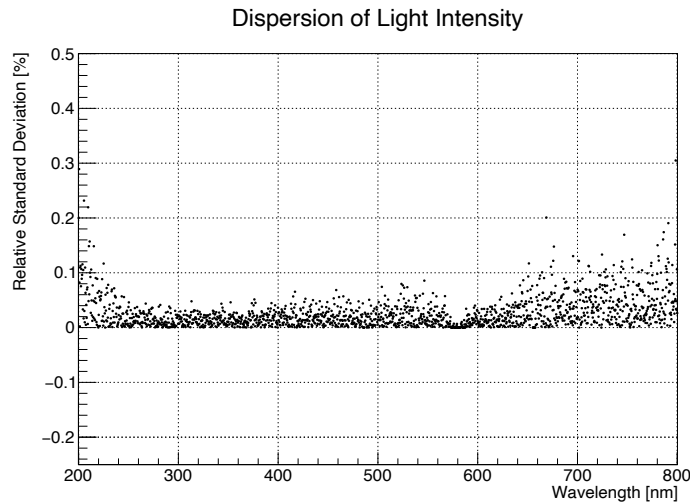


Figure 4.1: This plot gives the relative standard deviation or percent variation in intensity by wavelength for 8 “open air” measurements taken throughout the Corning UV 7980 Homogeneity grade 5F irradiations ( $\sim 1$  hour). This shows a variation of less than 0.1%.

### 4.1.2 Results

The light transmission loss is calculated as a percentage of the original intensity at each photon energy<sup>1</sup>, given by

$$T_l = \frac{I_0 - I_d}{I_0 - I_{back}} * 100, \quad (4.1)$$

---

<sup>1</sup>Measured in wavelength and converted here to energy to fall in line with the prevailing literature

where  $I_0$ ,  $I_d$ , and  $I_{back}$  are the unirradiated, irradiated, and background intensity, respectively. The background intensities are measured with the light source blocked; this is the signal noise of the LTA. Figure 4.2 displays the RMS of the background intensity throughout a beamday. The background fluctuates by minimal amounts, less than two intensity counts, which is treated as a constant and cancels out of the numerator.

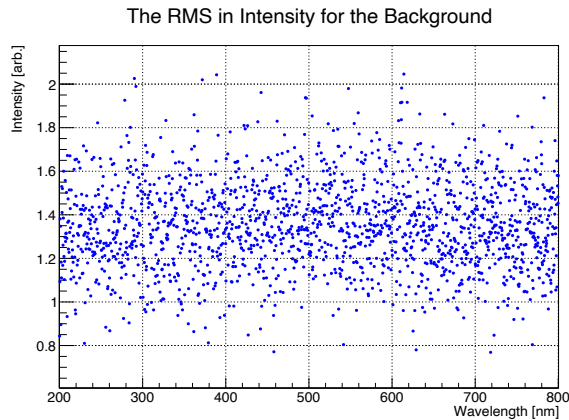


Figure 4.2: Plot of the RMS of the background measurements taken throughout an entire beamday, which is less than 2 intensity counts for any given energy and is treated as a constant ( $I_{back}$ ).

$T_l$  is graphed for each photon energy, at each dose, for each sample, in Figures 4.3 and 4.6. The absorption coefficients are also given in Figures 4.4 and 4.7. The absorption at each dose for each photon energy is calculated by  $\alpha_{d,E} = \ln\left(\frac{I_0 - I_{back}}{I_d - I_{back}}\right)$ . In Figures 4.8 and 4.5 the transmission losses are given in wavelength. Using the error propagation found in appendix A the average error for any given wavelength or energy is  $\lesssim 0.5\%$ .

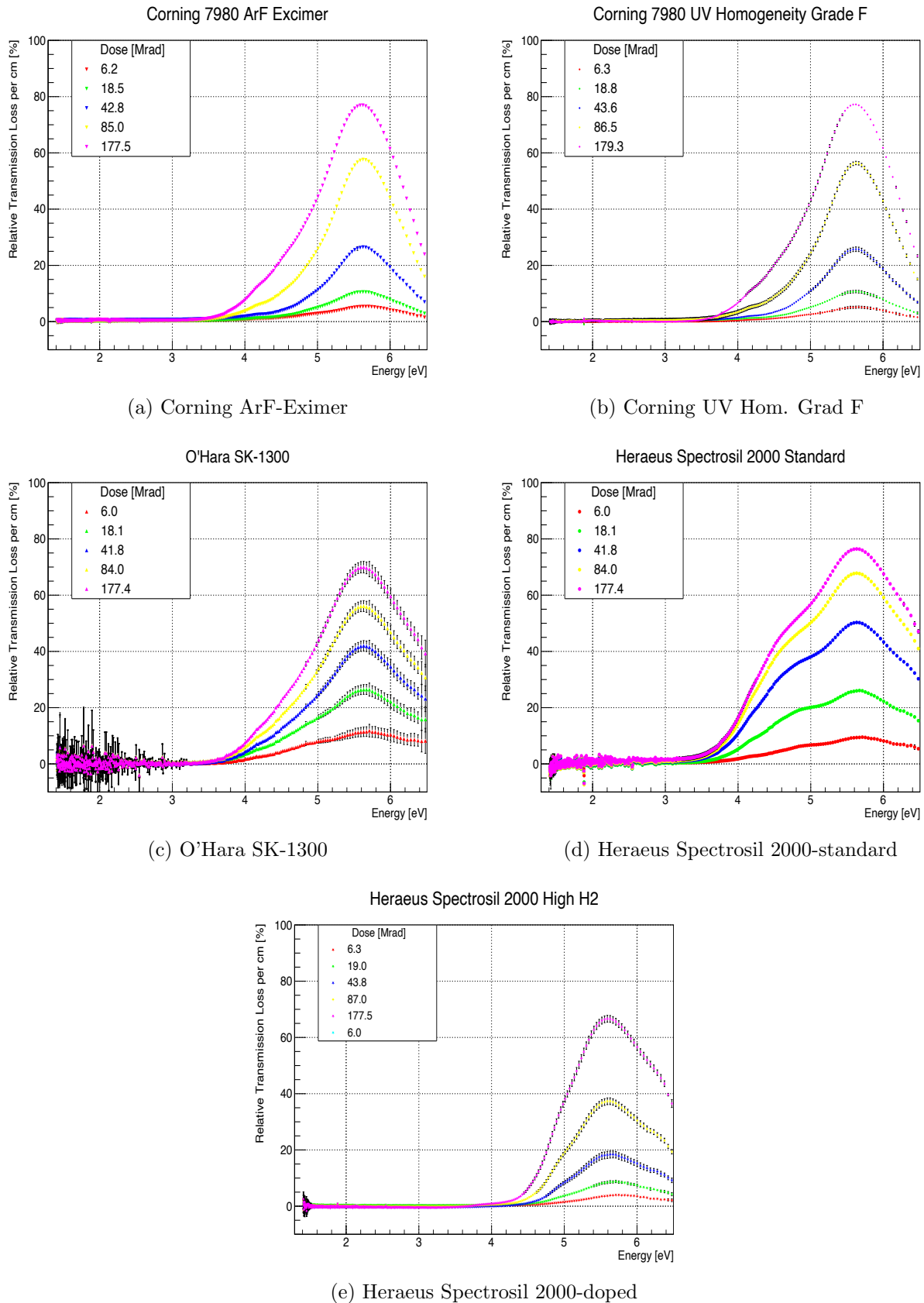
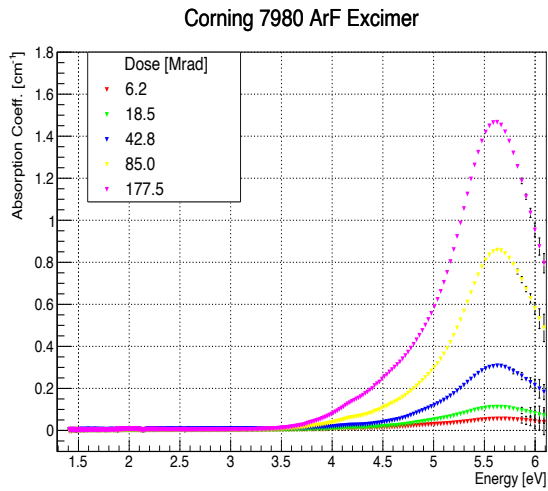
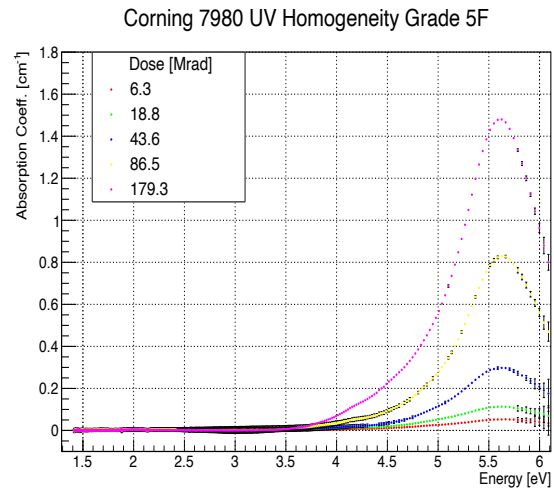


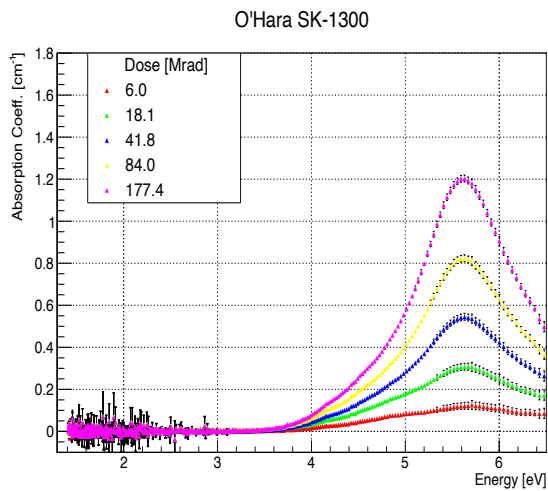
Figure 4.3: The September 2<sup>nd</sup> relative light transmission losses for each sample at each dose with  $\delta_{T_l}$  error bars.



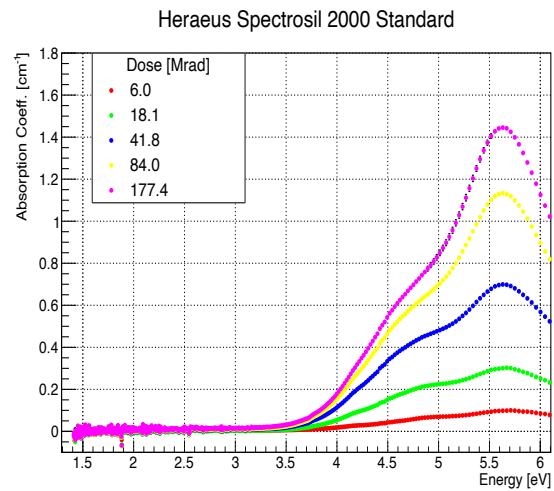
(a) Corning ArF-Eximer



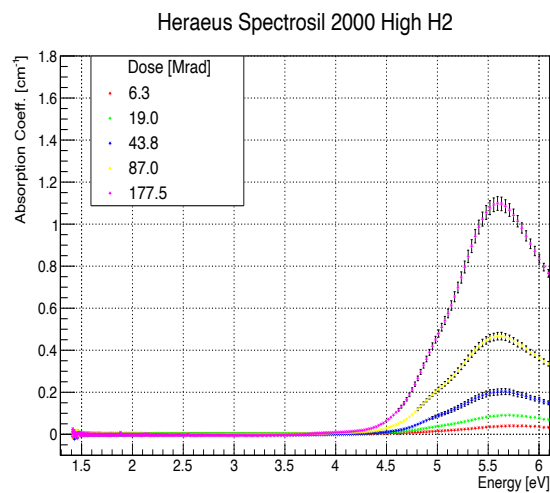
(b) Corning UV Hom. Grad F



(c) O'Hara SK-1300



(d) Heraeus Spectrosil 2000-standard.

(e) Heraeus Spectrosil 2000-doped H<sub>2</sub>Figure 4.4: The Sept. 2<sup>nd</sup> absorption coeff. for each sample at each dose with  $\delta_{T_1}$  error bars.

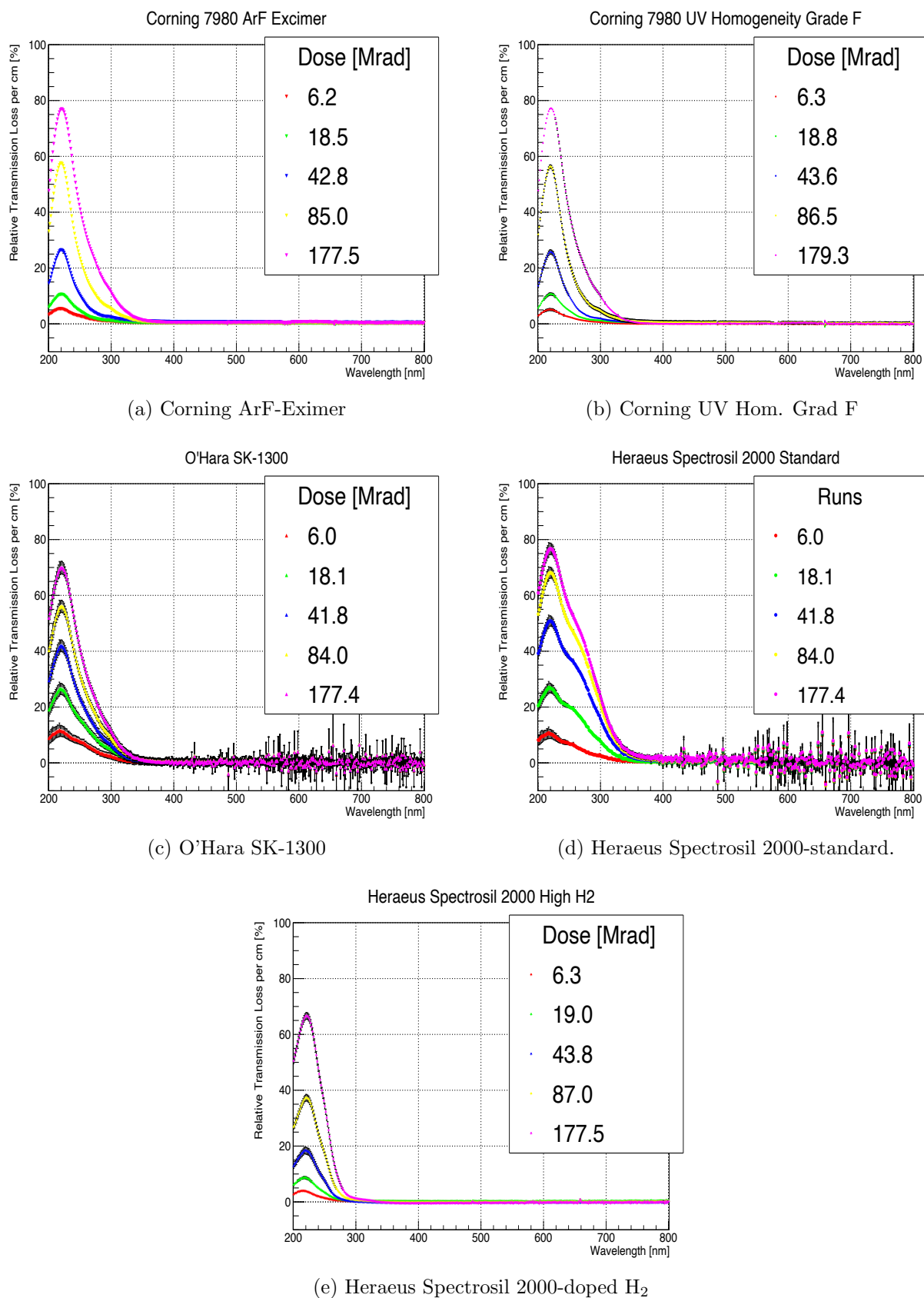


Figure 4.5: The Sept. 2<sup>nd</sup> relative light transmission losses versus wavelength for each sample at each dose with  $\delta_{T_l}$  error bars.

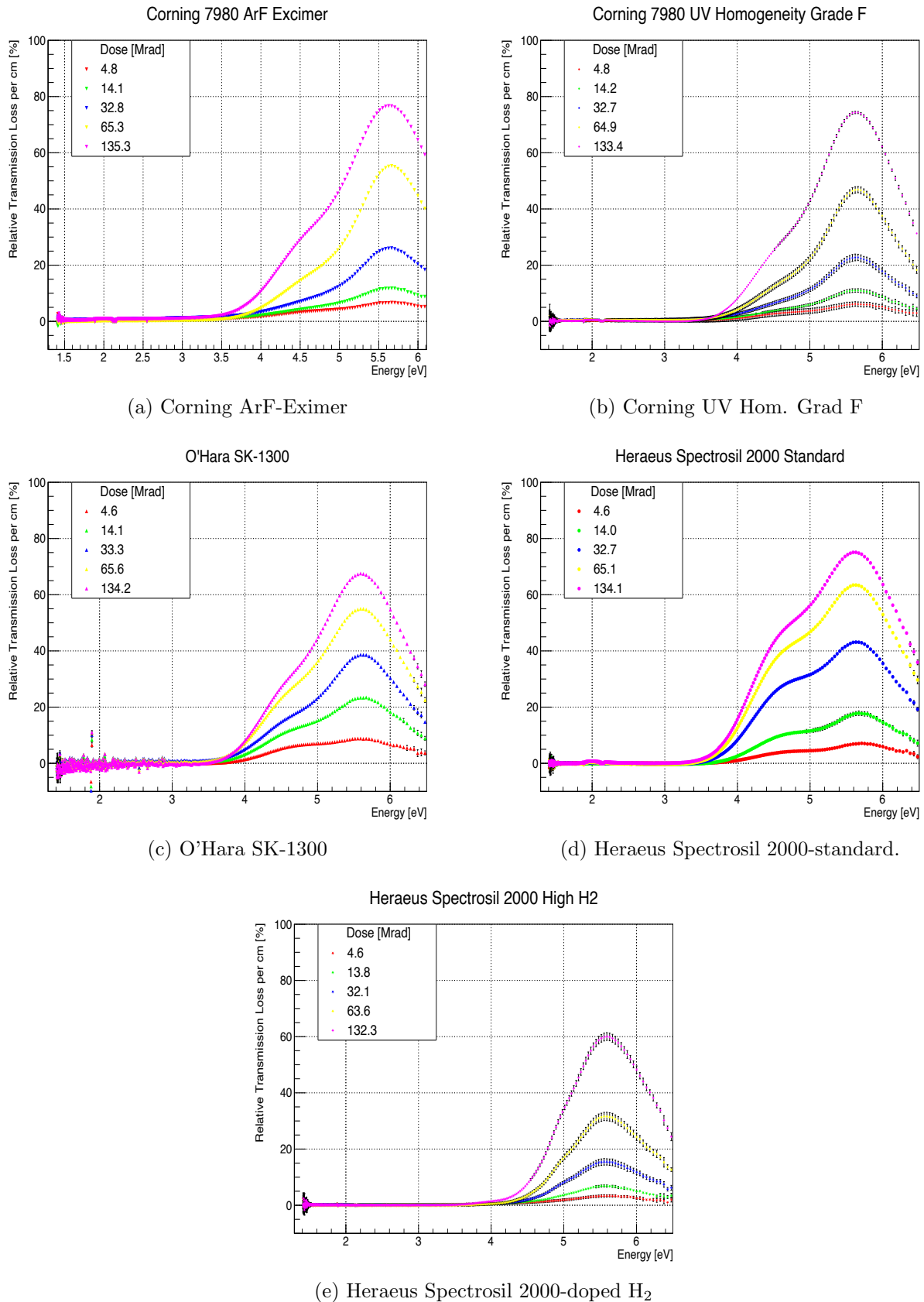


Figure 4.6: The March 10<sup>th</sup> relative light transmission losses for each sample at each dose with  $\delta_{T_l}$  error bars.

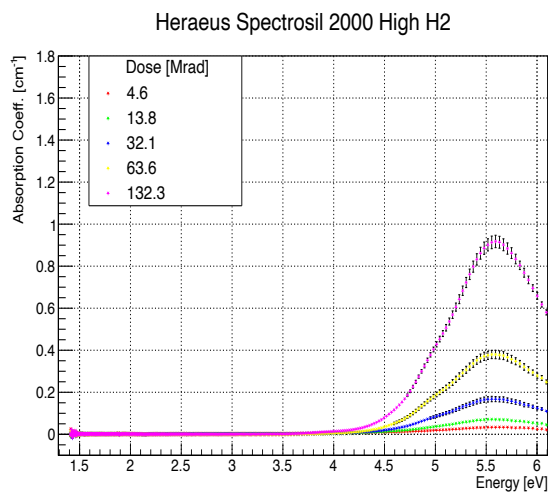
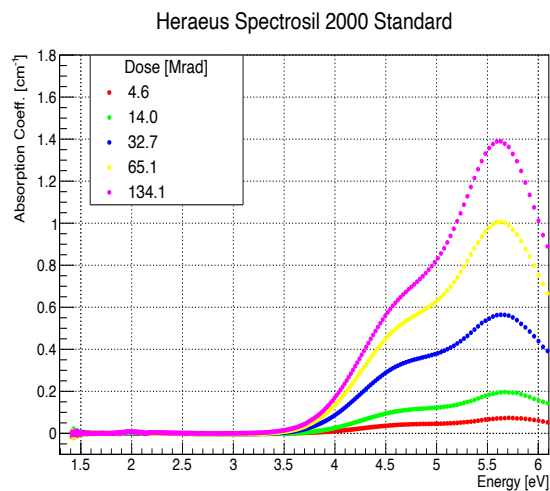
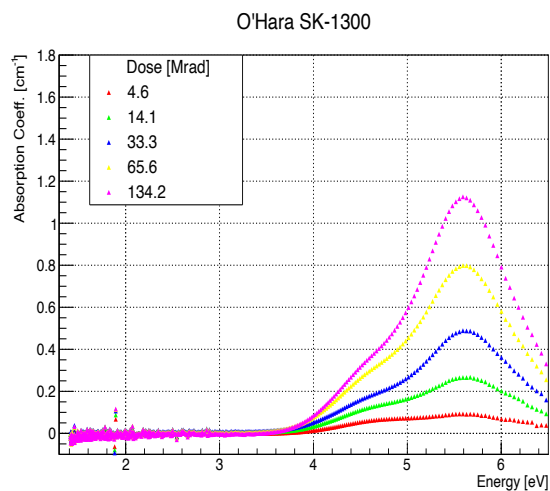
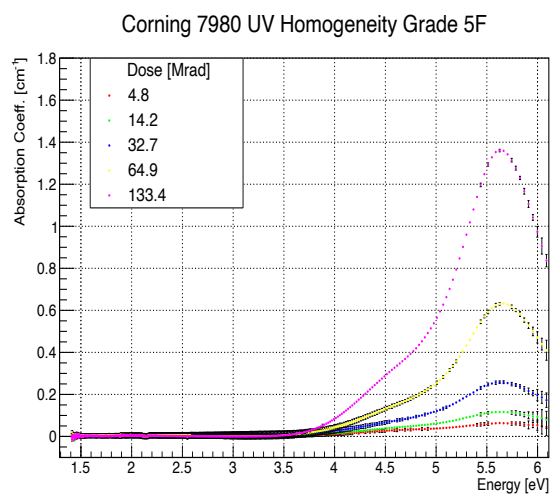
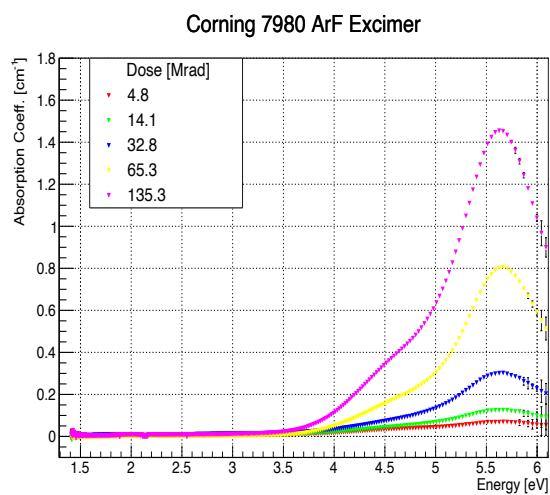


Figure 4.7: The March 10<sup>th</sup> absorption coeff. for each sample at each dose with

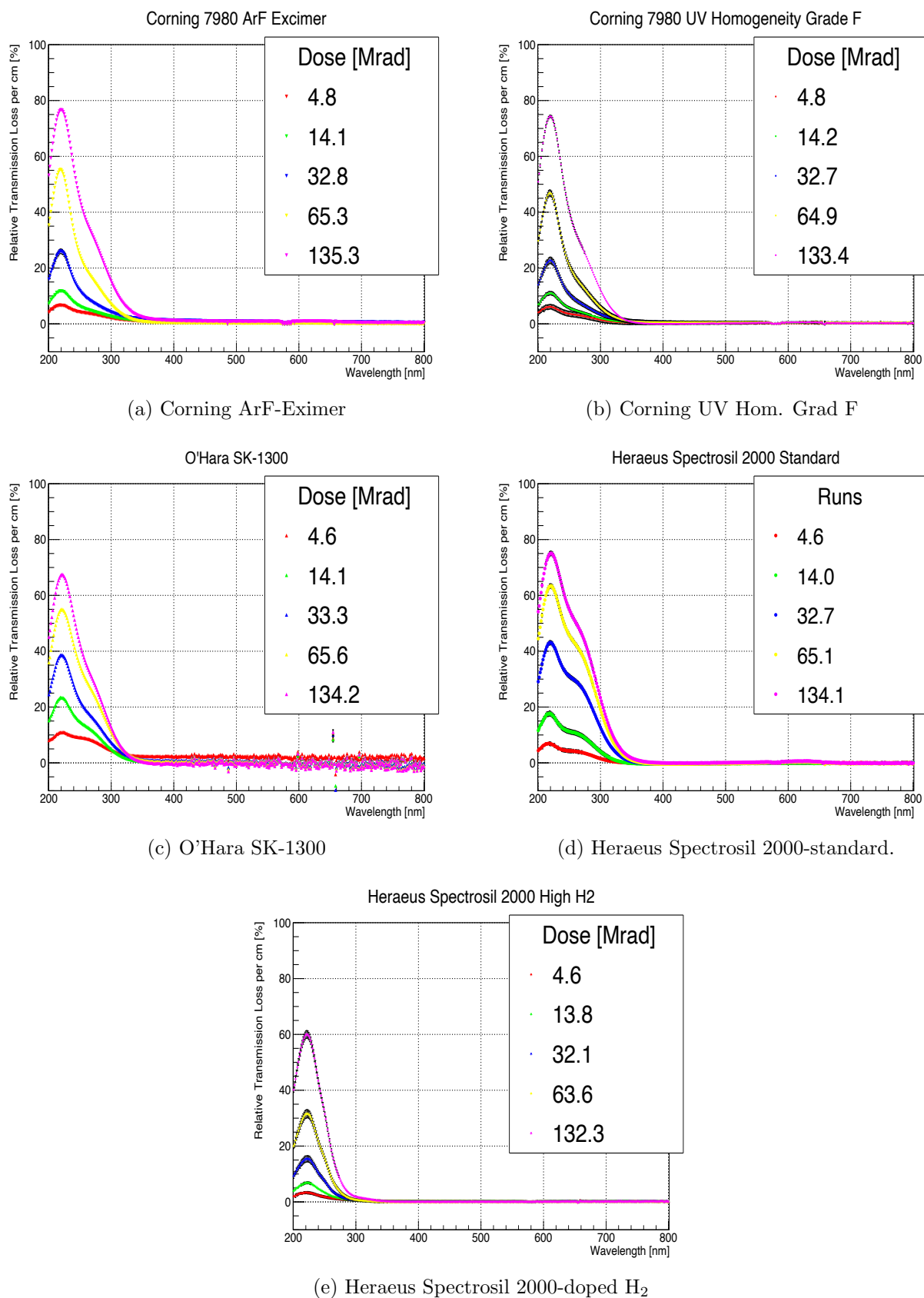


Figure 4.8: The March 10<sup>th</sup> relative light transmission losses versus wavelength for each sample at each dose with  $\delta_{T_i}$  error bars.

## 4.2 Dose

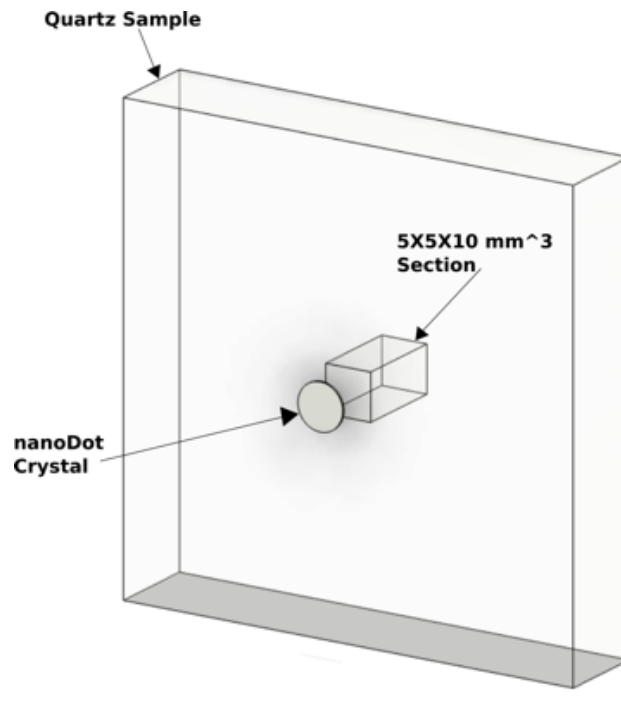


Figure 4.9: This cartoon shows the size and placement of the OSLD crystals that are irradiated to obtain a dose estimate for the corresponding  $5 \times 5 \times 10 \text{ mm}^3$  section of the HPFS samples.

Quantifying the dose consists of three steps

1. Dose is measured on an OSLD then normalized to the charge  $\frac{\text{dose}_{\text{OSLD}}}{\text{nC}}$  (read as dose per nano-Coulomb)
2. OSLD dose is then converted to dose on the HPFS  $\frac{\text{dose}_{\text{HPFS}}}{\text{nC}}$
3. The HPFS dose is then scaled by the total charge for each run

Measuring the charge in all cases is described in Section 3.2.3, with the results shown here in Section 4.2.2. The conversion of dose in an OSLD to dose in the HPFS is found using G4 simulation and is described in Section 4.2.1. The results for the OSLD measurements

are given in Section 4.2; these calculations involved a separate study using a cesium source to calibrate the dosimeters, described in appendix B.

### 4.2.1 G4 Simulation Results

Originally, the simulated beam was designed to physically match, as close as possible, the real beam; this involved “beam characterization measurements” that can be found in appendix C). Nevertheless, after simulating the  $\sim$ full phase space of the two beam parameters, a constant conversion factor was found that relates dose on an OSLD to dose in HPFS. This conversion factor does not depend on the simulated beam parameters and does not change, as long as the OSLD and the corresponding HPFS sections are orthogonal to the beam center<sup>2</sup> and the energy of the beam is approximately correct.

This constant ratio is because the dose is determined by the total flux of energized particles (mostly 8 MeV electrons). As shown in Figure 4.9, the same flux is seen by the OSLD and the corresponding center  $5 \times 5 \times 10 \text{ mm}^3$  section of HPFS. The only exceptions are a non-orthogonal beamline setup, or a highly divergent beam where particles pass through an OSLD but not through the HPFS section or vice versa. However, this is not the case in any of these measurements. The laser aligning procedure combined with the custom sample holders and beam stand ensures precise, repeatable sample placement in the beamline.

Figure 4.10 shows a graph of dose in the OSLD to dose in the HPFS over a large phase space of beam parameters. The points represent the same beam parameters for both materials (OSLD and HPFS), with their dose-responses graphed against each other. This graph shows that there is a constant ratio regardless of the parameters used. The slope of the line 0.97 gives the conversion between the dose in the two materials.

The beam parameters simulated range from 0 – 3 degrees angular sigma and 0 – 3 cm radial sigma, which, as shown in Figure 4.11 is far more dispersed than anything seen using our beam setup.

---

<sup>2</sup>hence the alignment procedure in Section 3.2.1

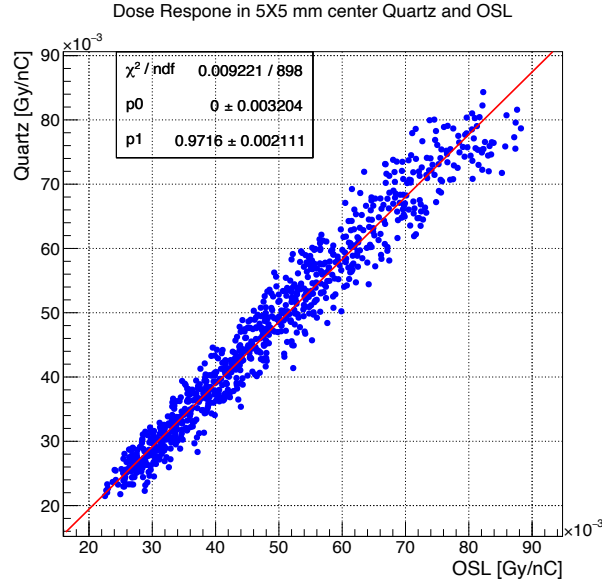
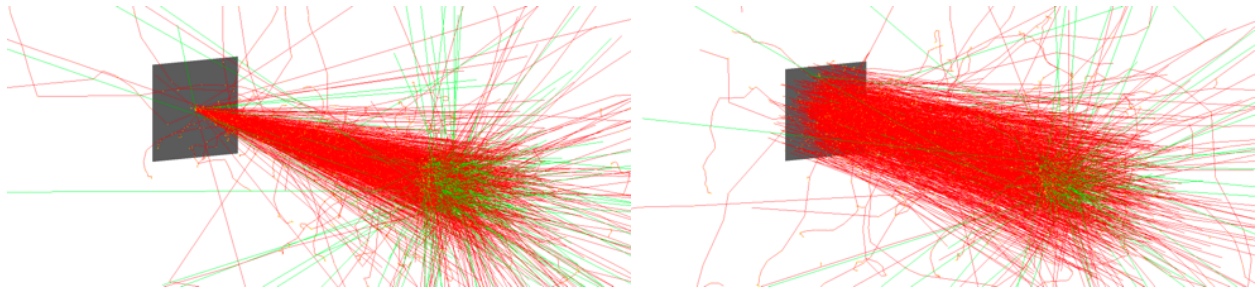


Figure 4.10: Simulated HPFS sample dose in center section ( $5 \times 5 \times 10 \text{ mm}^3$ ) versus simulated OSLD dose. These data points come from simulating and obtaining a dose in both materials across the phase space of beam parameters. This shows the highly correlated distribution and linear fit.



(a) Angular sigma = 0 degrees, radial sigma = 0 cm (b) Angular sigma = 3 degrees, radial sigma = 3 cm

Figure 4.11: These show the influence of the beam parameters on the simulated beam distribution. In (b), the distribution is larger than anything we measured. The dark square in these visualizations represents the beamline vacuum exit window. This has the correct thickness and material type but is larger than the actual exit window for the real beam.

$$\begin{aligned} \frac{\text{dose}_{\text{HPFS}}}{\text{nC}} &= C * \frac{\text{dose}_{\text{OSLD}}}{\text{nC}}, \\ \frac{\text{dose}_{\text{HPFS}}}{\text{nC}} &= 0.97 * \frac{\text{dose}_{\text{OSLD}}}{\text{nC}}, \end{aligned} \quad (4.2)$$

where  $C$  is the conversion factor,  $C = 0.97$ .

## 4.2.2 Charge

The charges for the OSLD data are recorded manually. But, due to technical constraints, the charge for the HPFS runs must be averaged. The oscilloscope averages 256 pulses, and one of these averages is saved to an output file every 60 seconds. These averages are distributed for each run, giving a mean and a standard deviation. Figure 4.12 shows the distribution for both beamdays.

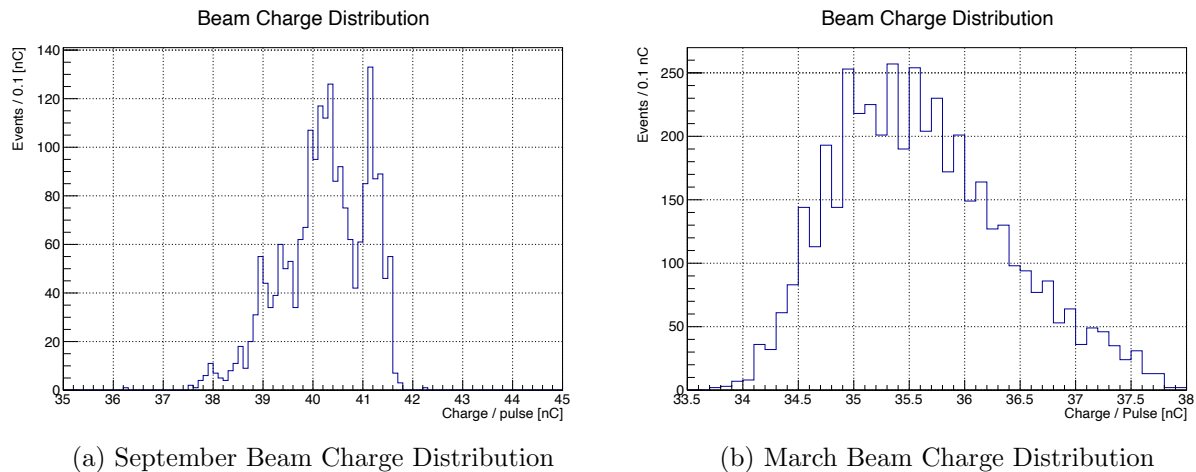


Figure 4.12: This is the charge distribution as measured throughout the entire day across all irradiations in both September and March. Note, the x axis scales are different; the distributions each have a 1 – 2 % RMS/Mean.

For the March beamday, the average charge per beam pulse on sample was approximately 36 nC. In September the average charge per beam pulse was approximately 40 nC. Each sample is irradiated for  $\sim 16\text{k}$ ,  $32\text{k}$ ,  $64\text{k}$ ,  $112\text{k}$ ,  $240\text{k}$  pulses in five successive runs with light transmission measurements in between runs.

## 4.2.3 nanoDot OSLD Results

Appendix B details the Cs-137 calibration measurements performed on the nanoDots for this experiment. Figure 4.13 shows a fit made from this data. This fit is used to map PMT counts, recorded in the microStar reader, to dose values. These dose values are then

normalized to the total charge exposed to the OSLDs. The average  $\frac{dose_{OSLD}}{nC}$  in March was 8.5 rad/nC, and in September the average was 9.2 rad/nC.

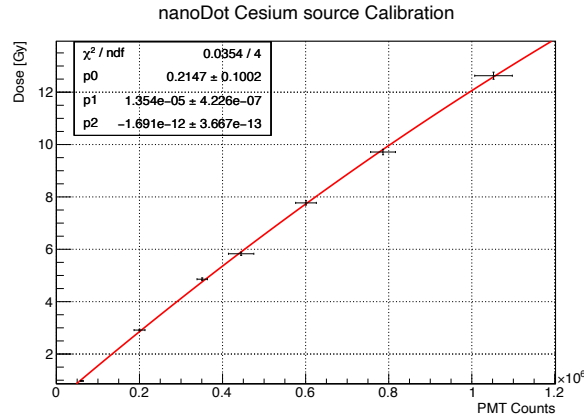


Figure 4.13: This graph shows the calibration fit for the nanoDot OSLDs used in this experiment. This fit shows a good agreement with the data. The calibration measurements can be found in Appendix B.

The error in the OSLD dose estimate is 7.6 %. This is based on the OSLD PMT count repeatability and the error on the cesium source activity.

#### 4.2.4 Dose Results

The dose for the  $5 \times 5 \times 10 \text{ mm}^3$  section of HPFS, referred to as  $Dose_{HPFS}$ , is calculated as follows

$$dose_{HPFS} = 0.97 \cdot \frac{dose_{OSLD}}{nC} \times (\text{average charge per pulse}) \times (\# \text{ pulses}). \quad (4.3)$$

Propagating the uncertainties for the  $\frac{dose_{OSLD}}{nC}$  and the average charge per pulse, the absolute error on the dose values is  $\sim 7.8 \%$ . The accumulated dose values for each sample, at each run, on both beam days are given in Tables 4.1 and 4.2.

Cumulative Dose [Mrad] March 10 <sup>th</sup>					
Sample	1 <sup>st</sup> Run	2 <sup>nd</sup> Run	3 <sup>rd</sup> Run	4 <sup>th</sup> Run	5 <sup>th</sup> Run
Heraeus-standard	4.6 ± 0.3	14.0 ± 1.1	32.7 ± 2.5	65.1 ± 4.9	134.1 ± 10.2
Heraeus-doped	4.7 ± 0.3	13.8 ± 1.0	32.1 ± 2.4	63.6 ± 4.8	132.3 ± 10.1
O'Hara SK-1300	4.6 ± 0.4	14.1 ± 1.1	33.3 ± 2.5	65.6 ± 5.0	134.2 ± 10.2
Corning UV-HGF	4.8 ± 0.4	14.2 ± 1.1	32.7 ± 2.5	64.9 ± 4.9	133.4 ± 10.1
Corning ARF-Ex	4.8 ± 0.4	14.1 ± 1.1	32.8 ± 2.5	65.3 ± 5.0	135.3 ± 10.3

Table 4.1: The cumulative peak dose in each sample for the March irradiation run.

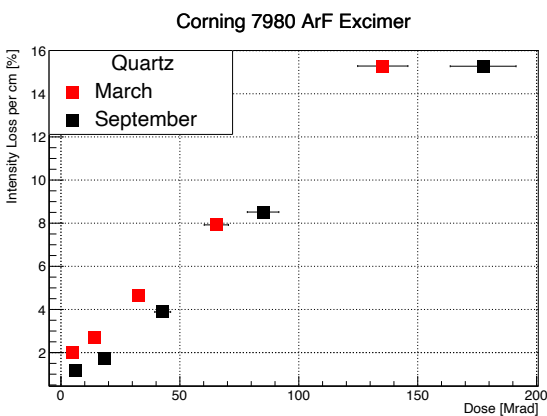
Cumulative Dose [Mrad] September 2 <sup>nd</sup>					
Sample	1 <sup>st</sup> Run	2 <sup>nd</sup> Run	3 <sup>rd</sup> Run	4 <sup>th</sup> Run	5 <sup>th</sup> Run
Heraeus-standard	6.0 ± 0.5	18.1 ± 1.4	41.8 ± 3.3	84.0 ± 3.3	177.4 ± 13.8
Heraeus-doped	6.3 ± 0.5	19.0 ± 1.5	43.8 ± 3.4	87.0 ± 6.8	177.5 ± 13.8
O'Hara SK-1300	6.3 ± 0.5	19.0 ± 1.5	44.3 ± 3.5	88.1 ± 6.9	180.56 ± 14.1
Corning UV-HGF	6.3 ± 0.5	18.8 ± 1.5	43.6 ± 3.4	86.5 ± 6.7	179.3 ± 14.0
Corning ARF-Ex	6.2 ± 0.5	18.5 ± 1.4	42.8 ± 3.3	85.0 ± 6.6	177.5 ± 13.8

Table 4.2: The cumulative peak dose in each sample the September irradiation run.

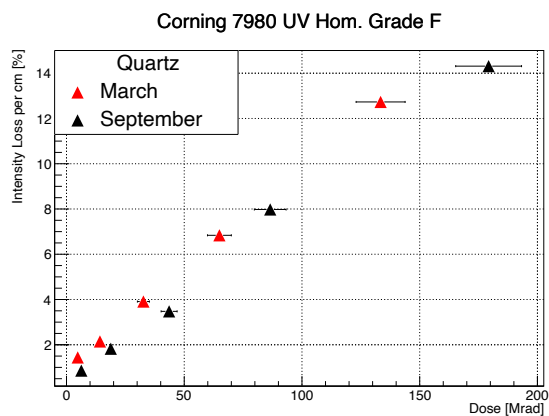
### 4.3 Intensity Loss by Dose

In order to quantify the net transmission losses in our samples due to radiation damage, we calculate a total intensity loss between 220 – 400 nm. This wavelength region is the most important for Cherenkov light losses and is also the most sensitive spectral region for the LTA. The total intensity loss is calculated using the raw background corrected data summed over the  $\sim 0.3$  nm wavelength bins,  $S_i = \sum_{\lambda=220}^{400} I_{\lambda}$ . The difference between the pre- and post-irradiated sums,  $S_0 - S_d$ , is taken and divided by the initial (pre-irradiated) sum. The uncertainty for each sum is the uncertainty in each intensity added in quadrature. The uncertainty in the total intensity loss is then found in the same way reported in appendix A. The Total Intensity Loss in percent is given by

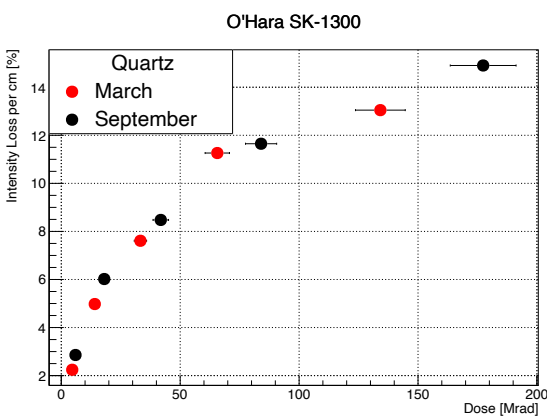
$$\text{Total Intensity Loss [\%]} = \frac{S_0 - S_d}{S_0} * 100. \quad (4.4)$$



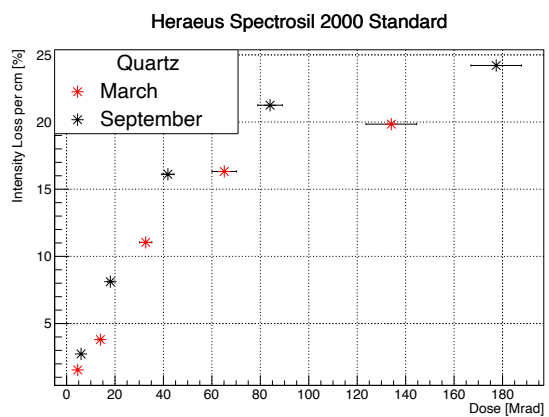
(a) Corning ArF-Eximer



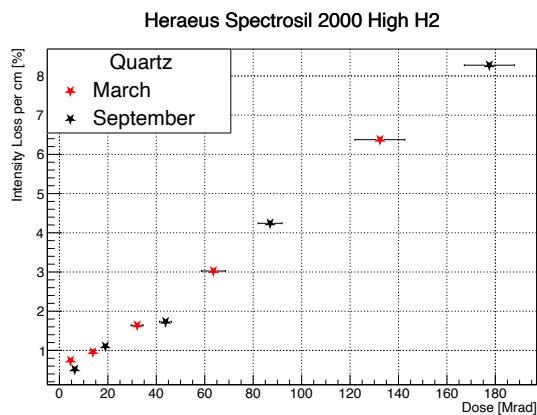
(b) Corning UV Hom. Grad F



(c) O'Hara SK-1300



(d) Heraeus Spectrosil 2000-standard.



(e) Heraeus Spectrosil 2000-doped

Figure 4.14: These graphs show the intensity light loss as a function of dose of both the March 10<sup>th</sup> and September 2<sup>nd</sup> measurements. The intensities are summed from 220 – 400 nm

Total Intensity Loss [%] at Approximate Dose March 10 <sup>th</sup>					
Sample	5 Mrad	14 Mrad	33 Mrad	65 Mrad	134 Mrad
Heraeus-standard	$1.55 \pm 0.02$	$3.81 \pm 0.02$	$11.04 \pm 0.02$	$16.32 \pm 0.02$	$19.84 \pm 0.02$
Corning ArF-Ex	$2.00 \pm 0.02$	$2.69 \pm 0.01$	$4.65 \pm 0.01$	$7.92 \pm 0.01$	$15.29 \pm 0.01$
O'Hara SK-1300	$2.24 \pm 0.02$	$4.98 \pm 0.01$	$7.61 \pm 0.01$	$11.26 \pm 0.01$	$13.05 \pm 0.01$
Corning UV-HGF	$1.44 \pm 0.03$	$2.15 \pm 0.01$	$3.90 \pm 0.02$	$6.84 \pm 0.04$	$12.73 \pm 0.01$
Heraeus-doped	$0.74 \pm 0.02$	$0.96 \pm 0.01$	$1.64 \pm 0.02$	$3.02 \pm 0.02$	$6.37 \pm 0.01$

Table 4.3: Total intensity loss between 220 – 400 nm at each cumulative dose level for the March run.

Total Intensity Loss [%] at Approximate Dose September 2 <sup>nd</sup>					
Sample	6 Mrad	18 Mrad	43 Mrad	86 Mrad	177 Mrad
Heraeus-standard	$2.74 \pm 0.01$	$8.12 \pm 0.01$	$16.11 \pm 0.02$	$21.25 \pm 0.01$	$24.21 \pm 0.03$
Corning ArF-Ex	$1.16 \pm 0.01$	$1.74 \pm 0.01$	$3.89 \pm 0.01$	$8.52 \pm 0.02$	$15.28 \pm 0.01$
Corning UV-HGF	$0.86 \pm 0.01$	$1.82 \pm 0.01$	$3.48 \pm 0.01$	$7.98 \pm 0.03$	$14.31 \pm 0.01$
O'Hara SK-1300	$2.86 \pm 0.02$	$6.02 \pm 0.02$	$8.48 \pm 0.02$	$11.65 \pm 0.02$	$14.91 \pm 0.02$
Heraeus-doped	$0.57 \pm 0.00$	$1.10 \pm 0.00$	$1.73 \pm 0.01$	$4.24 \pm 0.02$	$8.28 \pm 0.02$

Table 4.4: Total intensity loss between 220 – 400 nm at each cumulative dose level for the September run.

Figure 4.15 shows how all samples compare to each other in total light loss. At most dose levels, the Heraeus Spectrosil-2000 standard has the largest light loss; at  $\sim 177$  Mrad, it loses around 25 % of the relative light signal. While the Heraeus doped sample is the most radiation-resistant, showing only around 8 % losses  $\sim 177$  Mrad. The other samples show similar losses to each other, especially the two Corning samples, which are nearly identical.

Interestingly, the O'Hara SK-1300 sample, which is dry HPFS, performs worse than the Corning samples in the earlier dose ranges. But, then its rate of accumulating damage starts to level off; after  $\sim 135$  Mrad it performs similarly to the Corning samples, losing around 15% of transmitted intensity at the highest dose. The non-linear dose-response in the O'Hara HPFS is likely due to a “saturation” of the generation of specific defect centers. This type of saturation can also be seen in the Heraeus standard sample. Figure 4.14 shows the intensity loss for every sample. Most samples have a linear dose-response, but the O'Hara and the Heraeus standard samples show a breakdown of this linearity.

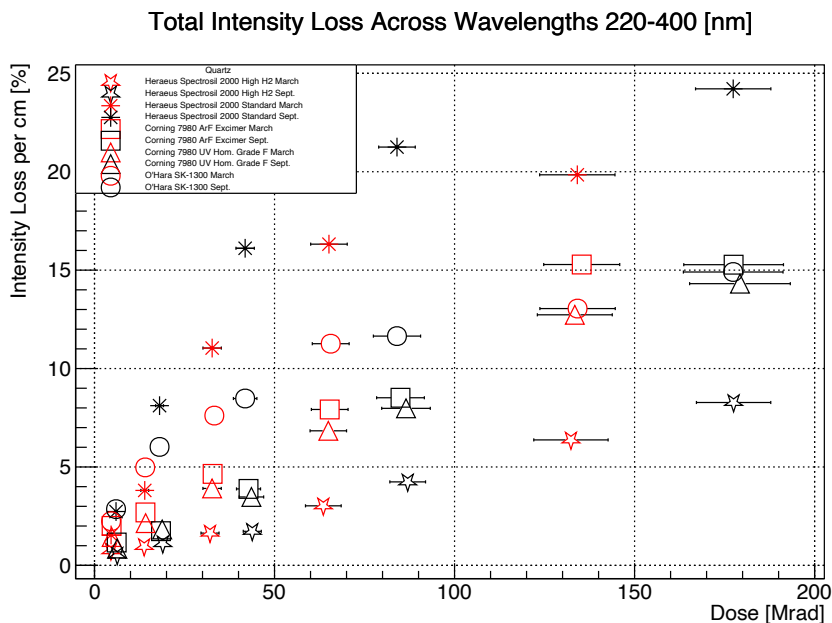


Figure 4.15: This graph shows all samples from both beamdays. You can see that the same brand samples all perform similarly to each other across both days. And there are clear differences between brands. Red symbols are results from March, while corresponding black symbols are from September.

## 4.4 Absorption Centers

As discussed in Section 2.3, the distribution of absorption losses is expected to be Gaussian. Many studies in the past have attempted Gaussian decompositions of absorption spectra. Nevertheless, in 2011 Skuja<sup>[5]</sup> found that the non-bridging oxygen hole center (NBOHC) distribution was a multi-Gaussian fit made of 5 overlapping functions when previously a single Gaussian had been used. Moreover, there are still un-quantified contributions to absorption from controversial defects such as the peroxy radical center (POR). It is our opinion that this indicates that Gaussian decompositions of absorption spectra are “risky” to trust. In private correspondence with Linards Skuja, he asserted that finding a unique decomposition is close to impossible because of many overlapping bands. We therefore do not attempt to fit the distributions. Despite this, we find evidence of many defect centers.

There is evidence for the most common absorption bands ( $E'$ , NBOHC) in the light transmission loss measurements and absorption coefficients in Figures 4.3-4.8. The large

peak on the right in all samples is consistent with  $E'$ -centers, although our peak has a center closer to 5.6 eV for all samples rather than the standard 5.8 eV. This difference is likely due to the steep efficiency drop-off of the LTA in this region as pointed out in Section 3.1.1. The shoulder to the left of the large peak in most samples (accept the Heraeus doped) is associated with NBOHCs<sup>[8,22]</sup>. These results are in line with many previous findings<sup>[8,22]</sup>; looking at other data sets is more interesting.

We took several data sets using different methods, such as leaving samples exposed to the UV light source of the deuterium lamp (UV bleaching) for a given amount of time. Irradiating the samples at a much higher dose rate, causing an increase in their temperature. Taking differences between transmission spectra for different dose levels and differences between the two Heraeus samples, which are the same base material, but one has a higher  $H_2$  content. Figure 4.16 shows the results of these analyses.

First, by zooming in on the visible region, we see in at least two samples an absorption band centered close to 2 eV (Figure 4.16a); this is a well-known NBOHC absorption band. Figure 4.16b shows UV bleaching results of all samples. These are graphed as a transmission loss for consistency, so negative values indicate a gain in transmitted light intensity.

We irradiated a previously dosed Corning UV homogeneity grade 5F sample at a much higher dose rate to look for temperature effects. This sample reached temperatures  $\gtrsim 100$  °C<sup>3</sup>. Figure 4.16c displays the results. Light transmission increased below 5.1 eV; this indicates that the NBOHCs were annealing away, while the  $E'$ -centers continued to show damage.

In a follow-up test after the March beamday exposures and measurements, we exposed all the irradiated samples to the deuterium lamp (UV bleaching) for 10 minutes and then re-measured the light transmission. Figure 4.16b displays the results of this test. All samples started to see the generation of NBOHCs or possibly hydrogen hole centers. All samples except the Heraeus doped sample show the annealing of a peak around 5.6 eV; these are the  $E'$ -centers. The corning samples show a slight shift of the peak to 5.5 eV. This shift is most

---

<sup>3</sup>The regular samples were kept below 40 °C during irradiation

likely due to the overlapping NBOHC and  $E'$ -center distributions; one is increasing, and one is decreasing. An interesting feature can be seen in the Corning samples. They both have a small annealing “bump” around 4.5 eV. This bump may indicate there is another absorption center involved in the region.

Figure 4.16d gives the differences between the doped and the standard Heraeus samples at every dose. From the beginning, two peaks are noticeable; these again are the NBOHC and the  $E'$ -centers. By the last dose, a prominent NBOHC peak around 4.6 eV (plus the small peak around 1.9 eV) develops with a smaller peak around the  $E'$ -centers. These results strongly indicate that the NBOHCs are primarily affected by the doping of  $H_2$ , and to a lesser extent, the  $E'$ -centers, especially in the lower dose ranges. However, in between those centers looks to be a formation of another peak.

By taking the differences in the spectra at different dose levels, we thought that separate peaks might start to develop. The idea is that some centers may saturate first, then the growth of others will become more prominent. Examining the difference in spectra between the fourth and fifth dose runs for both Corning and the Heraeus standard samples on both beamdays, an interesting peak is visible; Figure 4.17 displays the graph. This peak is interesting because it is centered on an energy  $\sim 5.2 - 5.4$  eV, where there is no well-established connection to a defect center.

We did not take EPR measurements in this experiment, and we cannot connect this peak to an EPR signal of a known defect. Nevertheless, we can make the following argument. This peak is only visible in wet samples not doped with  $H_2$ . Wet HPFS is oxygen-rich and likely more susceptible to oxygen-excess-related defects such as NBOHCs, PORs, and interstitial  $O_2$ . This peak is not an NBOHC or interstitial  $O_2$ , which is thought to have peaks around 1.62 and 0.975 eV<sup>[22]</sup>. However, a peak at 5.4 eV has been found for surface POR defects<sup>[25]</sup>. Moreover, it has been suggested that the bulk absorption could be at 4.8, 5.4, 4.3, and 5.1 eV<sup>[22,24]</sup>.

We suggest here that this absorption center could be the POR defect based on the location

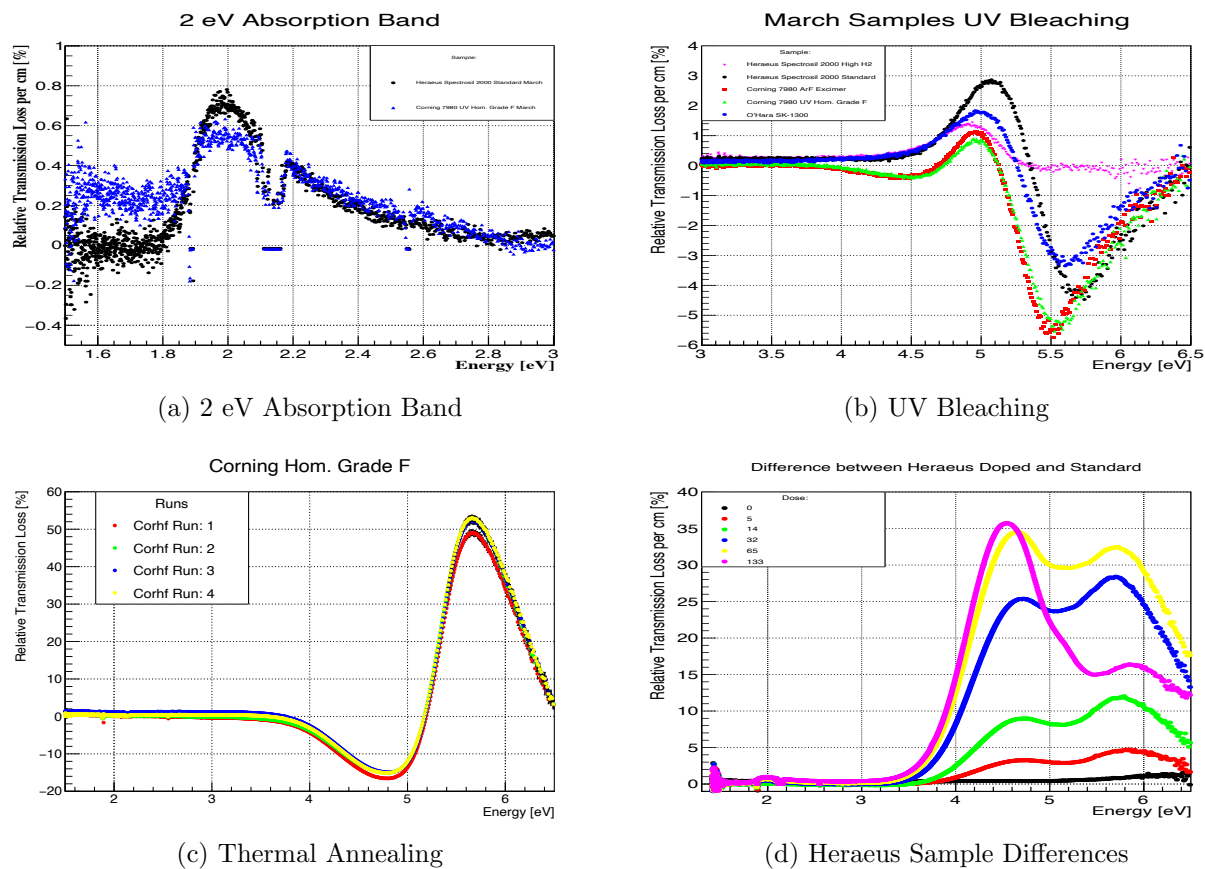


Figure 4.16: This graph shows the difference between the standard and the doped Heraeus samples at  $\sim 135$  Mrad. It's clear there is a large peak around 4.6 and a tail going into the Vis-UV region.

of the peak, and it is only present in samples where the potential for oxygen excess-related defects is more significant.

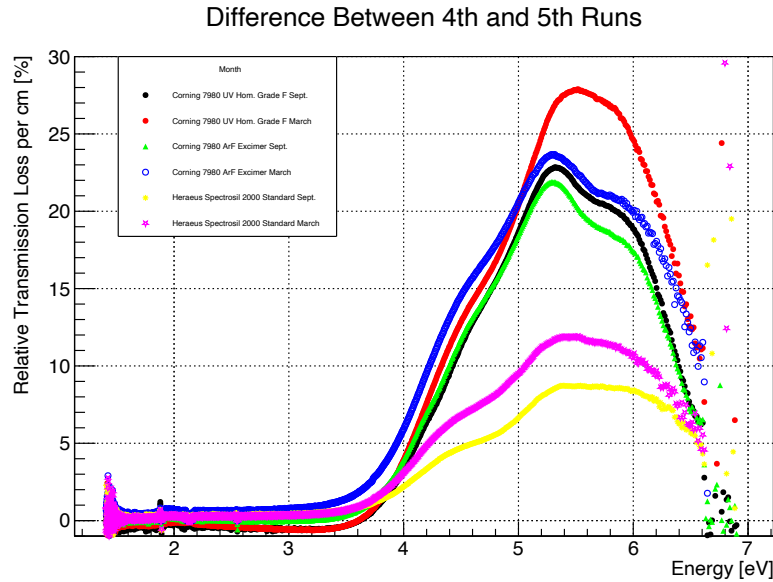


Figure 4.17: The peak around 5.3 eV can be seen in all of these samples. It is especially prominent in the Corning samples, with the 7980 ArF Excimer brand showing clear peaks.

## 4.5 General Discussion

### Applications to MOLLER, DIRC Limitations, and Next Steps

Applying our measurements and data to actual losses in Cherenkov detectors is a nuanced exercise. The Cherenkov light will “bounce” around a significant distance inside the HPFS before finally exiting. Furthermore, the dose in the HPFS would not likely be uniform. That means the light will encounter varying levels of damaged centers along its path, making the total light loss that the detector will experience more challenging to calculate. As the next step, the absorption coefficients will be used in a G4 optical simulation of the DIRCs in MOLLER. This simulation will provide a more accurate estimate of these detectors’ signal losses over the lifetime of MOLLER.

Another consideration is the temperature reached by the samples during the irradiations. The dose received on HPFS tiles will accumulate over months and years in the MOLLER experiment. While in this experiment, the doses were achieved in minutes and hours, at a much higher flux, increasing their temperature to  $\sim 35$  °C. We measured the annealing of

the NBOHCs at 100 °C, and we stayed well below that. However, the temperature increase from room temperature to 35 °C may affect these results.

## **POR**

The possible POR peak (Figure 4.17) is found by taking the difference between the light transmission spectra of the fourth and fifth dose runs; the peaks are not prominent in the corresponding absorption coefficient differences. Apparently, taking the natural log of the ratios of intensities, “washes out” this feature. Perhaps this washing out is why it has not been thoroughly studied in the literature.

For short distances it is not uncommon to approximate the absorption coefficient with  $\alpha_{\gamma}xI_0 = I_d$ . Where  $x$  is the distance through the material,  $I_0$  is the incident intensity, and  $I_d$  is the transmitted intensity. With  $x = 1\text{cm}$ , our light transmission measurements are equal to  $1-\alpha_{\gamma}$ . This means our light transmission measurements are just that when using a short-distance approximation.

We can not conclusively say that the POR causes this peak in transmission spectra as we made no other complimentary measurements such as electron paramagnetic resonance (EPR). A next step would be to repeat the process while taking (EPR) measurements, tying absorption to POR concentration. Also, the UV bleaching data from the Corning samples in Figure 4.16b shows a small bump around 4.5 eV, possibly indicating another absorption center in the region. A more careful study of UV bleaching may combine these efforts and produce a more precise result.

## **Comparison to Other Works**

Our absorption coefficients and light transmission losses align with hundreds of published papers on HPFS and the defect centers generated by ionizing radiation. Here we compare papers that had similar applications to our experiment, that is, using HPFS as a Cherenkov radiator.

Our findings agree with Tannoudji<sup>[2]</sup> in that transmission losses were detected. Although, their experiment used doses far less than in this experiment. Another caveat is that they reported their findings in Roentgens, a measure of the electric charge freed (in the form of ionizing particles) in air (and only in air) from X-rays or gammas; it is not a measure of energy deposition in a material. They point this out in their paper. It is not trivial to go from an exposure reading in an ion chamber to a deposited dose in material, especially without using simulation.

However, our findings conflict with Hoek<sup>[3]</sup>, they found no losses in their synthetic fused silica samples at the 10 Mrad dose level. A possible reason for this is inaccurate dose estimations. It is not clear how they calculated the dose in their experiment. Our experiment used 8 MeV electrons, as shown in Figure 2.13, most of the dose will deposit in the first 1 cm of the HPFS. It is not the same for a 150 MeV proton used in their experiment. Also, different sample brands were investigated in their experiment, although the Heraeus Suprasil they investigated is thought to be less radiation hard than the materials used here. Nevertheless, from our results, it is clear that every sample looked at showed losses in the UV region at doses as small as 4.5 Mrad.

### **Other Considerations**

The area the HPFS is measured through is important because the dose distribution is not uniform. Figure C.6 shows an example of the distribution from a beam simulation. In addition, there can be differences between volumes even in the same sample, of the number of sensitive precursors like peroxy linkage or three numbered rings as in Section 2.3. As a result, our dose calculations and light transmission measurements are only accurate for the exact volume we calibrated with the OSLD and measured through with the LTA.

## Chapter 5

### Conclusion

This analysis shows how the five HPFS samples compare in radiation hardness. We also estimates the light losses the MOLLER experiment can expect in the dose range of 5-175 Mrad. We find that Heraeus Spectrosil-2000 doped with H<sub>2</sub> is the most radiation-hard substance showing only around 8% losses at  $\sim 177$  Mrad. The Corning samples 7980 ArF Excimer, and UV 7980 Homogeneity grade 5F outperformed the O'Hara SK-1300 sample in the range below  $\sim 135$  Mrad. However, at the highest doses, greater than  $\sim 135$  Mrad, the O'Hara performed slightly better than the Corning 7908 UV Homogeneity Grade F, with all three samples showing around 15% losses at the highest dose. At every dose greater than  $\sim 15$  Mrad, the standard Heraeus Spectrosil-2000 performed the worst, showing losses over 24% in total. Heraeus makes both the best and worst performing samples; both are Spectrosil-2000, which shows the effectiveness of the H<sub>2</sub> doping on radiation resistance.

All samples exhibit the most common absorption center, the E'-center. Moreover, all the samples except the doped Heraeus show signs of the NBOHC around 4.6 eV, and the 1.9 eV NBOHC band is seen in several samples. Furthermore, new evidence of the POR absorption center is possibly detected in our wet HPFS samples, giving it a bulk absorption peak at  $\sim 5.3$  eV.

## REFERENCES

- [1] K. Kumar *et al.*, “The moller experiment: An ultra-precise measurement of the weak mixing angle using møller scattering,” arXiv:1411.4088 [nucl-ex], November 2014.
- [2] J. Cohen-Tanugi *et al.*, “Optical properties of the dirc fused silica cherenkov radiator,” *Nuclear Instruments and Methods in Physics Research A*, vol. 515, pp. 680–700, 2003.
- [3] M. Hoek *et al.*, “Radiation hardness study on fused silica,” *Nuclear Instruments and Methods in Physics Research A*, vol. 595, pp. 190–193, 2008.
- [4] C. D. Marshall *et al.*, “Induced optical absorption in gamma, neutron and ultraviolet irradiated fused quartz and silica,” *Journal of Non-Crystalline Solids*, vol. 212, no. 1, pp. 59–73, 1997.
- [5] L. Skuja *et al.*, “Visible to vacuum-uv range optical absorption of oxygen dangling bonds in amorphous  $\text{SiO}_2$ ,” *Phys. Rev. B*, vol. 84, p. 205206, Nov 2011. [Online]. Available: <https://link.aps.org/doi/10.1103/PhysRevB.84.205206>
- [6] P. Anthony *et al.*, “Precision measurement of the weak mixing angle in moller scattering,” *Physical Review Letters*, vol. 95, no. 081601, August 2005.
- [7] L. R. Drees *et al.*, *Silica in Soils: Quartz and Disordered Silica Polymorphs*. John Wiley & Sons, Ltd, 1989, ch. 19, pp. 913–974. [Online]. Available: <https://access.onlinelibrary.wiley.com/doi/abs/10.2136/sssabookser1.2ed.c19>

- [8] G. M. L. Piccolo *et al.*, “Intrinsic point defects in silica for fiber optics applications,” *Materials*, vol. 14, no. 24, 2021. [Online]. Available: <https://www.mdpi.com/1996-1944/14/24/7682>
- [9] J. Harison, “Quartz, tibet.” [Online]. Available: [https://en.wikipedia.org/wiki/File:Quartz,\\_Tibet.jpg](https://en.wikipedia.org/wiki/File:Quartz,_Tibet.jpg)
- [10] F. Kruijen, “A common form of tridymite.” [Online]. Available: [https://commons.wikimedia.org/wiki/File:Tridymite\\_tabulars\\_-\\_Ochtendung,\\_Eifel,\\_Germany.jpg](https://commons.wikimedia.org/wiki/File:Tridymite_tabulars_-_Ochtendung,_Eifel,_Germany.jpg)
- [11] R. Lavinsky, “Cristobalite.” [Online]. Available: <https://commons.wikimedia.org/wiki/File:Cristobalite-Fayalite-40048.jpg>
- [12] Materialschemist, “a-quartz.” [Online]. Available: <https://commons.wikimedia.org/wiki/File:A-quartz.png>
- [13] —, “b-quartz.” [Online]. Available: <https://commons.wikimedia.org/wiki/File:B-quartz.png>
- [14] —, “B-tridymite, red atoms are oxygens.” [Online]. Available: <https://commons.wikimedia.org/wiki/File:B-tridymite.png>
- [15] S. State, “Crystal structure of cristobalite.” [Online]. Available: <https://commons.wikimedia.org/wiki/File:B-cristobal2.png>
- [16] H. Group, Feb 2022. [Online]. Available: [https://www.heraeus.com/en/hca/fused-silica-quartz-knowledge\\_base\\_1/production\\_process\\_1/makingoffusedsilica\\_hca.html](https://www.heraeus.com/en/hca/fused-silica-quartz-knowledge_base_1/production_process_1/makingoffusedsilica_hca.html)
- [17] R. A. Huang Kun, “Theory of light absorption and non-radiative transitions in f-centres,” *Royal Society London*, vol. 95, no. A204406–423, 1950.
- [18] M. Leone *et al.*, “Chapter 1 - optical absorption, luminescence, and esr spectral properties of point defects in silica,” in *Silicon-Based Material and Devices*, H. S.

- Nalwa, Ed. Burlington: Academic Press, 2001, pp. 1–50. [Online]. Available: <https://www.sciencedirect.com/science/article/pii/B978012513909050012X>
- [19] R. K. Watts *et al.*, “Point defects in crystals,” *Berichte der Bunsengesellschaft für physikalische Chemie*, vol. 82, 1977.
- [20] T. D. Kühne, “Second generation car-parrinello molecular dynamics,” *Wiley Interdisciplinary Reviews: Computational Molecular Science*, vol. 4, no. 4, pp. 391–406, Jul 2014. [Online]. Available: <https://doi.org/10.1002%2Fwcms.1176>
- [21] D. L. GRISCOM, “Optical properties and structure of defects in silica glass,” *Journal of the Ceramic Society of Japan*, vol. 99, no. 1154, pp. 923–942, 1991.
- [22] L. Skuja, “Optically active oxygen-deficiency-related centers in amorphous silicon dioxide,” *Journal of Non-Crystalline Solids*, vol. 239, no. 1, pp. 16–48, 1998. [Online]. Available: <https://www.sciencedirect.com/science/article/pii/S0022309398007200>
- [23] R. Devine, “Macroscopic and microscopic effects of radiation in amorphous sio<sub>2</sub>,” *Nuclear Instruments and Methods in Physics Research Section B: Beam Interactions with Materials and Atoms*, vol. 91, no. 1, pp. 378–390, 1994. [Online]. Available: <https://www.sciencedirect.com/science/article/pii/0168583X94962537>
- [24] W. Wang *et al.*, “Structural and electronic properties of peroxy linkage defect and its interconversion in fused silica,” *Journal of Non-Crystalline Solids*, vol. 434, pp. 96–101, 2016. [Online]. Available: <https://www.sciencedirect.com/science/article/pii/S0022309315302957>
- [25] V. A. Radzig, “Point defects in disordered solids: Differences in structure and reactivity...” *Journal of Non-Crystalline Solids*, vol. 239, no. 1, pp. 49–56, 1998. [Online]. Available: <https://www.sciencedirect.com/science/article/pii/S0022309398007534>

- [26] S. Agostinelli *et al.*, “Geant4—a simulation toolkit,” *Nuclear Instruments and Methods in Physics Research Section A: Accelerators, Spectrometers, Detectors and Associated Equipment*, vol. 506, no. 3, pp. 250–303, 2003. [Online]. Available: <https://www.sciencedirect.com/science/article/pii/S0168900203013688>
- [27] G. Collaboration, “Geant4 a simulation toolkit: Guide for physics lists,” <https://geant4-userdoc.web.cern.ch/UsersGuides/PhysicsListGuide/BackupVersions/V10.6/fo/PhysicsListGuide.pdf>.
- [28] —, “Geant4 a simulation toolkit: Book for application developers,” <https://geant4-userdoc.web.cern.ch/UsersGuides/ForApplicationDeveloper/BackupVersions/V10.6/fo/BookForApplicationDevelopers.pdf>.
- [29] O. Optics, “Flame miniature spectrometer user manual,” Ocean Insight.
- [30] N. Pramanik *et al.*, “Radiation processing of nylon 6 by e-beam for improved properties and performance,” *Radiation Physics and Chemistry*, vol. 78, no. 3, pp. 199–205, 2009. [Online]. Available: <https://www.sciencedirect.com/science/article/pii/S0969806X08002818>
- [31] K. Krane, *Introductory Nuclear Physics*. John Wiley and Sons, 1988.
- [32] J. Lehmann *et al.*, “Angular dependence of the response of the nanodot osld system for measurements at depth in clinical megavoltage beams,” *Medical Physics*, vol. 41, no. 6Part1, p. 061712, 2014.
- [33] Heraeus, “Heraeus quartz glass for optics data and properties,” [https://www.heraeus.com/media/media/hca/doc\\_hca/products\\_and\\_solutions\\_8/optics/Data\\_and\\_Properties\\_Optics\\_fused\\_silica\\_EN.pdf](https://www.heraeus.com/media/media/hca/doc_hca/products_and_solutions_8/optics/Data_and_Properties_Optics_fused_silica_EN.pdf).
- [34] Corning, “Corning® hpfs® 7979, 7980, 8655 fused silica optical materials prod-

uct information,” [https://www.corning.com/media/worldwide/csm/documents/HPFS\\_Product\\_Brochure\\_All\\_Grades\\_2015\\_07\\_21.pdf](https://www.corning.com/media/worldwide/csm/documents/HPFS_Product_Brochure_All_Grades_2015_07_21.pdf).

- [35] Akselrod *et al.*, “Preparation and Properties of Alpha-Al<sub>2</sub>O<sub>3</sub>:C,” *Radiation Protection Dosimetry*, vol. 47, no. 1-4, pp. 159–164, 05 1993.
- [36] C. Harper, “Reproducibility of optically stimulated luminescence dosimeters in mixed radiation fields,” Master’s thesis, Idaho State University, 2018.
- [37] I. C. on Radition Units and Measurments, “Icru report 30, quantitative concepts and dosimetry in radiobiology,” April 1979.
- [38] L. M. Unger and D. K. Trubey, “Specific gamma-ray dose constants for nuclides important to dosimetry and radiological assessment,” 9 1981. [Online]. Available: <https://www.osti.gov/biblio/6246345>

# Appendix A

## Error Propagation

### Uncertainty Propagation L.T

To calculate the percentage of light lost through the irradiated samples, we take the difference between the unirradiated intensity  $I_0$  and the irradiated intensity  $I_d$ ,  $(I_0 - I_d)$ . This is then divided by the initial unirradiated intensity and multiplied by 100. The intensity for the background  $I_{back}$  (light source blocked) must also be subtracted out. The background is essentially constant and is treated as such (see Figure A.1); it, therefore, cancels out in the numerator. The equation for the transmission loss ( $T_l$ ) then becomes

$$T_l = \frac{I_0 - I_d}{I_0 - I_{back}} * 100. \quad (\text{A.1})$$

This equation gives the transmission loss between the unirradiated HPFS and its irradiated state as a percentage of the initial intensity. This calculation is done for every energy (or wavelength) individually.

The uncertainty for each intensity is found by obtaining the root mean square (RMS) of the intensity for each wavelength in all repeated measurements taken at each dose. Typically ten measurements were taken pre-irradiation and three after each dose. The RMS for  $I_0$  will be denoted as  $\sigma_0$  the RMS for  $I_d$  is  $\sigma_d$ . The uncertainty of a difference (with no covariance)

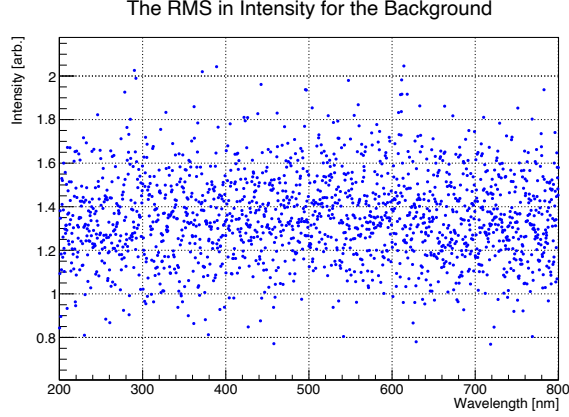


Figure A.1: The RMS in intensity for the background measurements throughout an entire beamday. This shows that the RMS is less than 2 intensity counts for any given wavelength. A typical measurement for intensity has counts in the tens of thousands. So the contribution to any error is  $\sim 0.02\%$  level which is far less than any other source and is ignored.

is given by

$$\begin{aligned}
 f &= A - B \\
 \sigma_f &= \sqrt{\sigma_A^2 + \sigma_B^2}.
 \end{aligned}
 \tag{A.2}$$

And the uncertainty of a quotient (with no covariance) is given by

$$\begin{aligned}
 g &= \frac{C}{D} \\
 \sigma_g &= |g| \sqrt{\left(\frac{\sigma_C}{C}\right)^2 + \left(\frac{\sigma_D}{D}\right)^2}.
 \end{aligned}
 \tag{A.3}$$

That makes the RMS for  $I_0 - I_d$  denoted as  $\sigma_1$

$$\sigma_1 = \sqrt{\sigma_0^2 + \sigma_d^2}.
 \tag{A.4}$$

And the uncertainty for  $T_l$  denoted as  $\sigma_{tl}$  would then be

$$\sigma_{tl} = |T_l| \sqrt{\left(\frac{\sigma_1}{I_0 - I_d}\right)^2 + \left(\frac{\sigma_0}{I_0}\right)^2}. \quad (\text{A.5})$$

However, there are fluctuations of intensity independent of these measurements. The light source fluctuations are measured by taking open air (no sample, only air) measurements between irradiation measurements. These are done throughout the day and have always been found to have  $\lesssim 0.1\%$  dispersion see Figure A.2. This uncertainty denoted as  $\sigma_{ls}$  adds in quadrature to  $\sigma_{tl}$ , giving final uncertainty in  $T_l$  denoted as  $\delta_{tl}$ . In the graphs below the light loss values are given in  $T_l \pm \delta_{tl}$  form.

$$\delta_{tl} = \sqrt{\sigma_{tl}^2 + \sigma_{ls}^2} \quad (\text{A.6})$$

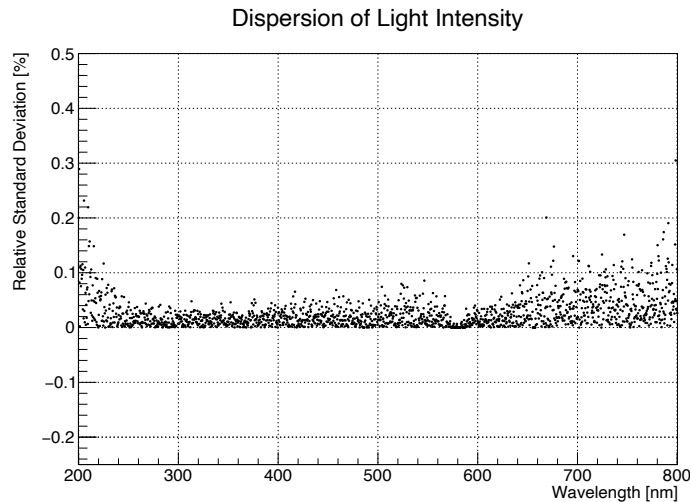


Figure A.2: This plot gives the percent variation in the 8 "open air" intensity measurements taken throughout the Corning UV 7980 Homogeneity grade 5F irradiations ( $\approx 1$  hour).

To represent  $\delta_{tl}$  as a percent error in the transmission loss measurements<sup>1</sup>. The relative standard deviation (RSD)<sup>2</sup> is used which is given by

<sup>1</sup>Which are themselves a percent change

<sup>2</sup>This quantity is a standardized measure of dispersion of a probability distribution

$$RSD_{T_l} = \frac{\delta_{t_l}}{T_l} * 100. \quad (\text{A.7})$$

For a graph of all the errors for each piece, dose, and wave lengths between 200-500 nm see Figure A.3. As is shown all uncertainties are well below  $\pm 1.5\%$  with almost all below  $\pm 0.5\%$ .

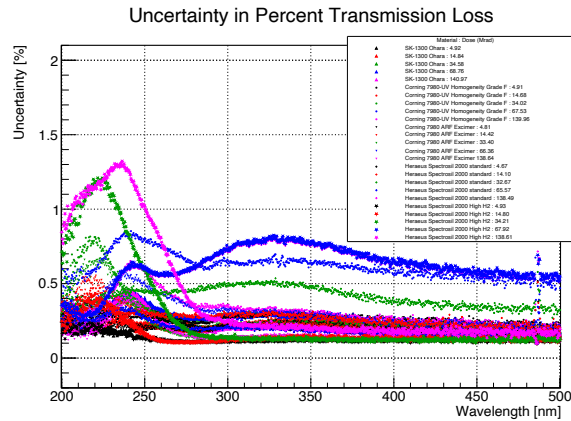


Figure A.3: The uncertainty for every piece at every dose in between wavelengths 200-500 nm

The uncertainty for the absorption coefficients given by equation 2.21 are a combination of equation A.3 and the uncertainty for a natural logarithm

$$f = \ln(D), \quad (\text{A.8})$$

$$\sigma_f = \frac{\sigma_D}{D}.$$

The final relative standard deviation for the absorption coefficients is given using equation A.7 and substituting  $\sigma_f$  and  $f$ .

## Appendix B

### Cesium-137 Measurements

We calibrated the nanoDot OSLDs using a cesium-137 source following the example of previous nanoDot calibrations<sup>[36]</sup>.

The cesium-137 Source mount is a J.L Shepherd and Assoc. Model 81-8B Irradiator S.N 7019 see Figure B.2. This source has a calibration certificate from the manufacturer made in 1984. The exposure was calibrated with a MDH Industries Model 2025 X-Ray Monitor, S.N. 2127, with a 180cc probe, S.N. 6105, and a 3cc probe, S.N. 4126. This detector, in turn, was calibrated using a MDH Industries Inc. Model 10X5-6 3-terminal ion chamber National Bureau of Standards (now National Institute of Standards and Technology NIST.) Report #DG 7856/82. The calibration sheet also states it is a 20 Ci source housed in an Amersham type X60/1 Capsule, S.N 00090EZ. It was certified on June 25th, 1984.

It was found that there was a discrepancy when calculating the exposure using the exponential decay of 20 Ci of cesium-137 and then comparing that to modern measurements of exposure. The actual exposure measurements from the 1984 calibration sheet were analyzed to investigate this problem.

In 1984 four exposure measurements at different distances were calibrated. The experimental uncertainty of the MDH detectors used in those exposure measurements is 5% according to a private correspondence with a J.L Shepherd employee. A  $\frac{1}{r^2}$  fit of the four

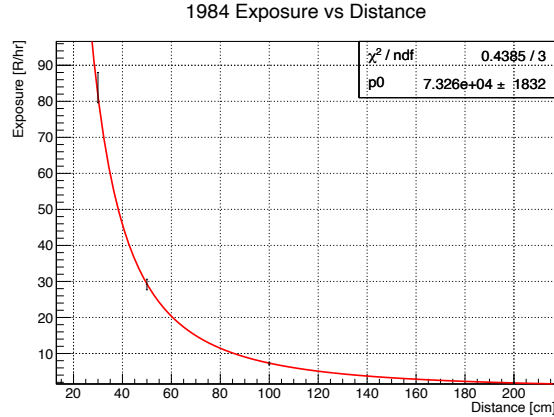


Figure B.1: Exposure Measurements of cesium-137 source June 1984

measurements was made as can be seen in Figure B.1. Using the equation for exposure

$$\dot{\chi} = \Gamma_{\delta} \frac{\alpha}{d^2}$$

[37] where  $\dot{\chi}$  is the exposure rate ( $\frac{C}{kg \cdot hr}$ ),  $\Gamma_{\delta}$  is the specific gamma ray constant also known as the gamma factor or the exposure rate constant ( $\frac{R \cdot cm^2}{hr \cdot mCi}$ ),  $\alpha$  is the activity of the source (mCi), and  $d^2$  is the distance from the source squared ( $cm^2$ ). Using the known value for the gamma ray constant of cesium-137 at 100 cm  $\Gamma_{\delta} = 3.3$ [38] and solving the fit parameter for the activity yields 22.2 Ci with an uncertainty of 0.56 mCi or  $\approx 2.5\%$ . We then took a series of exposure measurements on the source to compare to this calculation.

### B.0.1 Equipment used

A rotary stage, Ludlum model 9-4 ion-chamber, J.L Shepherd cesium source, video camera, tape measure.

### B.0.2 Methods

The Ludlum detector was placed with the bottom window facing the source window on top of a block of Styrofoam connected to a platform on the rotary stage shown in Figure B.3. The platform was placed as far away from the window as allowed, approximately 2.7 m. The



Figure B.2: J.L Shepherd cesium-137 source



Figure B.3: left) is an image of the Ludlum model 9-4 ion-chamber right) Image of the the experimental set up. The Ludlum detector sits window side facing the source window, on top of a Styrofoam block attached to a sliding platform connected to the rotary stage at the bottom.

source was turned on for a few seconds, the detector's readout was read using a camera that fed into a live readout in the operation room adjacent to the source room, and the source was turned off. The rotary stage was then moved forward by 1 inch, and the process was repeated up to approx. 26 cm away; this was the distance that the exposure was beyond the ability of the Ludlum detector to read.

### B.0.3 Results and Conclusions

A graph of the results can be seen in Figure B.4. The experimental uncertainty in the distance is based on the multiple measurements it takes to go from the source window to the center of the Ludlum detector  $\pm 0.57\text{cm}$ . The uncertainty in the exposure measurements comes from an energy dependence uncertainty of 20% and a reading error of  $\pm 1R$  or  $\pm 0.1R$ .

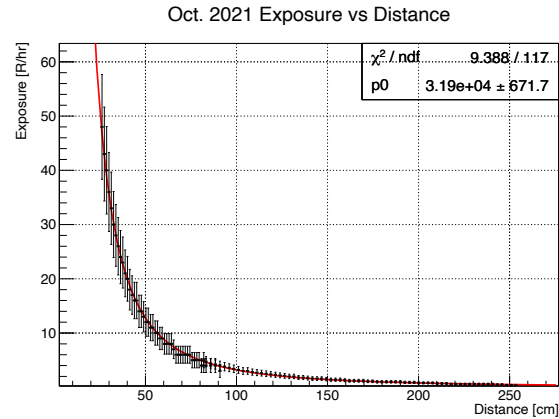


Figure B.4: Exposure Measurements of cesium-137 source Oct. 2021

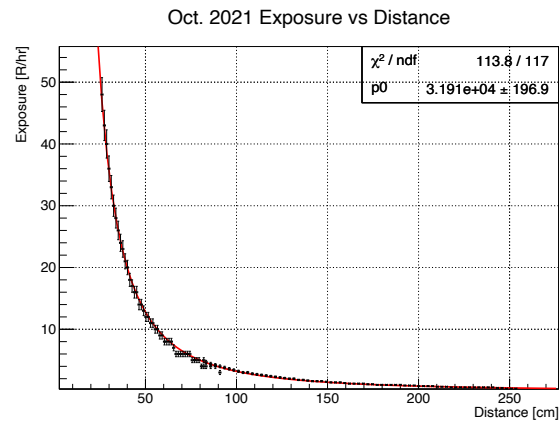


Figure B.5: Exposure Measurements of cesium-137 source Oct. 2021 revised error

depending on the range setting of the detector used. Combining these yields  $\approx 20\%$  error for the exposure rate. The value for the reduced chi-square is very small; this indicates that the estimated error is too high.

So, the error was corrected with the following  $\sigma_{ex_2}^2 = \sigma_{ex_1}^2 * \chi^2$ . This gave distance-dependent errors between 5.6-9%, with the closet distances all less than 6%. In a private conversation with a Ludlum employee, they stated that the error for exposure on a cesium 137 source should be below 10%. Our data seems to agree; a corrected graph can be seen in Figure B.5.

Using the fit data (the value  $p_0$ ) and the uncertainty in the exposure measurements, calculating a value for the activity of the source to be  $9.67 \pm 0.55$  Ci or  $\approx 5.7\%$  error. Using

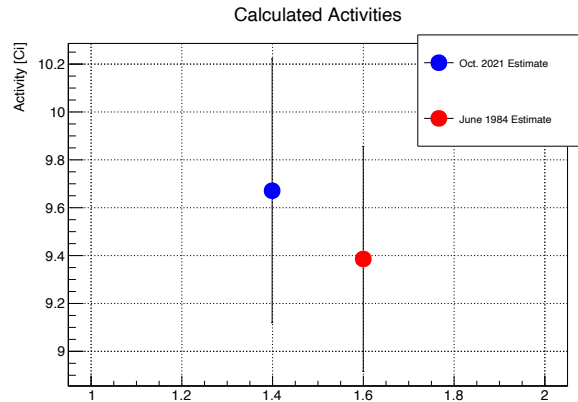


Figure B.6: Calculated Activities one from using exponential decay from 1984 and one from using the exposure measurements from 2021

the exponential decay of cesium-137 and applying it to the calculated activity of the source in 1984, the expected activity in Oct. 2021 is  $9.39 \pm 0.47$  Ci. A graph comparing these to calculated results can be seen in Figure B.6. These values lie within each other's error and are consistent with what is expected within experimental uncertainty.

Figure B.5 shows the exposure measurements fit a  $1/r^2$  drop in intensity as expected. For this to be true, a few assumptions must be true, the source is approximately spherical, and there is little to no attenuation of the gammas from the source to the detector. This first assumption is used in simulating the cesium source.

In a private correspondence with a radiation safety officer at ISU, it was learned that there might be a scattering problem with the room used, causing a higher exposure rate by as much as 5%. The radiation safety group at the university is no longer using the source to calibrate their equipment because of their findings. They used the source to calibrate their safety equipment and have standards that must be followed, which are not allowed by the room's geometry. However, this study finds that these measurements are within acceptable ranges of uncertainty to calibrate the OSL dosimeters. As reasonable verification of the source activity was still able to be determined when calculated with exposure measurements.



Figure B.7: An array of OSLs taped to the cesium source window 11.2 cm from the source.

## B.1 OSL Calibration measurements

The OSL nanoDots were calibrated using the J.L Shepherd cesium-137 source. A Geant4 simulation of the cesium source was created and used (the value of the activity from above was simulated). The simulation gave a calculated value of 215.126 rads/hr, which would give the exposure to dose in the carbon doped Aluminum oxide conversion factor as  $\approx 0.85$ , which is in agreement with the exposure to dose in an aluminum conversion factor of 0.85<sup>[37]</sup>.<sup>1</sup>

Separate arrays of OSLs were irradiated to specific doses as listed in table B.1. There was a total of four calibrations done on OSLs from three different batches received from the manufacturer.

These OSLs are then measured in a microStar reader to obtain scaled PMT counts (according to their sensitivity value, which is a calibration value set at the factory). These PMT counts are then used to make a fit of Dose vs PMT counts. As seen in Figure 4.13. This fit function can then be used to fit all dose measurements. So we have 5.7 % error from the dose estimate on the cesium source, and an averaged 5 % error from the repeatability

<sup>1</sup>Using equation 4.4 from the ICRU report and NIST values for  $\frac{\mu_{en}}{\rho}$  for air and Aluminum

Time Irradiated [hr]	Dose [Gy]	Avg. PMT Count	$\sigma_{pmt}$
0.45	0.97	61266	3538
1.35	2.91	200144	13186
2.26	4.85	351029	12522
2.71	5.83	444759	30524
3.61	7.77	600864	24940
4.52	9.71	786293	29938
5.87	12.63	1052297	45267

Table B.1: Time irradiated, doses achieved, scaled PMT counts from microStar reader, and the uncertainty in the PMT counts

measurements of the OSL PMT counts, this is similar to the error found in<sup>[36]</sup>. This Yields a 7.6% error on dose estimations using these nanodot dosimeters.

# Appendix C

## Beam Characterization

We quantified the electron beam's radial and angular distribution, which is then used in the G4 simulation. To quantify these distributions, an  $8 \times 8$  in<sup>2</sup> glass slide or a piece of gafchromic film is irradiated 25, 50, and 75 cm away from the beam pipe window. A set number of beam pulses is shot at the material, a photocopier scans the material, and the image is analyzed using ROOT to obtain a distribution.

We analyze the scanned images of the beam distribution by converting the RGB values of the image to grey scale values. 2D projections are made, normalized, and fit with a Gaussian function. Figure C.2 shows these projections and the fits of each image.

Simulations of glass slides at the same distances are irradiated, and the histograms are compared to the real-world histograms in a residual minimization study. This study scans a large phase space of the simulated radial and angular sigma beam parameters. A residual (FOM) is found between the simulated and real histograms. Minimizing this number gives us the best combinations of settings to use in the G4. Figures C.3 and C.4 give the results. From these plots, the minimum value is 0.2 for the radial sigma and 0.8 for the angular sigma.

After the beam parameter optimization, all that's left is to simulate the HPFS. A plot of the dose on a  $5 \times 5 \times 1$  cm<sup>3</sup> HPFS sample is shown below in Figure C.6 with the deposition

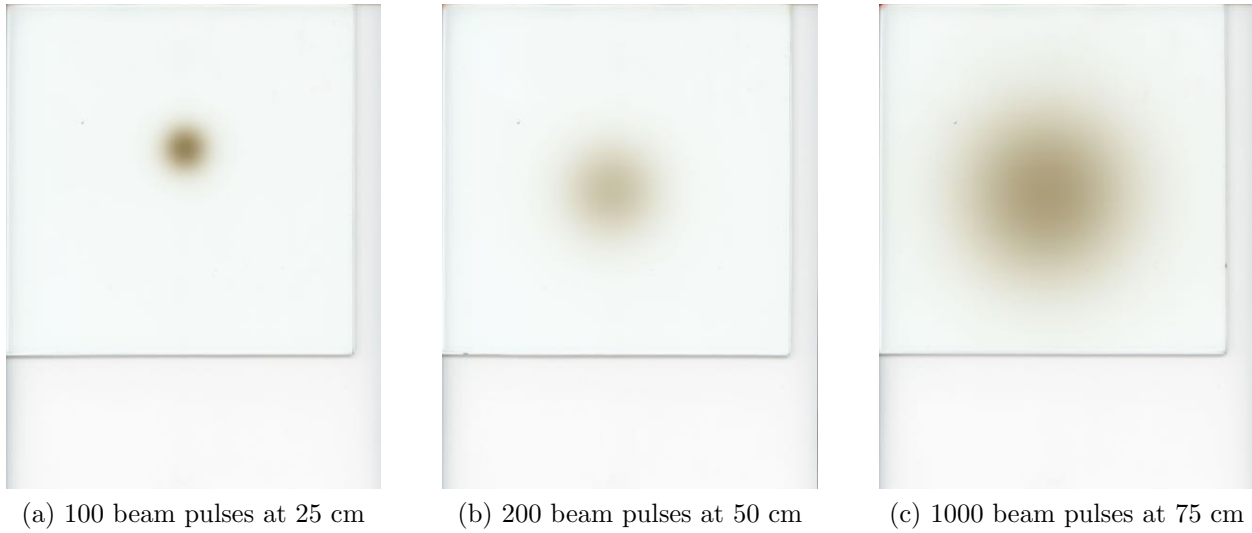


Figure C.1: Scans of the irradiated glass slides at different distances

along the z-axis in Figure C.6b. These Figures show the output of the G4 simulation broken into  $5 \times 5 \text{ mm}^2$  squares; the square of interest is the center where the dose is the highest. This area is where we measure through with light transmission measurements. These results are shown in dose per nC.

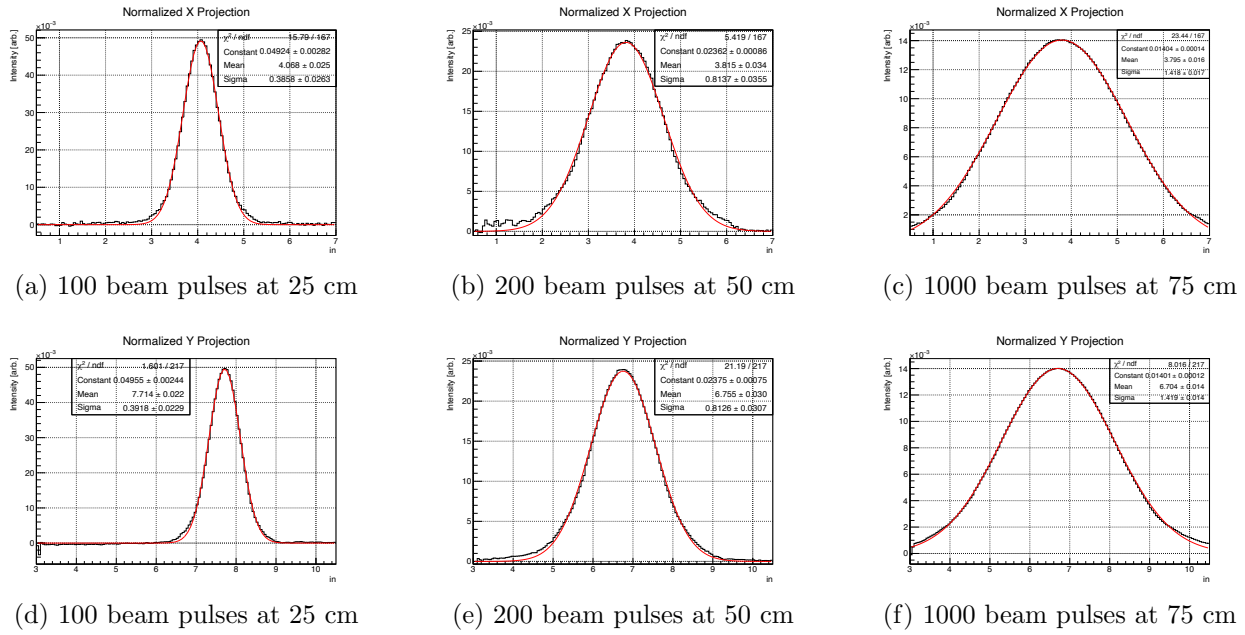


Figure C.2: X and Y projections of the glass slide distributions

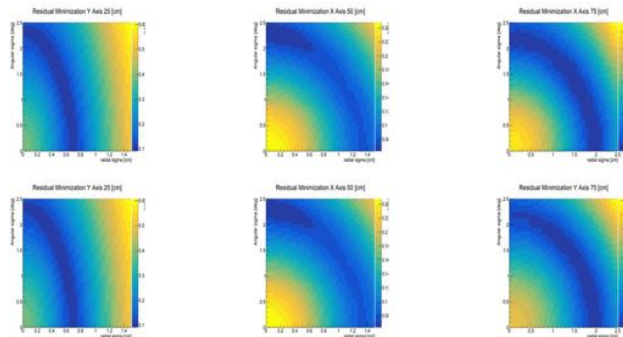


Figure C.3: The Figure of merit comparing the real world histogram to the simulation histogram for every distance for each axis projection. The optimal values are on the blue end of the spectrum.

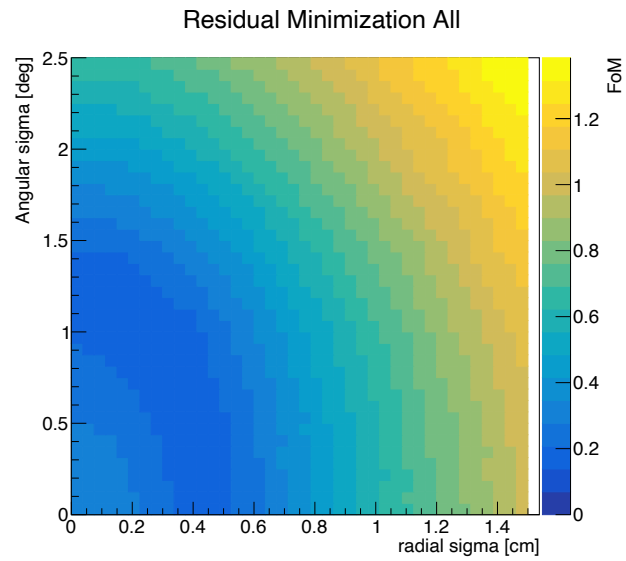


Figure C.4: Every FOM combined into one graph. The optimal values are on the blue end of the spectrum.

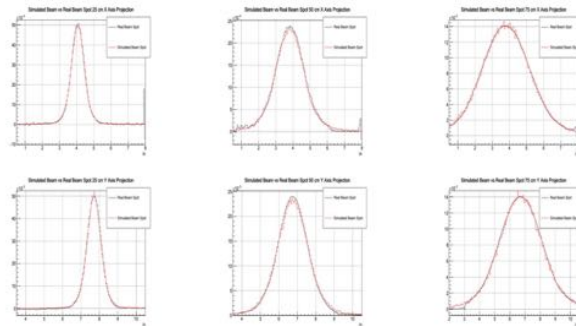
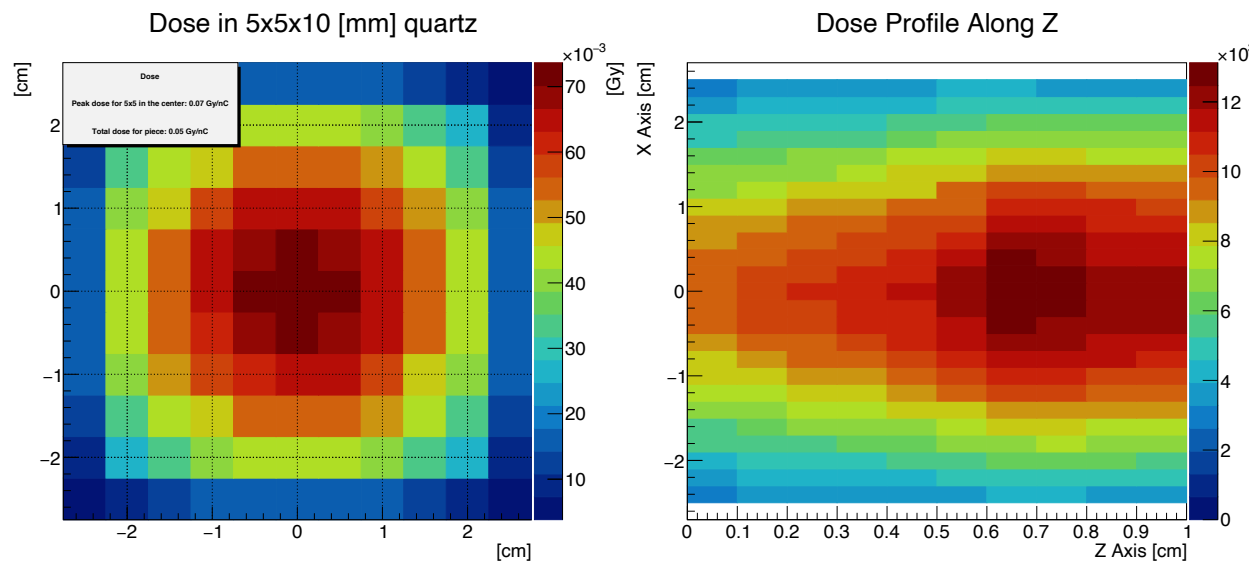


Figure C.5: Graphs of the distributions of the glass slides in the real world and the optimised simulated distributions.



(a) Dose profile projection across the face of the quartz (b) Dose profile projection along the width of the quartz

Figure C.6: These are an example of the dose profile in